國 立 交 通 大 學

電機工程學系

博士論文

腦神經訊號感測元件開發與系統整合應用

Development of Neural Recording Sensors and Electronics for Microsystem Integration

研 究 生：張志瑋

指導教授：邱俊誠 教授

中華民國 一百年 四月

腦神經訊號感測元件開發與系統整合應用

研究生：張志瑋　　　　　　　　　　　　指導教授：邱俊誠 博士

國立交通大學電控工程研究所博士班

摘要

此論文討論各式腦神經電訊號感測器與生醫電子電路系統設計相關研究，以應用於神經醫療微系統整合為最終目的。研究內容包括(一) 微機電針狀乾式電極，使用於腦電波紀錄，擁有優秀的感測介面阻抗表現；具有自我穩定機制與可應用於光動力療法之微探針陣列亦在本論文中逐一探討。(二) 可撓性大腦皮層感測電極陣列，利用高分子聚合物製造，可應用於腦部表面電位量測，此成果已在聲音刺激大鼠腦部聽覺神經反應紀錄中獲得驗證。(三) 三維神經探針感測陣列，以觀察與紀錄神經訊號在三維神經組織空間中的傳遞以及訊號源的分析為目的，其相關製程與封裝技術可用於與後級晶片整合。(四)無線傳能系統，包括了電感耦合線圈以及低壓降整流器製作，可用於無電池之微系統應用。(五)多通道類比前端放大器的設計與製作，其具有低功耗低雜訊的特色，並結合微控器與藍芽傳輸介面設計，做為各式神經訊號感測之醫療輔具應用系統之初步實現。上述諸類感測器涵蓋了各式腦神經電訊號範圍，而電源與感測電路設計亦為生醫微系統不可或缺的重要角色，搭配其他電子元件即可成為應用於生醫感測之整合式微系統。

Development of Neural Recording Sensors and Electronics

for Microsystem Integration

Student：Chih-Wei Chang   Advisor：Dr. Jin-Chern Chiou

Institute of Electrical and Control Engineering
National Chiao-Tung University

Abstract

In this dissertation, versatile neural sensors and electronics are developed for biomedical microsystems integration. Presented devices include (1) MEMS surface mounted dry electrode (MDE), which provides superior low interface impedance performance. Alternative diamond-shaped MDE and transparent MDE for self-stability enhancement and PDT applications are also reported. (2) Flexible gird electrode array using parylene-C as structure is fabricated for ECoG recording with *in-vivo* auditory response recording in rat. (3) Stacked three dimensional (3D) microprobe array developed for implantable neural recording provides simple process, solid structure with possibility for system integration, design flexibility and volume usage efficiency. The neural signal data acquired by the 3D array achieves the recording and mapping of the neural signal network and interconnections among the target brain structure, which allows further studies for event-related observation. (4) Wireless RF-powering electronics, which is designed for implantable biomedical microsystem applications. Miniaturized spiral coils as a wireless power module and low-dropout linear regulator circuit convert RF signal into DC voltage for batteryless applications. (5) 16-channel analog front end neural amplifier is introduced for biopotential conditioning, which offers technical merits of reduced supply voltage, sufficient low power per channel and reasonable low noise performance, yet offers integration with micro controller unit and Bluetooth modules for conceptual biomedical microsystem representation. Proposed sensors and electronics provide versatile neural recording and key component realization in microsystem design, as well as achieving the development of biomedical prosthesis applications by integrating with commercial modules.

誌謝

感謝指導老師 邱俊誠教授在求學路上的諄諄教誨，師恩浩蕩，永銘於心。感謝口試委員吳重雨教授、羅錦興教授、歐陽盟教授、梁勝富教授與段正仁博士的指導與建議，讓此論文更加完備。此外，感謝辛裕隆醫師、陳右穎教授、黃建峻博士與張嘉麟博士在研究上的協助與勉勵。

感謝實驗室朝夕相處互相砥礪的夥伴，陳志良、洪振鈞、謝禮忠、侯冠州、蔡尚瑋、林君穎、林岳正、黃煜傑、周俊仲、鄒慶華、何檀均、王詠鋒、洪聖昕、陳彥璋、楊可筠以及詹巧雯，小弟感銘五內。

感謝女友婉筠的支持與陪伴，是促使我不斷前進的動力。

最後謹以此論文獻給我的父母，以及弟妹，沒有你們，就沒有今天的我。

江雨霏霏江草齊，六朝如夢鳥空啼。

無情最是臺城柳，依舊煙籠十里堤。

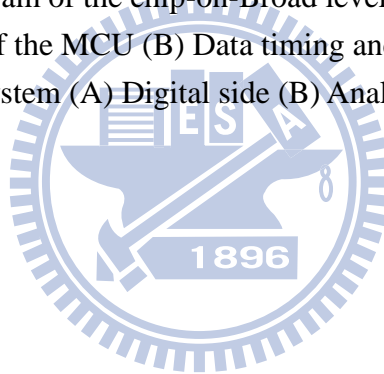<div align="right">

張志瑋

2011 年五月 新竹

</div>

Content

List of Figures

List of Tables

Chapter 1

Introduction

1.1 Biopotential Signals in Brain

Many organs in the human body, such as the heart, brain, muscles, and eyes, manifest their function through electric activity. The heart, for example, produces a signal called the electrocardiogram (ECG). The brain produces a signal called an electroencephalogram or EEG. The contraction and relaxation activity of muscles produces an electromyogram (EMG). Eye movement results in a signal called an electrooculogram (EOG), and the retina within the eyes produces the electroretinogram (ERG). Measurements of these and other electric signals from the body can provide vital clues as to normal or pathological functions of the organs. For example, abnormal heart beats or arrhythmias can be readily diagnosed from an ECG. Neurologists interpret EEG signals to identify epileptic seizure events. EMG signals can be helpful in assessing muscle function as well as neuromuscular disorders. EOG signals are used in the diagnosis of disorders of eye movement and balance disorders [1]. Examples of human biopotential waveforms are shown in Fig. 1.1 [1].

The origins of these biopotentials can be traced to the electric activity at the cellular level [2]. The electric potential across a cell membrane is the result of different ionic concentrations that exist inside and outside the cell. The electrochemical concentration gradient across a semi-permeable membrane results in the Nernst potential. The cell membrane separates high concentrations of potassium ion and low concentrations of sodium ions (along with other ions such as calcium in less significant proportions) inside a cell and just the opposite outside a cell. This difference in ionic concentration across the cell membrane produces the resting potential [3]. Some of the cells in the body are excitable and produce what is called an action potential, which results from a rapid flux of ions across the cell membrane in response to an electric stimulation or transient change in the electric gradient of the cell [4]. The electric excitation of cells generates currents in the surrounding volume conductor manifesting itself as potentials in the body.

Fig. 1.2 illustrates the biopotentials in brain [5]. Different signals are acquired depend on the recording methodology and location. The neural spikes, which are known as nerve impulses or action potentials, are produced by single unit firings. The temporal sequence of action potentials emitted by a neuron is called its spike train. The neural spikes are recorded
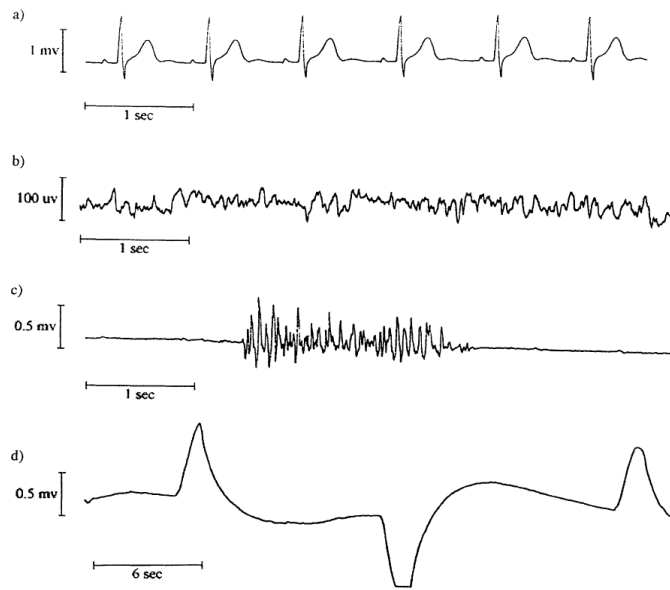
Fig. 1.1 Waveforms of the biopotentials: (a) ECG (b) EEG (c) EMG (d) EOG [1]

via microelectrodes or probes placed close to the neuron cell body. Local field potential (LFP), or near-field potential, is a particular class of electrophysiological signals, which is dominated by the electrical current flowing from all nearby synaptic activity within a volume of tissue. The signal is produced by the summed synaptic current flowing across the resistance of the local extracellular space. The electrical potential or voltage is recorded with a very small electrode embedded within neuronal tissue, typically in the brain of an anesthetized animal or *in-vitro* within a slice of brain tissue maintained [6]. Briefly speaking, the LPF is the summation of pre/post-synaptic activity from a population of neurons recorded the electrode tip.

Electrocorticography (ECoG) is the electrical activity on the cortical surface resulted from volume conduction of coherent collective neural activity throughout cortex. ECoG is recorded via electrodes placed directly on the exposed surface of the brain to record electrical activity from the cerebral cortex. ECoG may be performed either in the operating room during surgery (intra-operative ECoG) or outside of surgery (extra-operative ECoG). Because a *craniotomy* (a surgical incision into the skull) is required to implant the electrode grid, ECoG is an invasive procedure [4].

EEG is the electrical activity on the scalp resulted from volume conduction of coherent collective neural activity through the brain and skull, and laterally along the scalp. The recording of EEG along the scalp can be seen as producing by the firing of neurons within the brain [7]. In clinical contexts, EEG refers to the recording of the brain's spontaneous electrical activity over a period of time, as recorded from multiple electrodes placed on the scalp. In neurology, the main diagnostic application of EEG is in the case of epilepsy, as epileptic activity can create clear abnormalities on a standard EEG study [8]. Fig. 1.3 detailed the recording electrode placements for different recording proposes.
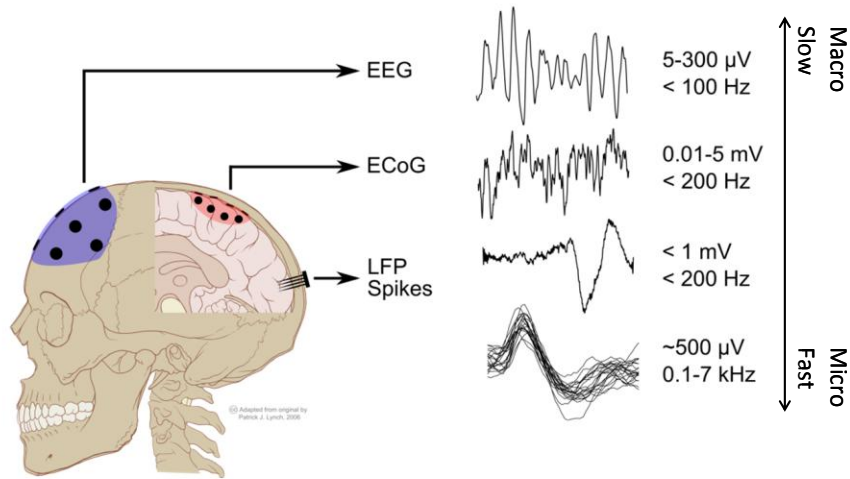
Fig. 1.2 Biopotentials in brain [5]
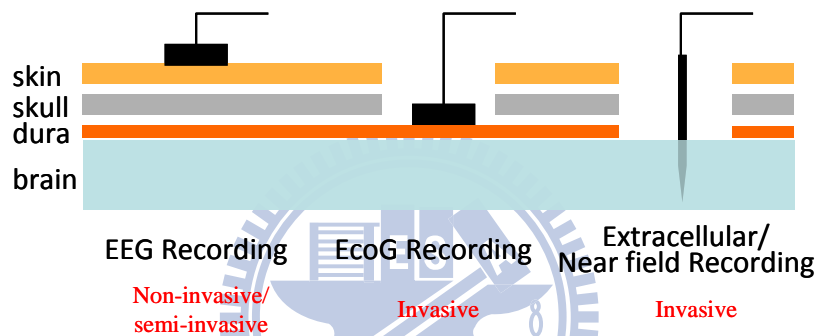
Fig. 1.3 Brain electrical activity recording

From the scale point of view, EEG provides low resolution information of the brain activity but benefits by non-invasive recording requirement with smaller magnitude and behaves in low frequency band. The Derivatives of the EEG technique includes evoked potentials (EP) and Event-related potentials (ERPs), which involves averaging EEG activity time-locked to the presentation of stimuli in cognitive psycho-physiological researches [7]. In the other hand, neural spike recordings provide detailed information in a localized area or specified neuron unit. In processing neural spike signals, spike sorting is a critical step in neuroscience research. When an electrode is inserted into the brain for neural recording, it typically detects signals from multiple different neurons. Each neuron exhibits spikes with distinct characteristics, such as amplitude and shape. Spike sorting is the process of using these characteristics to determine which neuron contributed a given spike. This critical step in the neural processing stream decodes patient's intentions for neuroprosthesis applications [9].

1.2 Preview of Neural Recording Sensors and Systems

Biomedical devices for neural recording in the central nervous system are widely viewed as

a promising path to revolutionary progress in understanding neural functions and to the realization of practical neural prostheses. Also, long-tem, real-time and stable observation on the monitoring target for treating disorders such as epilepsy, seizures as well as for rehabilitative prosthesis is required for these biomedical device designs. Such biomedical device usually includes two main parts, the sensors and the systems. The former collects the biopotentials from the target volume of tissue, while the latter provides signal conditioning, processing and transmission. Miniaturized, light-weight, wireless implantable bio-sensors and microsystems are the key solution to capture accurate biological signals from an untethered subject in his natural habitat.

Many neuroscience techniques have been reported to study the functional relationships in the brain. In addition to the brain imaging techniques such as functional magnetic resonance imaging (fMRI) and positron emission tomography (PET), electrical recording techniques play an important role in brain functionality mapping as well. For example, electrocorticography recorded with intracranial electrodes onto dura surface and local-field potentials using penetrated probes or non-penetrating grid electrodes, are clinically applied methods to record the electrical activity in the brain. Penetrated electrode probes in brain may cause the risk of damaging the brain tissue but benefits from precise signal location, while the flexible grid electrode arrays placed on the cortical surface can be used as a less invasive method in some clinical cases, e.g. in epilepsy surgery. Therefore, different sensors are chosen for the application conditions requirements.

To date, many types of sensor/microsystem manufacture technology for neural sensing are reported. Versatile microprobe arrays are fabricated by bulk silicon, polymer or assembly structure for biopotential sensory and implantable microsystems. For the silicon bulk etched arrays, one of the disadvantages is every probe in array only functions as one recording site [10]. Also when the array was integrated with active circuit boards [11], the minimal opening for implantation is relatively huge. Polymer-based sensors usually are used as planar or grid electrode arrays [12]. The flexible property of polymer makes it easier to fit the shape of the implant tissue. Some fully integrated microsystems for implantation application have been reported, such as blood pressure monitoring [13] and single unit recording [14]. However, disadvantages still exist, such as low channel account and bulky sensor array designs.

1.3 Motivation for sensor and system development.

Prior art shows demands for new fabrication technology in sensors design and integrated system for advanced neural recording, including smaller size, improved performance, convenient usage and integration probabilities. For example, standard electrodes in EEG recording are known as its disadvantage that using electrolytic gel. Also, for ECoG and extracellular measurement, new material, structure and assembly advancements are needed

for superior recording performance. Furthermore, electronics for the amplification, conditioning and transmission are required to achieve fully integrated sensing environment. Therefore, sensors fabricated by Micro Electro-Mechanical Systems (MEMS) technique are utilized in this dissertation, as well as the Integrated Circuits (ICs) design for analog biopotential processing and powering issues in the neural sensing microsystem. Such system is demanded to deal with every kind of neural signals that recording by the MEMS based sensors in brain.

In this work, versatile neural sensors associated with powering/amplification bioelectronics are presented for implantable microsystem design. Proposed system structure is shown in Fig. 1.4. MEMS dry electrode (MDE), Grid electrode array and 3D neural array are developed for EEG, ECoG, LPF and neural spike acquisition. Bioelectronics including neural amplifier and RF-DC regulator are designed for wireless powering and signal conditioning purposes. Electrode arrays sense and transfer the neural signals from the target tissue to the neural amplifier for signal conditioning and amplification. The developed components can be integrated with commercial chips for a conceptual representation toward microsystem in the thesis.
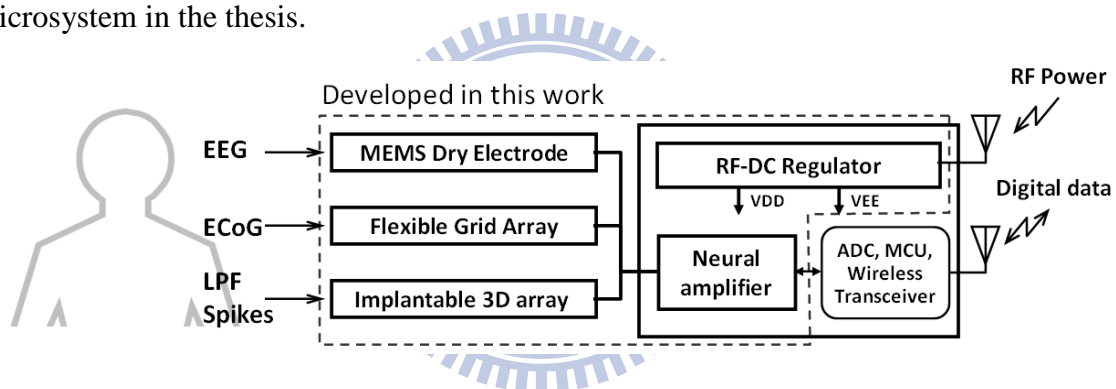
Fig. 1.4 Proposed neural sensors and microsystems in this thesis. The dotted area denotes the devices that developed in this work.

1.4 Organization of Dissertation Work

This dissertation is organized as follows. Chapter 1 provides the introductions and motivations as well as the background on this research. A microsystem structure consists of versatile neural sensors associated with powering and signal conditioning electronics for neuroprosthesis applications is described. Detailed designs and results for the sensors and electrical systems are reported in the following chapters. Chapter 2 introduces a series of surface-mounted MEMS dry electrode (MDE) development for EEG, drowsiness and photo dynamic therapy (PDT) applications. Functions including low interface impedance, self-stability and transparent light guide are detailed in this chapter. Chapter 3 presents a flexible gird electrode array made by polymer for ECoG measurements; related device fabrication and characterization are investigated in this chapter. Chapter 4 reports a new stacking method for assembling a 3D microprobe array with great structure strength,

smaller implantable opening and simple assembly steps. Proposed method also provides design flexibility and volume usage efficiency. 3D neural signal propagation observation for human cerebral cortex layers is achieved by practical implantation in excised brain tissue after resection surgery in this study, which achieves the mapping and observation of the neural signal network among the target brain structure. Chapter 5 illustrates the integrated electronics toward microsystem. Miniaturized spiral coils as a wireless power module with low-dropout regulator circuit is developed to convert RF signal into DC voltage for batteryless implantation. 16-channel analog-front-end neural amplifier is also introduced, offering technical merits of sufficient low power and reasonable low noise performance. An integrated microsystem using the fabricated neural amplifier associated with commercial micro control unit and wireless transceiver module are described as well. Chapter 6 draws the conclusions in this work and provides possible future directions for further research.
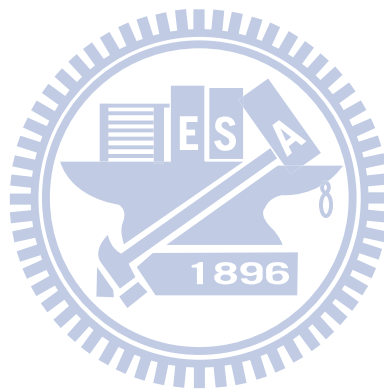
Chapter 2

Skin Surface-Mounted MEMS Dry Electrode

2.1 Biopotential Electrode for Electroencephalography Recording

EEG signals consist of the differences in electrical potentials caused by summed postsynaptic graded potentials from pyramidal cells that create electrical dipoles between the soma (body of neuron) and apical dendrites (neural branches) [15]. The EEG is typically described in terms of rhythmic activity, which is divided into bands by frequency. For example, these frequency bands are a matter of nomenclature i.e. rhythmic activity between 8–12 Hz is described as *alpha wave*. Also, rhythmic activity within a certain frequency range was noted to have a certain distribution over the scalp or a certain biological significance [15]. Frequency bands are usually extracted using spectral methods as implemented by EEG software. Biopotential electrodes for EEG recording transfer signals from skin tissue to the amplifier circuit. When the electrodes placed onto the skin, say surface-mounted electrode, actually act as a voltage divider with the amplifier input resistance for signal transportation. Therefore, the most important characteristic of a biopotential electrode is low electrode-skin interface impedance so that signals can be propagated without attenuation or production of noise [16].

In this chapter, various types of MEMS-based dry electrodes (MDE) are presented for different purpose. Silicon-based MDE fabricated via micromachining technology is proposed for high-fidelity EEG sensor with low electrode-skin interface impedance. Diamond-shaped MDE (DS-MDE) provides extra self-stability onto skin during measurement. Finally, a transparent MDE fabricated by advanced hot-embossing process is illustrated for photodynamic therapy application in this chapter as well.

2.2 MEMS Dry Electrode

When electrodes are placed on the skin of the forehead, an electrode-skin interface is constructed. The anatomy of the skin consists of three different layers: the *epidermis*, the *dermis*, and the subcutaneous layer. The *epidermis* contains two further layers: the *stratum corneum* (SC) and the *stratum germinativum* (SG). The SC consists of dead cells and thus has electrical isolation characteristics. The SG is composed of living cells and is therefore

electrically conductive. Blood vessels and nerves are located in the dermis [17].

To overcome the electrical isolation properties of the SC, standard wet electrodes always require that the skin is prepared (abrasion of the SC) and an electrolytic gel is used. Improper skin preparation may cause skin irritation, pain, or even infection. Using electrolytic gel is uncomfortable and inconvenient; it can cause an itchy feeling, and sometimes makes skin red and swollen when EEG measurements are made over a long period of time. Furthermore, the conductivity of gel gradually decreases because it hardens, resulting in degradation in the quality of data acquisition.

In this work, presented MEMS dry electrode (MDE) is designed to penetrate the SC layer into the electrically conductive SG layer but stop before the *dermis* layer to avoid pain or bleeding. Fig. 2.1 shows the basic idea and the difference between MDE, DS-MDE, transparent MDE and standard wet electrode. Since the dry electrode is expected to circumvent the high impedance characteristics of the SC, skin preparation and electrolytic gel application are thus not required. The thickness of the *epidermis* varies in different types of skin, but almost in the range from 0.05 mm (eyelids) to 1.5 mm (palms and soles). The *dermis* also varies in thickness depending on the location of the skin. It is 0.3 mm on the eyelids and 3.0 mm on the back [18]. The most important layer for EEG measurement, SC, is thinnest skin layer, being less than 20 um. Therefore, as long as the length of the microprobes on dry electrode are longer than the thickness of the SC, then, low electrode-skin-interface impedance can be achieved by the spiked tip of microprobe reaching the SG layer.
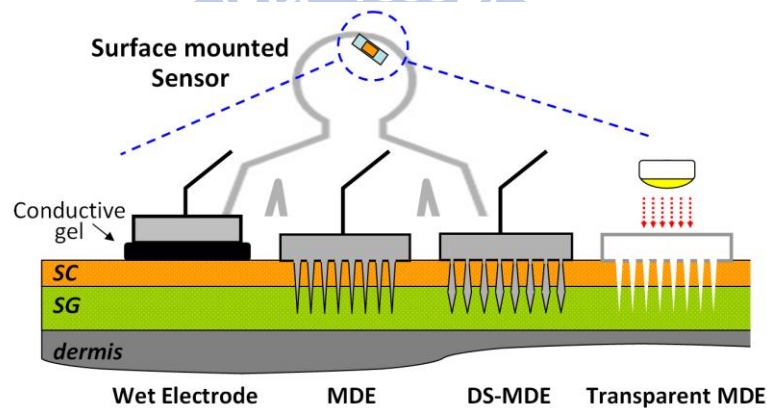
Fig. 2.1 Implementation diagram of applying standard wet electrode, MDE and DS-MDE onto skin surface

The relating electrode-skin interface cross section sketch and the related electrode-skin-interface equivalent circuit are illustrated in Fig. 2.2. The model for the standard electrode includes a capacitance C_d and a resistor R_d at the electrochemical electrode–electrolyte interface of the standard electrode and the electrolytic gel. The resistor R_S reflects the electrical resistivity of the electrolytic gel. The SC can be considered to be a semi-permeable membrane. If there is a difference in ionic concentration across this

membrane (e.g., the ion concentration of the electrolytic gel and the ion concentration of the SG do not match perfectly), there is a potential difference E_{se}. Furthermore, the electrolytic gel soaked SC shows distinctive resistive and capacitive behavior, represented by C_e and R_e. Finally, R_u is the resistivity of the SG and underlying tissue. The model of the dry spiked electrode is less complex. The conductive metal coating of the spikes is in direct contact with the SG, hence, an electrode–electrolyte interface, C_d and R_d, is created. R_m is the resistivity of the SG and underlying tissue [19].
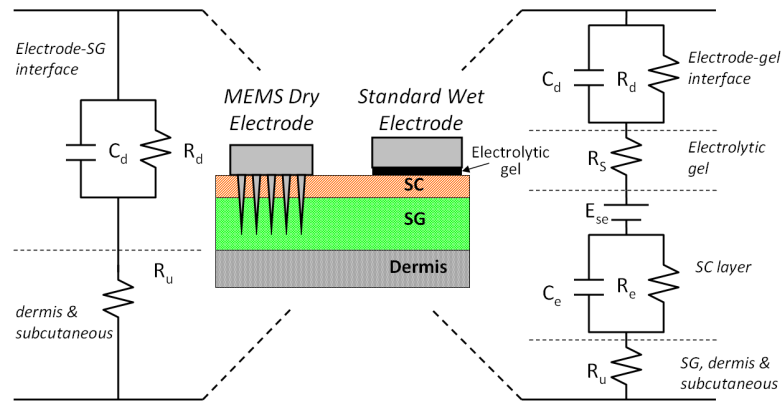
Fig. 2.2 Electrode-skin interface comparison between spiked dry and electrode standard wet electrode.

2.3 Diamond-Shaped MDE

The MDE designs [20] use electrically conductive microprobe to penetrate the high electrically resistive outer skin layer to obtain better electrical conductivity than wet electrodes. However, the conical shape microprobe array lacks the position stabilization capability. This limitation is due to the force created by the compressed skin tissue that continually counteracts the conical shape microprobes into outward direction and degrades the bio-signal recording quality directly. To overcome this drawback, a self-stabilized, DS-MDE is developed. The proposed diamond-like design has a wider neck and a narrower bottom than previous conical shape dry electrodes. This configuration provides an external force to stabilize the probe that can remain in the skin when the tissue counteracts the probe continually. In contrast with a related work [21] which also demonstrates the mechanical attachment capability of a body surface electrode, the proposed DS-MDE without sharp barded edges does not damage the skin tissue after removing the electrodes from skin. The DS-MDE can thus provide satisfying self-stability capability and superior electric conductivity when attached onto skin without additional tissue injury.

Fig. 2.3 (A) illustrates the forces applied on the probe after the DS-MDE was placed onto skin tissue. F_b and F_p, caused by the compressed tissue, are the normal force applied on the face of tip and the face of shaft. Fr is the resultant force of $|F_b + F_p|$ with direction towards the skin. F_c and F_v denote the frictional force and viscous force, respectively. F_s is the

minimal force that required for dragging out the probe from skin tissue. Clearly, the minimal F_s for dragging out the probe is

$$F_s \geq F_r + \left(F_c + F_v \right) \qquad (2\text{-}1)$$

Since that F_c and F_v are small, difficult to estimate and always help the probe to stay in the tissue when the probes are dragging out of the tissue, they are ignored in the simulation. To quantitatively determine the improved self-stability of the presented DS-MDE comparing with MDE, stability factor (SF) is simply defined as the F_r, the resultant force of $|F_b + F_p|$. It is clear that if F_r can provide an inward force into the tissue, the stability of the probe can be improved.

The force F_b and F_p are positively proportional to the compressed tissue volume, which can be calculated from the dimension of probe (a, b, c and d) illustrated in the force diagram. Thus, the resultant force F_r is calculated from the angle relationship in the force diagram. For the general MDE, its vertical shaft wall (a = b) and conical tip result in a F_r with outward direction from the tissue which can not help the probe stay in the skin. Comparing with the MDE, DS-MDE with an invert-triangle shaft wall makes the resultant of F_b with the direction towards into the tissue, which helps the probe stay in the skin.

The calculated result indicates that the narrower the bottom width a, the higher stability can be achieved. Simulation result is shown in Fig. 2.3 (B).Note that with tip length and neck diameter are 50μm, SF reaches the maximum value if the bottom diameter is less than 30μm and shaft length is longer than 150μm. As a result, a stable probe configuration with 250μm probe length has been designed to reach the SG layer.
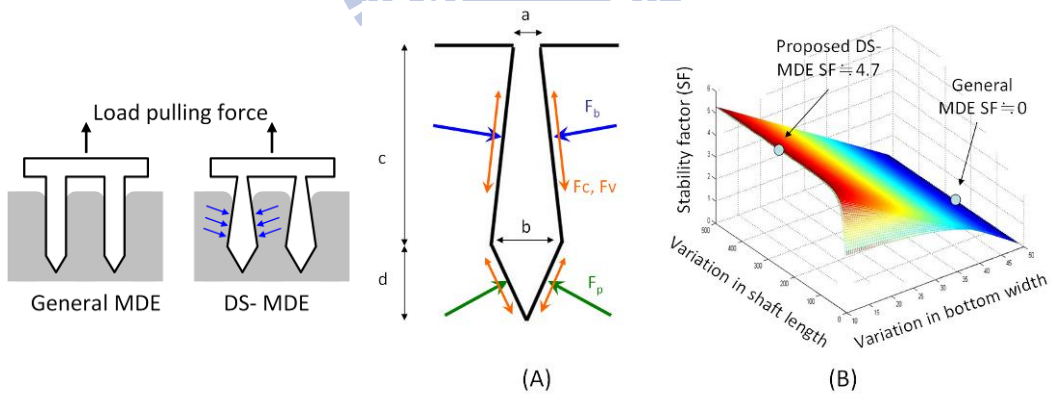
Fig. 2.3 Stability modeling

2.3 Fabrication and Characterization

The fabrication process of MDE and DS-MDE is illustrated as Fig. 2.4. The microfabrication process consisting of ion-etching with inductive coupled plasma (RIE-ICP) etching process and sputtering metallization technology was developed. In this process, a 6μm thick photoresist film was patterned as circular hard-mask for the isotropic etching process to produce the probe tip. Next, we proceeded with the anisotropic etching process to

form the probe shaft with high aspect ratio. According to the etching parameter control, different style of shafts including cylindrically shaped and inverted-triangle shaped are fabricated for MDE and DS-MDE, respectively. Then, the hard mask at the probe tip was released by sulfuric acid wet-etching. Finally, the probes were subsequently coated with titanium and platinum using sputtering technique to achieve electrical conductivity and bio-compatibility.
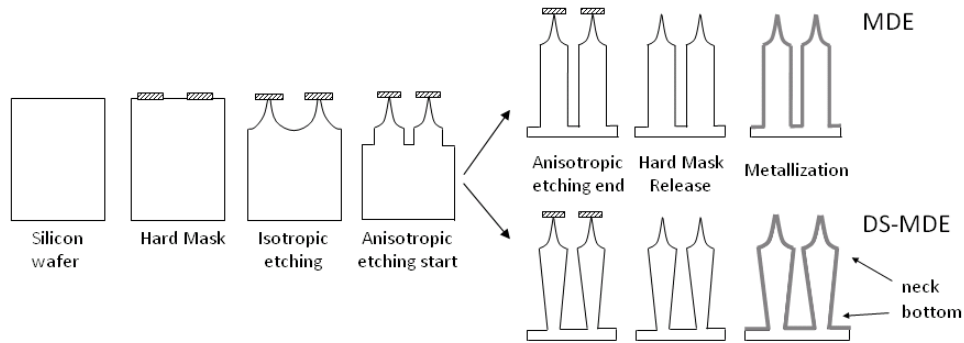
Fig. 2.4 Fabrication process flow

Fig. 2.5 shows the microphotograph of the fabricated results: (a) microprobe array of MDE, (b) tip of the microprobe, (c) inverted-triangle shaped microprobe array of DS-MDE, (d) close view of the DS-MDE. The fabricated MDE and DS-MDE are 20×20 array in 4×4 cm2 with 250μm in probe height. The MDE is 30μm probe width, while the DS-MDE is 50μm and 17μm in neck and bottom width, respectively. Notably, the peak of the probes on the DS-MDE are not perfectly sharp (< 10 μm) but tiny enough to penetrate the outer skin layer.
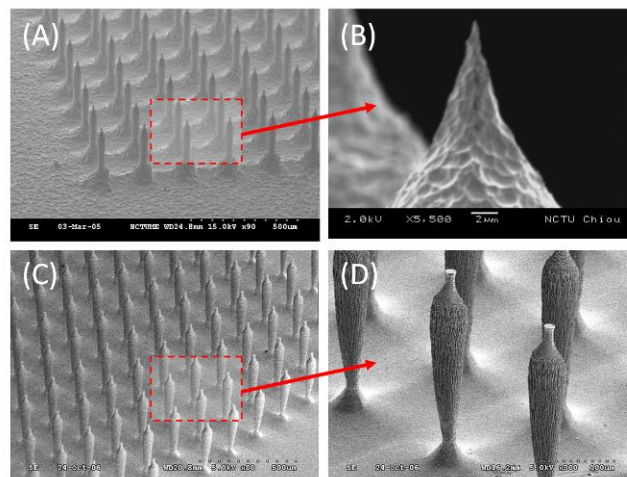
Fig. 2.5 Fabrication results

To characterize the electrode-skin interface impedance effect, two electrodes were lined up on the forehead with a distance of 4 cm apart to perform an electrode-skin-electrode interface (ESEI) experiments. The ESEI acts as two electrode-skin interface in series. Therefore, lower ESEI performance implies lower electrode-skin impedance. A circuit [19]

was used to determine the ESEI impedance and reduce the risk of harming the test person during biopotential recordings [22]. A total of 19 tests were performed, involving 5 subjects to evaluate the performance of different types of electrode. According to Fig. 2.6, in the interest frequency range for EEG (0.5~100 Hz), MDE shows much smaller impedance performance then standard wet electrodes under condition without skin preparation (use of gel, abrasion of the SC). Experiment results demonstrate that the impedance of presented MDE was superior to that of the wet electrodes.
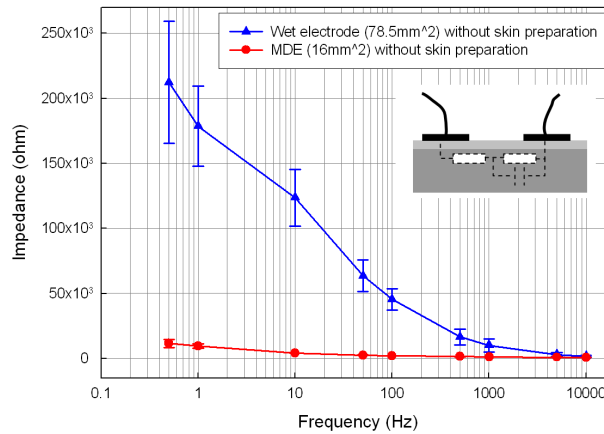
Fig. 2.6 Electrode-skin interface impedance characterization

A recording example of the MDE and standard wet electrode is shown in Fig. 2.7. The recorded EEG signal (α rhythm, 8-12Hz, seen in normal relaxed adults) with the peak-to-peak magnitude of approximate 0.5V and 0.95V for MDE and wet electrode. Note that both wet electrode and MDE are placed at the neighboring location with identical amplifier circuit. The relationship of electrode/skin interface impedance and the signal intensity proved the advantage of the MDE design.
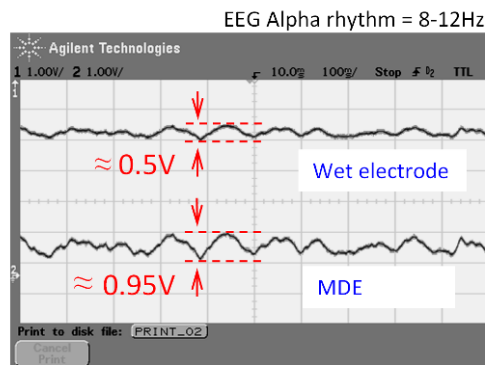
Fig. 2.7 Recording example of alpha rhythm by MDE and standard wet electrode

To compare the EEG signals acquired by MDE and standard wet electrodes, five MDE/wet electrode pairs are placed at the frontal of head. The MDE/wet electrode pair 1 and 5 is placed at Fp1 and Fp2 according to the international 10-20 electrode placement system [1].

Three more electrode pairs are also evenly placed between pair 1 and 5 labeled as MDE/wet electrode pair 2, 3, and 4, respectively. The distance between MDE and wet electrode in the MDE/wet electrode pair is about 1 cm. We used the average EEG signals at A1 and A2 as the reference. EEG signals at MDE and wet electrodes were then simultaneously recorded by the Scan NuAmps Express system (Compumedics Ltd., VIC, Australia). Before data acquisition, the contact impedance between each dry and wet electrode was calibrated to be less than 5 kΩ. The EEG data were recorded with a 16-bit quantization level at a sampling rate of 500 Hz and then re-sampled down to 250 Hz to simplify data processing. Each amplifier circuit channel had a differential-input instrumentation amplifier as the first amplifier stage, followed by a 0.5–100 Hz band pass filter and a 60 Hz notch filter.

We recruited three volunteers to take part in the experiment. In each experiment, the EEG signals were simultaneously recorded for 1000 seconds from the two pairs of disposable dry and wet electrodes, including eyes-open and eyes-closed conditions as shown in Fig. 2.8 (A). Using the comparison method [23], a segment of a time-series recording comparing the signals obtained for Subject 1 from the pair of disposable dry and wet electrodes respectively at Fp1 is shown in Fig. 2.8 (B). Also included on the plot is the Pearson correlation over 0.25-s segments. Although only a single 5-s segment is shown, the recording quality was consistent for all subjects without obvious changes in signal quality or noise levels. In Fig. 2.8 (C), statistics showed that the average Pearson correlation of all subjects was over 90%, and in 91% of the recording data it was higher than 92%. Very significant correlations, in excess of 90%, are evident throughout the record.
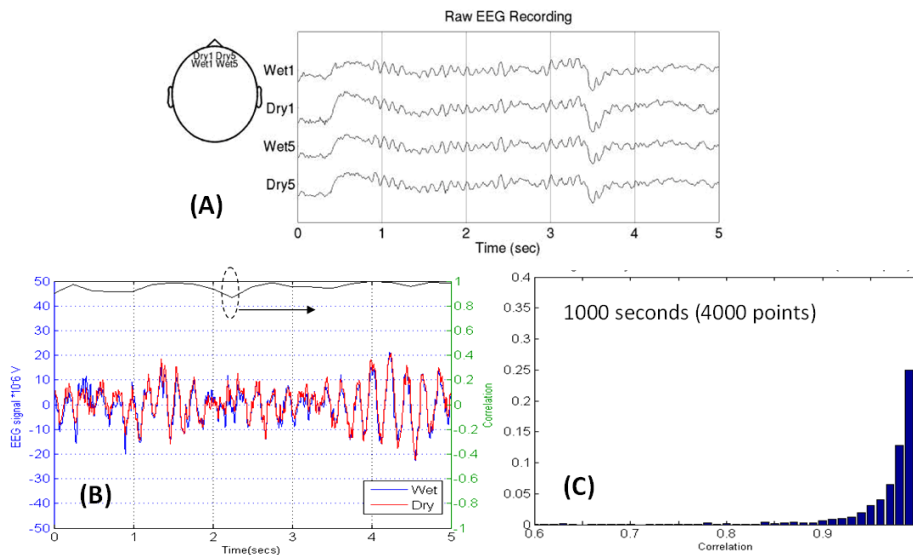
Fig. 2.8 (A) Simultaneously EEG recording from MDE and wet electrode (B) 5-s segment comparison of EEG signals. Upper line shows the Pearson correlation data calculated using 0.25-s segments. (C) Statistics analysis of the average correlation for all subjects.

The self-stabilized capability of the DS-MDE was tested by a micro force testing system

(MTS Corp., USA). MDE and DS-MDE with same area (4x4 mm^2), each consists of 20x20 micro probe array, are gluing to a PMMA holder for the pulling force test. A pig skin fixed on another PMMA plate was used for the test tissue. The DS-MDE was pressed into the pig skin tissue under testing by the holder beam of the force testing system. The force with which the DS-MDE was pressed into the tissue was not measured. After ensuring the micro probes penetrated the test tissue, the micro force testing system started to pull off the DS-MDE. During testing, the applied force and displacement were recorded. Fig. 2.9 shows the testing results. The average required pulling force for the general MDE and DS-MDE were 1.705N and 3.160N, respectively. Notably, both MDE and DS-MDE had the same chip area, number of probes and probe length.

In contrast with prior art, proposed DS-MDE without sharp barded edges does not damage the tissue after removing from skin. The DS-MDE can thus provide satisfying self-stability capability and superior electric conductivity without additional tissue injury.
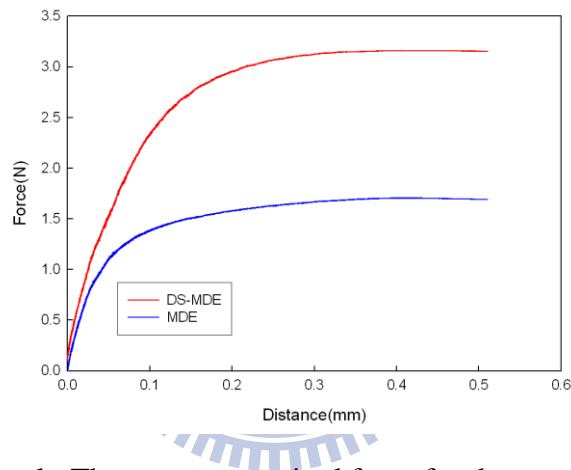
Fig. 2.9 Pulling test result. The average required force for the general MDE and DS-MDE were 1.705N and 3.160N, respectively.

2.4 Drowsiness Monitoring with MDE

In order to demonstrate the potential applications of the MDE sensors during long and routine recording in operational environments, the drowsiness monitoring was investigated according to the EEG signals recorded by proposed MDE placed at Fp1 and Fp2 in an attention-demanding driving experiment. Preventing accidents caused by drowsiness is greatly desirable but requires techniques of continuously monitoring drivers' drowsiness levels and delivering effective feedback to avoid dangerous situations at the wheel [24]. An EEG-based drowsiness estimation system that continuously estimates drivers' drowsiness levels in a virtual-reality (VR) based driving simulator is used here [25]. The VR based highway-driving environment provides the study of drivers' cognitive change during a long-term driving. Also, a lane-keeping driving error experiment is defined as the drowsiness level used to verify the estimated drowsiness level produced by the EEG power

14

spectrum analysis. The power spectrum level of theta wave and alpha wave defined the drowsiness index as shown in Fig. 2.10. During the period of increasing drowsiness but when subjects are still responding, delta and theta power increased, whereas alpha decreased [26]. Therefore, the drowsiness monitoring by MDE can be achieved by combining the EEG spectrum analysis and VR based driving error.
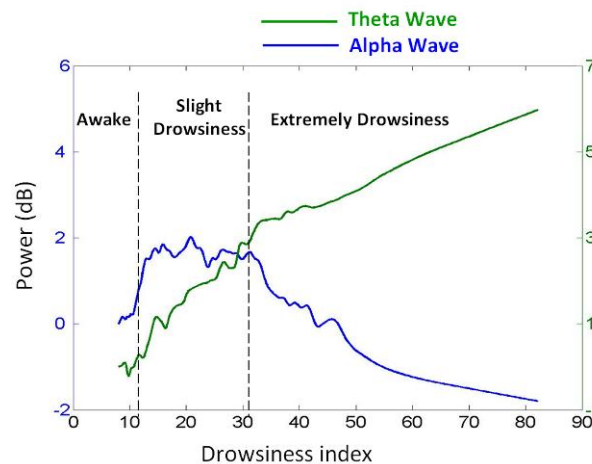
Fig. 2.10 Drowsiness level detection by EEG power spectrum observation

The EEG signals recorded by five MDE sensors are fed into an EEG-based drowsiness estimation system to indirectly estimate the driving drowsiness levels. The recorded driving performance time series were smoothed using a causal 90-s square moving-averaged filter [27] advancing at 2-s steps to eliminate variance at cycle lengths shorter than 1–2 min, since the fluctuations in drowsiness levels had a cycle length over 4 min [28]. The EEG data recorded by five MDE are first preprocessed using a simple low-pass filter with a cut-off frequency of 50 Hz to remove the line noise and other high-frequency noise. After moving-average power spectral analysis, we obtained EEG log power spectrum in time-series from the EEG sensors, with a frequency range from 1 to 40 Hz [29]. Then, Karhunen-Loeve Principal Component Analysis (PCA) is applied to the resultant EEG log spectrum to extract the directions of the largest variance for each session. Projections (PCA components) of the EEG log spectral data on the subspace formed by the eigenvectors corresponding to the largest 50 eigenvalues are used as inputs to a multiple linear regression model [30] to estimate the time course of driving errors for each subject. Each model is trained only using the features extracted from the training session and tested on a separate testing session.

Fig. 2.11 shows the performance comparison of drowsiness estimation either using MDE sensors or standard wet electrodes. As illustrated in the figure, the blue line and red line represent the driving errors acquired by VR system and estimated by EEG, respectively. Fig. 2.11(A) shows the estimated driving error correlation of Subject 1 in Session 2 by using EEG recorded from the wet electrodes, where the estimators are trained from Session 1. Conversely, Fig. 2.11 (B) shows the estimated driving error of Subject 1 using EEG data

from wet electrodes, where Session 2 acts as training dataset and Session acts as testing session. Also, Fig. 2.11 (C) and (D) show the estimated and actual errors made by Subject 2. Similarly, Fig. 2.11 (E), (F), (G) and (H) display the estimated driving error correlation made by MDE sensors with varied training session and testing session.
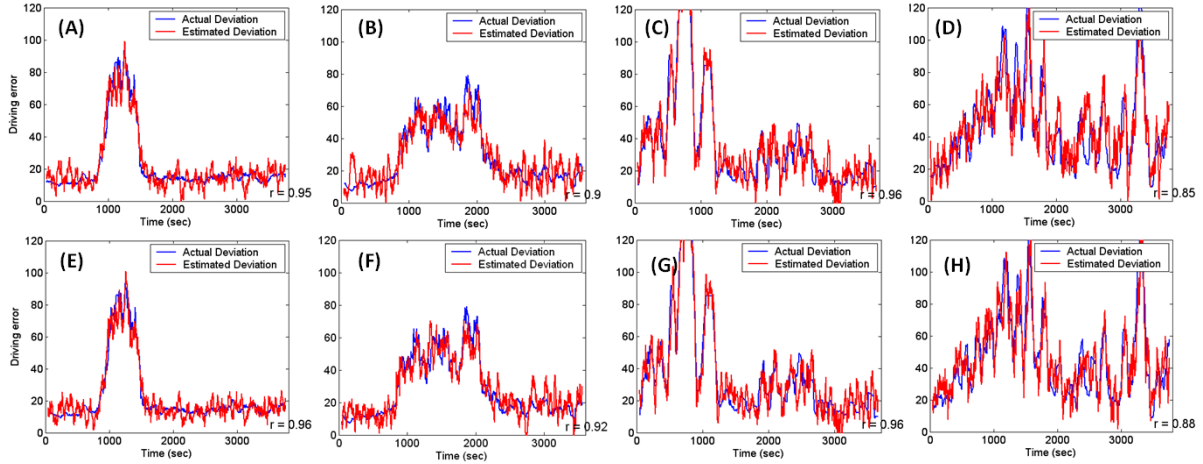
Fig. 2.11 EEG estimated (red line) and actual VR driving error (blue). (A)-(D): Estimated by standard wet electrodes (E)-(H) Estimated by MDE sensors

Table 1 shows the comparison of the correlation coefficients between the actual and estimated driving error time series using MDE and wet electrodes. As shown in Fig. 2.11 and Table 1, the estimated driving errors result using only Fp1 and Fp2 consistent with previous report s that using whole-head 32-channel EEG [31] and show its capability for driving tasks examination. The results demonstrate the feasibility of estimating subject drowsiness levels in an accurate manner based on EEG signals collected from the frontal hairless sites. Furthermore, the estimation accuracy based on the EEG collected by MDE is comparable to that based on the signals collected by conventional wet electrodes, indicating the feasibility of using MDE to acquire EEG signals without the need for skin preparation in operational environments.

Table 2.1 Correlation performance comparison between MDE and wet electrodes

	Session 1: Training Session 2: Estimation		Session 2: Training Session 1: Estimation	
	Wet	MDE	Wet	MDE
Subject 1	0.95	0.96	0.90	0.92
Subject 2	0.96	0.96	0.85	0.88

2.5 Transparent MDE for Photodynamic Therapy Application

Photodynamic therapy (PDT) is administered to treat malignant tumors [32], various skin disorders [33], wound infections [34], and other diseases, as well as for cosmetic purposes in skin rejuvenation [33]. Treatment involves a photosensitizing agent, in which a visible light is irradiated to either terminate cancerous cells or cure precancerous cells instead of surgery [35]. Efficacy of PDT heavily relies on the photosensitizing agent, light, and oxygen. Physicians medicate patients and apply the photosensitizing agent on the affect part of the patient body and, then, illuminate the affected parts of a patients' body with various wavelengths of light, depending on the disease. When the photosensitizing agent is treated by light with a special wavelength, a reactive oxygen species is produced, subsequently damaging bio molecules and terminating cells [36]. Although this noninvasive and painless therapy distinguishes itself from traditional surgery, the non-uniform spatial distribution of the photochemical dose is a major limitation [37]. Tissues of the human body vary in light absorption, subsequently incurring a non-uniform light dose when irradiating the treated spot upon the affected part of skin. Additionally, the layers of skin located close to a light source receive too high of a photochemical dose, negatively affecting the human body [37]. MEMS-based dry electrode (MDE) with micro-needle array has received consideration in biomedical applications recently, especially in drug delivery [38] and physiological signal sensing. In micro drug delivery system, drug is injected through hollow needle structure into patient's tissue. The microstructure design allows the needle array pricked onto patient's skin without uncomfortable feeling. In physiological signal sensing system, micro needle array provides lower impedance and enhance the sensing system performance [20] [39]. In this work, an alternative application in optical biomedical engineering is presented by using transparent MDE. Additionally, MDE is manufactured with deep reactive ion beam etching, thick-film lithography and electroforming techniques for the shafts and tips; all-silicon fabrication process is prohibitively expensive.

This work describes a relatively low cost, easy fabrication method, which combined two-phase process for disposable transparent MDE manufacture. Therefore, the expensive ICP process was used only one time for the first MDE mold. Then, hot-embossing technique was applied to duplicate the silicon MDE into transparent micro-needle arrays. The material of duplicated micro-needle array can be polyimide (PI) or polymethylmethacrylate (PMMA), which has better light propagation capability than glass and relative low cost comparing with silicon. Furthermore, the duplication process could be repeated at least 120 times with guaranteed hot-embossing result. Carefully designed transparent MDE can avoid pain and bleeding but achieves superior light transmission efficiency. For photodynamic therapy applications, this design can significantly reduce the required irradiation power and therefore avoid additional damage to surrounding skin tissue. Practical in-vivo light

transmission experiment with two different density transparent MDE designs demonstrates the improved power transmission efficiency (PTE) of the two types of arrays is 1.41 and 1.71 times better than the condition without using transparent MDE.

Human skin structure is a layered composition, as described in section 2.2. The scattering coefficient of the *epidermis* is approximately half that of the dermis [40]. When treatment involves light irradiating with wavelength, such as a low power laser on the human skin, the skin reflects, scatters and absorbs the light simultaneously. Each layer of skin layer differs from light absorption. The propagation result of the incident light depends on the absorption of the skin. Also, when a specified intensity of received light power is required in PDT applications, high scattering and reflection could result in not only high power consumption but also extra damage to the other tissue surrounding the curing target. The Lambert–Beer law offers a simplified model of light propagation in the human skin, as shown in Fig. 2.12. When an incident light with interrogating energy I_0 illuminates into the human skin, the relationship between incident light power I_0 and the attenuated light power I can be expressed as [41]:

$$I(L) = I_0 10^{-aLC} \qquad (2\text{-}2)$$
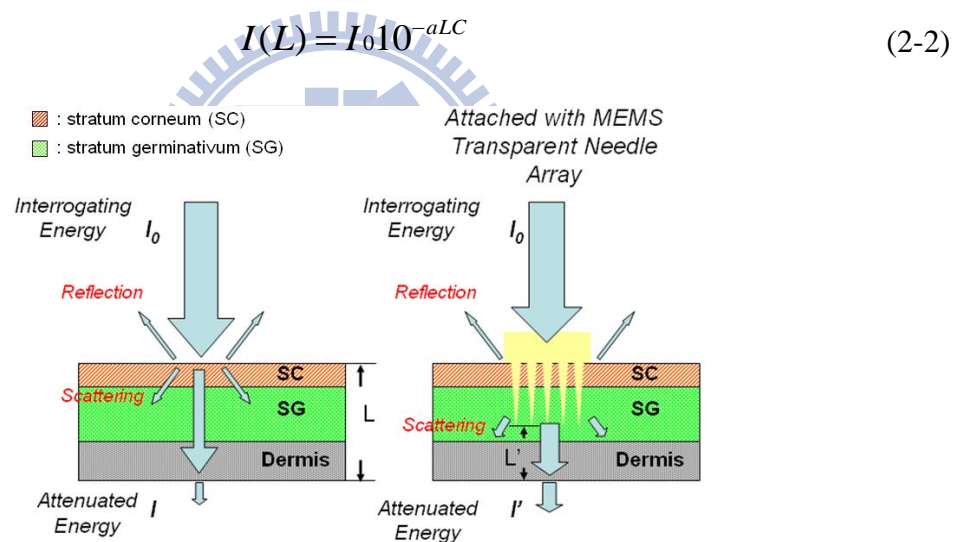
Fig. 2.12 Light propagation in skin: direct illumination or through transparent MDE

Where **L** represents the penetrating depth of light in the human skin, **a** denotes the equivalent absorption coefficient of all skin, and **C** denotes the concentration of the absorbing substance. When the transparent MDE is placed onto skin and penetrated though the SC layer into SG layer, as shown in Fig. 2.12, most of the incident light can be transferred into SG layer through the needle shaft, thus, the reflection and absorption of SC and SG layer could be reduced. Also, the penetrating depth of light is reduced from **L** to **L'**. Therefore, by using the proposed transparent MDE, the required target depth with required light power intensity could be achieved by lower interrogating energy.

The fabrication flow can be separated into two phase. The first phase is the fabrication of silicon MDE mold, which has been illustrated in previous sections. The second phase is the

repeated-and-repeated duplication process using hot-embossing technique. Fig. 2.13 illustrates the second phase fabrication process. First, polydimethylsiloxane (PDMS) was selected and spun onto Si substrate as the molding layer with curing at 90℃. Then, the silicon mold fabricated in the first fabrication phase was pressed into PDMS to form the second mold with hole-array. After well-controlled temperature recipe, the silicon array mold was removed from the PDMS mold. Notably, base on the well-controlled stated parameters including curing time and temperature, the released process is relatively easy without using any additional execution such as O2 plasma treatment which is used in previous works. And then, polymer material PMMA was injected into the PDMS mold to form the transparent needle array. Finally, the successfully performed transparent MDE was released from the PDMS mold and diced for further experiments. Fig. 2.14 shows the optical microscope photograph of transparent MDE.
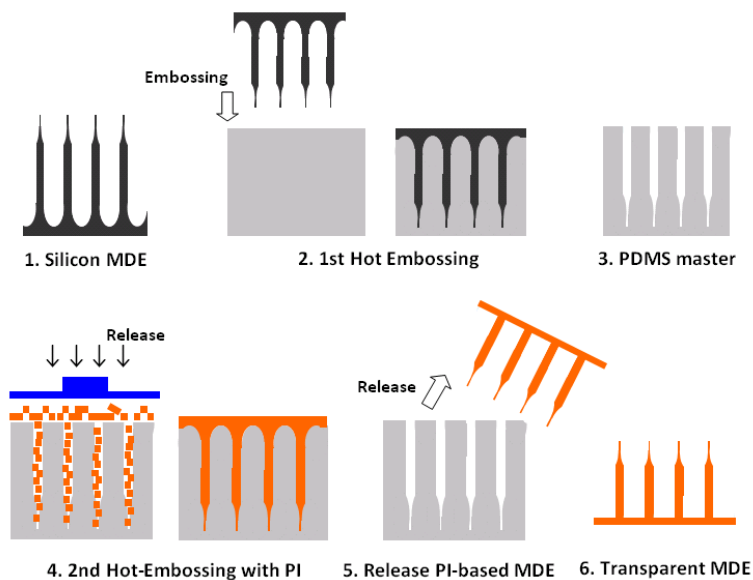
Fig. 2.13 The hot embossing process to manufacture transparent polymer based MDE
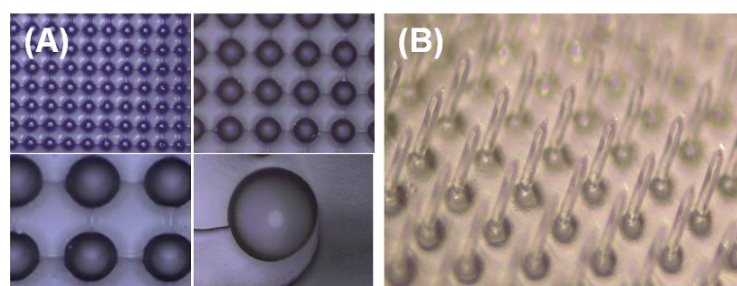
Fig. 2.14 The optical microscope photograph of transparent MDE. (A) Imprinted PDMS holes (B) PI based MDE

Fig. 2.15 (A) shows the light transmission experiment setup, which demonstrates the enhanced light transmission efficiency when using transparent MDE as light transmitting media. In this experiment, light source includes a 660nm-wavelength laser diode and

focusing lens was mounted onto finger with 3cm distance between finger and lens. The emitter power is adjusted by a current controller. Below the finger, a light receiver that can receive and measure the transmitted light power was well fitted to the backside of the finger. All experiments are performed in a dark room to eliminate the influence of excess light. To confirm the relationship between the array density and light transmission rate, two types of transparent MDE with the same area (4mm × 4mm) and different array density (needle number : 20 × 20 and 13 × 13) are prepared for test. Each array was tested under the parameter of input laser power from 2mW to 10mW with an interval of 2mW.

Fig. 2.15 (B) summarized the measurement results, where the black, blue and red lines indicate the received light power via skin, skin with rare-density array and skin with dense-density array, respectively. The results reveals that under the same LED power, the transparent micro-needle array can significantly enhance the propagation efficiency.
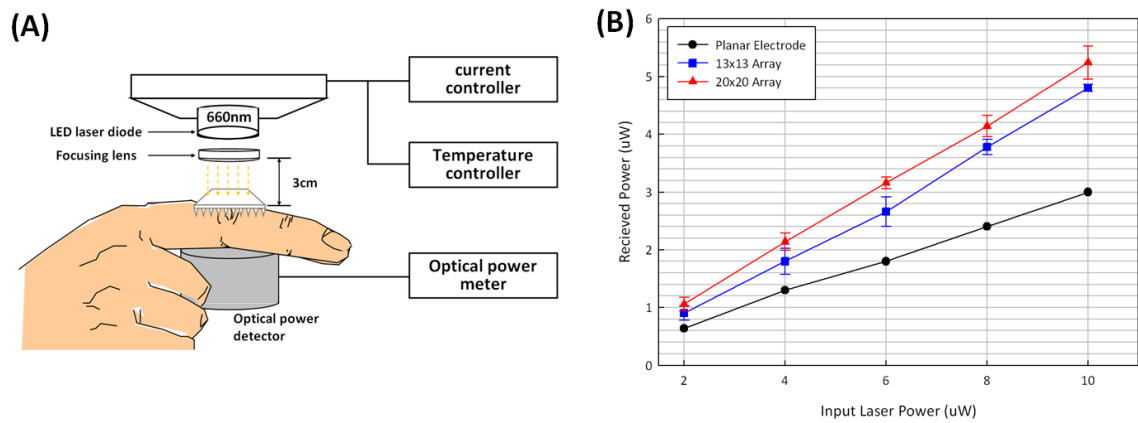
Fig. 2.15 (A) Light transmission experiment setup (B) Experiment results of input and received light intensity versus via transparent MDE with different array density

According to the experimental result, the improved PTE of dense density needle array and rare needle array are 1.41 and 1.71 times better than the condition without using transparent MDE. Note that the laser spot size on the array is about 3.5mm in diameter. In the same spotted area, the difference of received power between rare and dense density arrays comes from the different area ratio of needle part. Consider the PTE result of the rare-density array in Fig. 2.15, the area proportion of the needle part and non-needle part in the spotted area, the calculated PTE of needle part is 25 times larger than the flat part of array. By applied this result back into the calculation of the PTE of dense-density array, the calculated PTE of dense-density array is about 1.89 times better than the condition without using transparent MDE, which is very close to our measured result (1.71).

2.6 Summary

In this chapter, MEMS-based dry electrode (MDE) is presented for EEG recording. Related

experiments demonstrate its superior low electrode-skin interface impedance property without using any skin preparation. Next, a DS-MDE is also developed for better self-stabilized capability when being applied onto skin tissue. Practical application of drowsiness level monitoring in driving tasks shows reliable feasibility and competitiveness in driving error estimation examination comparing with standard wet electrodes. An alternative approach, transparent MDE, in photodynamic therapy application is realized by utilizing advanced hot-embossing method. The duplicated polymer-based micro-needle array can significantly reduce the required irradiation power and therefore avoid additional damage to surrounding skin tissue.

Chapter 3

Flexible Brain Surface Grid Electrode Array

3.1 Electrocorticography in Brain

Many neuroscience techniques have been used to study the functional relationships in the brain. In addition to the brain imaging techniques such as fMRI and PET, electrical recording techniques play an important role in brain mapping as well. ECoG recorded with non-penetrating grid electrodes are now one of a clinically applied methods to record the electrical activity in the brain. Comparing with the penetrating electrode probes, grid electrode arrays placed on the cortical surface can be used as a less invasive method in some clinical cases, e.g. in epilepsy surgery [42].

ECoG signals are composed of synchronized postsynaptic potentials (local field potentials), recorded directly from the exposed surface of the cortex. The potentials occur primarily in cortical pyramidal cells, and thus must be conducted through several layers of the cerebral cortex, cerebrospinal fluid (CSF), pia mater, and arachnoid mater before reaching subdural recording electrodes placed just below or on the dura mater (outer cranial membrane). However, to reach the scalp electrodes of EEG, electrical signals must also be conducted through the skull, where potentials rapidly attenuate due to the low conductivity of bone. For this reason, the signal magnitude of ECoG is much higher than EEG [43].

Because of the short distance between electrode and electrical source, neural activities on-set zone localization can be achieved with subdural electrodes, which is a critical imaging advantage for pre-surgical planning. ECoG offers a temporal resolution of approximately 5 ms and a spatial resolution of 1 cm [44]. It has been claimed that the spatial resolution of the present macro-size subdural electrodes usually used in clinic surgery could be substantially improved by using modern micro fabrication techniques [42].

Results in this chapter were co-worked with Yung-Feng Wang in Microsystem Control Laboratory, National Chiao-Tung University.

3.2 Design Criterion

To date, many types of grid electrode arrays have been reported for ECoG recording [45]-[49]. The materials used for electrode array structure include Polyimide, SU-8 and

Silicone, while the contact materials for sensing electrical activity usually are Gold, Platinum and Titanium Nitrite. According to the previous works, existing problems include: (1) Different level of height of the passivation layer and sensing electrode due to the thin-film process, which can affect the recording efficiency. Post processing for electrode may need. (2) Low spatial resolution due to the large electrode size/distance between electrodes. (3) Un-predictable structure distortion due to that the thickness of Polyimide varies after required high curing temperature (200-400°C).

Additionally, ECoG recording is an invasive process. Damage occurs while implantation, which consists of (1) Mechanical Damage, abrasion between sensor structure and cell tissue in setup. (2) Micromotion between skull and cortex surface, which cause abrasion in long-term implantation. (3) Immunity response cause by the implanted device [50]. Each of the damage described above can activate the glial scar in the neural tissue. The hyperplasias of the glial scar will then cover around the implanted device, provide attenuation property to the electrode and disable the functionality of the electrode eventually.

To overcome the disadvantage of the prior art, design key-point should includes

  (a) Great flexibility and softness to reduce the damage while implantation and fit to brain curvature.
  (b) Biocompatibility to reduce the immunity response.
  (c) Reasonable electrode size and density to enhance spatial resolution
  (d) Low gap of height between passivation layer and sensing electrode

In this chapter, a flexible grid electrode array is designed and fabricated by parylene-C as substrate with platinum as sensing electrode material. A three-layered array structure is presented, which formed by 10um thick parylene-C, 60nm/350nm Titanium/Platinum and 1um thick parylene-C as substrate, electrode and passivation layer. Small micro-structure thickness allows minimal implantation damage [48]. Benefit to the thin and flexible property, the grid electrode array is expected to perfectly fit the brain surface curvature for electrical activities collection.

Poly-para-xylylene (Parylene) is a macromolecule polymer. Today, over 20 types of Parylene has been developed, but for numerous reasons, only 3 were deemed commercially viable: they are Parylene-C, Parylene-N and Parylene-D. The advantages of the use of parylene as the bulk-material compared with technologies based on the use of other materials such as polyimide [51] and silicon (developed for other purposes) [52] include parylene's pinhole-free conformality, its low water permeability when compared with polyimide [53], its proven intraocular [54] and United States Pharmacopoeia (USP) Class VI biocompatibility, biostability, low cytotoxicity, its transparency, and its flexibility and mechanical strength (Young's modulus ~4 GPa) [55].

3.3 Fabrication and Characterization

Fig. 3.1 illustrates the proposed fabrication process flow: (A) Sacrificial layer deposition on the substrate. (B) Parylene-C deposition using CVD technique. (C)-(D) Platinum electrode and interconnection wire definition using lift-off technique. (E) 2nd parylene-C deposition. (F) Hard mask patterning for grid electrode array shape define. (G) Dry etching Parylene-C (H) Release structure by washing the sacrificial layer material.

(A) Sacrificial layer deposition

(E) 2nd Parylene-C deposition

(B) 1st Parylene-C deposition

(F) Hard mask patterning

(C) Platinum deposition & PR coating

(G) RIE

(D) Lift-off process

(H) Structure release

■ Si ■ Sacrificial layer ■ Parylene-C ■ PR ■ Hard mask
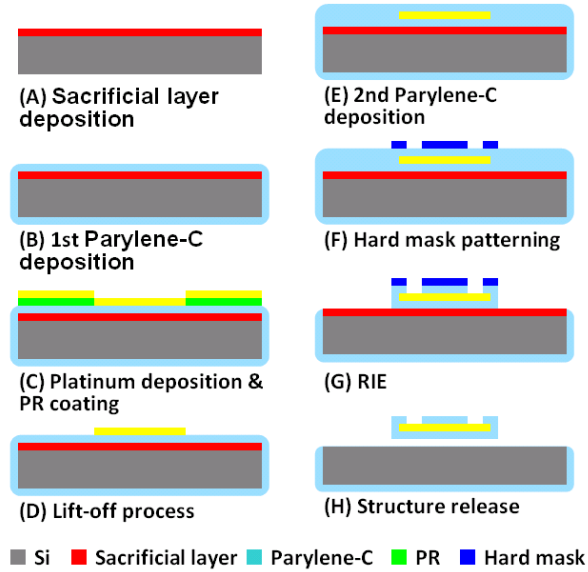
Fig. 3.1 Fabrication process flow of the presented implantable grid electrode array

Fig. 3.2 shows the photographs of the fabricated grid electrode array. (A) Top view. Right hand side denotes the recording area while left hand side of the structure is the bond pad area. (B) Packaged grid electrode array with a one cent coin. (C) Close-view of the recording electrode array. Parylene-C shows its transparent property. (D) The grid electrode array is packaged on a pre-designed PCB with connector (white) to be link to a cable wire for signal transmission. The grid array is 31.2mm in length, 4.3mm in width, and approximately 12um in thickness. Total 16 Platinum electrodes are fabricated with 500um in diameter, 750um in pitch. The width of routing wire is 100um.

To evaluate the impedance performance, the fabricated grid electrode array was characterized in physiologic saline solution (0.9% NaCl) under room temperature. The use of physiologic saline solution is because its electrolytic property is closed to implantation condition. As shown in Fig. 3.3, resulted impedance ranges between 12.6kΩ, -61.4° and 785.36kΩ, -12.32° when the testing input is set as 500mV in amplitude with scanning frequency from 40 Hz to 100 kHz. At 1kHz, test result shows that the impedance is about 1.64k Ohm and phase is -34.95°. Low impedance property induces less signal attenuation during recording therefore suit for the biopotential monitoring [56].
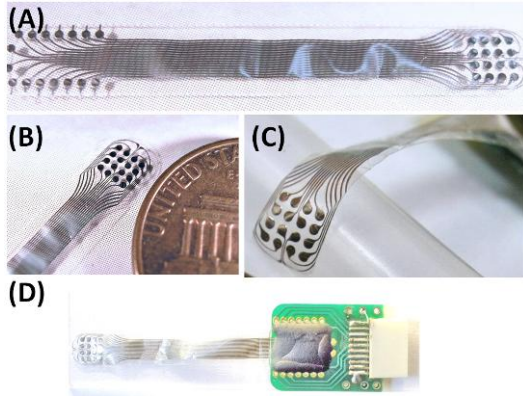
Fig. 3.2 Fabricated grid electrode array
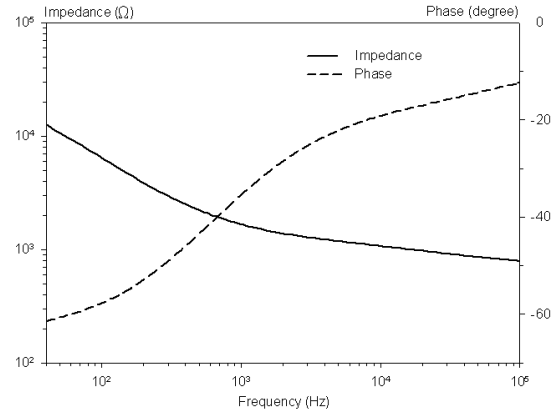
Fig. 3.3 Impedance characterization of single electrode

3.4 In-vivo Recording of Auditory Response in Rat

To demonstrate the functionality of fabricated gird electrode array, *in-vivo* experiment on auditory stimulation response recording is induced. When an authorized rat receives specialized frequency/magnitude sound stimulation, electrical response can be observed on a localized auditory area of cortex. It can be seen as neural activity happens due to the ears receive the sound and transfer into neural signals into brain and appear in auditory sensory brain area. By using the flexible grid electrode array, the interested area of brain is covered and recorded. Therefore, localized electrical response spot could be detected and characterized for functional mapping and event evaluation.

Sprague Dawley rats, aged 10–12 week old and weighting 280–350 g body weight, were used in the experiments. The animals were kept in a room under a 12:12-hr light-dark cycle with food and water provided ad libitum. All surgical and experimental procedures were reviewed and approved by the Animal Ethics Committee of the National Chiao-Tung University. The rats were anesthetized with urethane 2.0 g/kg body-weight (b.w.) intraperitoneal (i.p.). Subsequently, it was placed in a standard stereotaxic apparatus. Proposed grid electrode array are implanted over the area of auditory cortex. Fig. 3.4 (A) shows the implanted location on the rat brain [57], and the practical implantation optical photograph is presented in Fig. 3.4 (B), which shows that the presented grid electrode displayed a flexible property therefore greatly fit to the exposed brain cortex. Fig. 3.4 (C) indicates the close view of the electrode array contact area. Note that only the electrode covered area is exposed to dura layer, the rest area is skull. Fig. 3.4 (D) illustrates the channel number with respect to the location in electrode array, where ch-14, ch-15, ch-16 acts as ground and ch-1 is used as the reference channel.

The audio stimulator use signal generator, amplifier, audio amplifier and programmable attenuator (TDT-RZ5, TDT-PA5, TDT-RP2.1, TDT-SA1). The stimulate signals are 1kHz, 2kHz, 4kHz and 9kHz in frequency (in the auditory range of rat, 250-60kHz) with 25ms
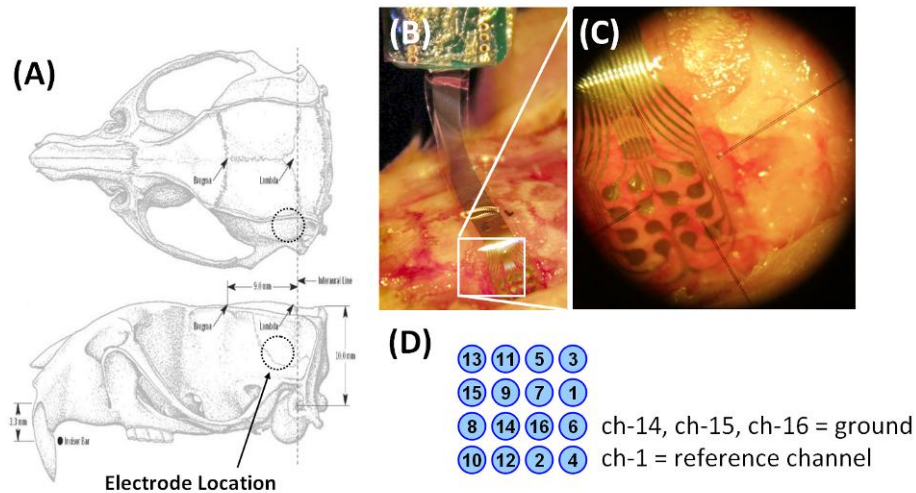
Fig. 3.4 Electrode implantation location, rat brain anatomy is adopted from reference [58]

duration, 2.5ms linear rise/fall time and 75dB sound pressure level (SPL). Every test sound is repeated for 100 times with 1 second period. Additionally, the speaker output is calibrated by a precise microphone (B&K 4149) before experiment.

Fig. 3.5 shows an example of recorded 16 channel signal in 1 second time frame. The upper green line in the figure illustrates the stimulate signal. The auditory response is then recorded and averaged to explicate the even-related evidence by software.
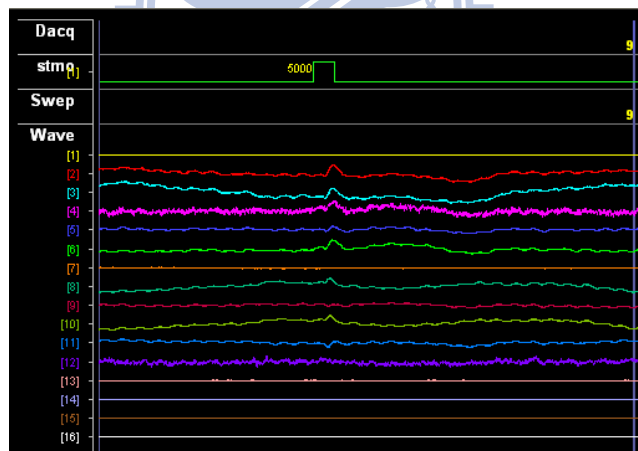
Fig. 3.5 16-channel recoding in 1 second time frame

Fig. 3.6 shows the time-magnitude plot of the averaged result of the 16 channel auditory ECoG response: (A) 1 kHz 75 dB SPL (B) 2 kHz 75 dB SPL (C) 4 kHz 75 dB SPL (D) 9 kHz 75 dB SPL. The 4 by 4 matrix boxes indicates the related electrode location on the brain. Vertical line in each box denotes the stimulation trigger marker. Four electrodes maker G (ground) and R (reference) are used as ground electrodes and reference electrodes. Fig. 3.7 presents the time-Frequency plot: (A) 1 kHz 75 dB SPL (B) 2 kHz 75 dB SPL (C) 4 kHz 75 dB SPL (D) 9 kHz 75 dB SPL. Related frequency distribution versus different electrode location can be observed in the results.
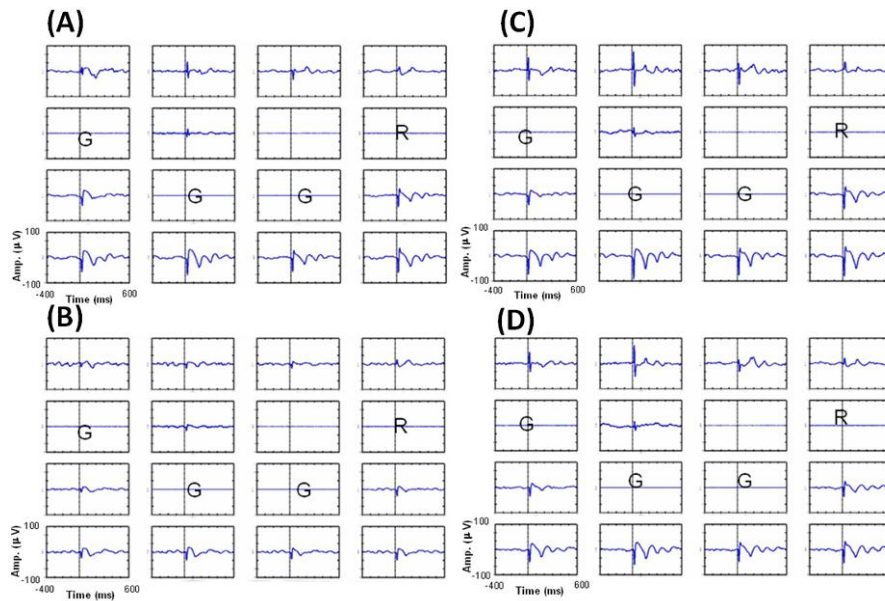
Fig. 3.6 Time-magnitude plot of the averaged 16 channel auditory ECoG response (A) 1 kHz 75 dB SPL (B) 2 kHz 75 dB SPL (C) 4 kHz 75 dB SPL (D) 9 kHz 75 dB SPL.
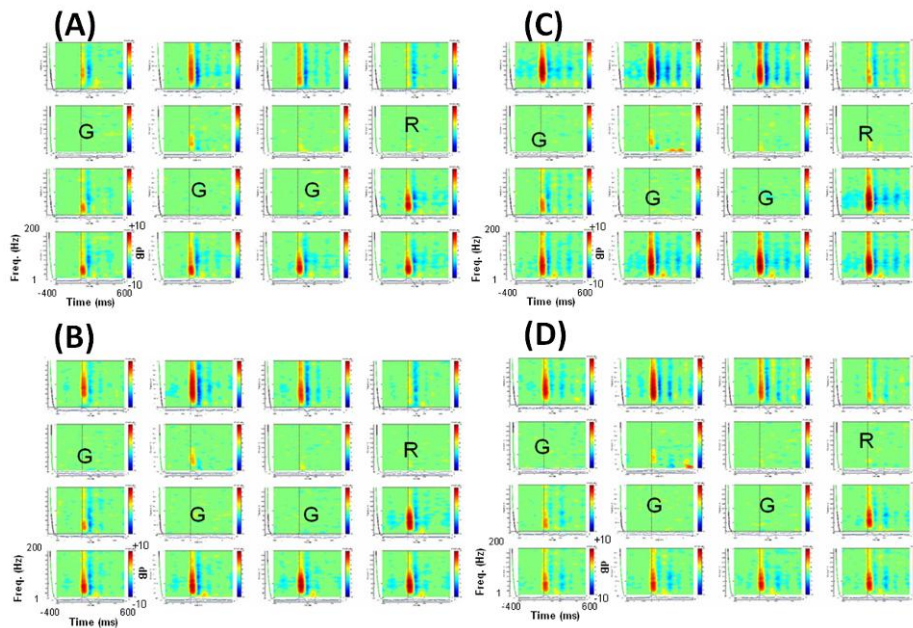
Fig. 3.7 Time-frequency plot of the averaged 16 channel auditory ECoG response (A) 1 kHz 75 dB SPL (B) 2 kHz 75 dB SPL (C) 4 kHz 75 dB SPL (D) 9 kHz 75 dB SPL.

By comparing the recorded ECoG intensity, 4 kHz stimulation shows strongest response, while 2 kHz shows less response and 1 kHz, 9 kHz have weakest response signal. Measured results shows that localized neurons discharge phenomenon (gamma activities, $30 - 200$Hz) are recorded by the presented grid electrode array. According to Fig. 3.6 and Fig. 3.7, three different auditory areas are covered by the grid electrode due to the different pattern observation. Group 1 includes 13, 11, 5, 3, Group 2 includes 8, 6, 10, 12, 2, 4, and 9, 7

27

belongs to the other group. Experiment results shows that recorded evoked potential on auditory cortex is about ±70uV, and the minimal effective sound stimulation magnitude is 20 dB SPL.

3.5 Summary

In this chapter, the implementation and characterization of a MEMS-based flexible grid electrode array utilizing parylene-C as substrate was presented for ECoG measurement applications. An un-symmetric sandwich-type structure consists of two Parylene layer (10um substrate and 1um isolation layer) and one Platinum layer was successfully fabricated. Comparing to previous works that using symmetric sandwich-type with thick isolation structure (polyimide, >20um), proposed method enhanced the adhesion property on brain cortex surface with great flexibility. Additionally, previous works suffer from the level difference between sensing electrode and passivation surface may need another electroplating post process high curing temperature (200-400℃). In this work, simplified process under room temperature and superior properties were achieved without complex and high-temperature processes.

In-vivo experiments demonstrate the recording capability of the proposed grid electrode array. Recorded auditory evoked potentials (AEPs) is ±70μV with 20dB SPL minimum sound level under general anesthesia, as well as the localized neurons discharge phenomenon (GAMA Activity, 30Hz~500Hz). The measurement result shows that the presented electrode array can cover the most of brain auditory cortex surface area, and distinguish specific signal characteristics between different electrode sites. Proposed grid array is looking forward to be used in awake animals in future works, which helps the studies on neurons degeneration, the mechanism of brain disease, and the development of the ECoG controlled BCI interface as well.

Chapter 4

Three Dimensional Neural Probe Array

4.1 3-Dimensional Electrophysiology Recording of Biological Cells

In recent years, advance micromachined/assembled micro probe arrays with electrical recording ability have come to play an essential role in exploring central neural systems. Simultaneous observation of a larger number of cell activities has become the general requirement to understand the nervous system [58]. Advances in neuroscience and neuroprosthetics now require microelectrode arrays that are able to access numerous neurons simultaneously with high spatial resolution [59]. Recording of the extracellular action potentials has been accomplished by surgically implanting neural probes into the target neurons of interest, which resulted from neural activities. Probes that could insert a large number of recording sites into neural tissues with minimal tissue damage are therefore needed. Also, the design of the probe arrays should be optimized for an experimental purpose that an electrode diameter of a few micrometers could support single-unit recording [60].

The traditional micro probes, which are made from insulated metal wires and glass micropipettes, cannot provide simultaneously multi-channel recording. The main reason is that the traditional devices function as only a single site on a single probe shaft. Some previous studies have improved the problem by thin-film lithography-based micromachining techniques since 1960s.

High-density probe arrays yielded insights into the organization and function of the neural system [61]. Silicon [62], glass [63], polymer [64] and sapphire [65] substrates have been employed as thin-film electrode probe planks. The thin-film silicon micro probe was developed many years ago for neuroscience and neural prostheses [66]. It has also been widely characterized electrically [67] and mechanically [68] for probe scaling [69], insertion force [70], tissue strain [71] and chronic brain responses [72]. The studies mentioned above provide detailed multi-channel recordings along a single plane, but lacked of full cell activity information in 3-D space [56].

To access the full cell activity that originates in the target tissue, three dimensional microprobe arrays are strongly required with precisely controlled dimensions and front-end circuitry compatibility. In other words, to achieve detailed studies of neural networks and

implementation of neural prostheses, we need to access three-dimensional volumes of tissue with three dimensional distributed recording sites. In modern neural system researches, 3D microprobe array allows the recording and mapping of the neural signal network and interconnections among the 3D brain structure. The recording and mapping would be impossible to achieve by using 2-D planar arrays [56].

Creating 3-D arrays by the assembly of 2-D parts is now the most popular method to construct a 3-D structure [59] [73-77]. The 2-D parts usually include 2-D arrays, vertical spacers and supporting platform. The supporting platform acts as a substrate, and the vertical spacers are erected on the supporting platform by tethers, joints and snap fasteners. The spacers fixed the 2-D arrays vertically on the supporting platform, and made the probe shafts pass through the holes of the supporting platform. The full 3-D structure is therefore like a PC motherboard. Additionally, active circuitry for signal processing can be designed and fabricated in the back-end of the 2-D arrays to achieve system integration. A unique handling method was developed in [76] for a dual-side, ultra-thin silicon substrate process to fabricate thin probe shafts without using doping etching stop technique. Moreover, stacked probes and PCBs by anisotropic conductive film create the connection for the dual-side wire routing and 3D structure. Therefore, each side of probe can be wired out separately. An alternative solution provided in [77] integrated the silicon probe with flexible ribbon cables by using thermosonic bonded gold bump. Also, a platform with bays and gold clips is designed to connect with probes, which results in an impressive 3D device. The comparison of three-dimensional microprobe arrays with some major design parameters is shown in Table 4.1. However, the studies mentioned above neglect the importance of smaller opening for surgery implantation. Smaller opening of skull can reduce the implantation damage to the subject, prevent the rise of brain pressure, and decrease the infection probability of the wound.

Although previous work creating 3-D arrays by assembly of 2-D arrays successfully achieves high electrode density by packaging active probes onto the supporting platform with some micromechanical packaging technique, some problems still exist. First, previous approaches that use 2-D silicon probes to form full 3-D arrays required complex schemes for assembling submillimeter parts [74]. The main problem of such techniques is that the parts (spacers and supporting platform) were all assembled in orthogonal planes. Thus, perpendicular connectors for interconnections between orthogonal planes were required for signal transmission. Ultrasonic bonding [74] and vertical snap fasteners [59] have been proposed for perpendicular transfer pads, but they suffered from complex assembly steps and precise alignment equipment for 3-D assembly. For example, precise alignment was required to make probe shafts pass through holes of the supporting platform and steady the probe onto the vertical spacers without damage during the assembly process. Second, the probe arrays were fixed only by the perpendicular bonding pads and the tenons. Low structure strength can cause stability problem in implantation. Third, the rooms between the

spacers and the 2-D probes were wasted. The volume of a 3-D structure increases rapidly when increasing the number of 2-D probes. Notably, the supporting platform also defines the minimal surgery opening requirement for implantation. Signal processing chips can either be made in the backend of the 2D arrays or mounted onto the supporting platform to achieve system integration. The former currently provides only low-end circuit processes, and the latter results in tremendously increased volume size and surgical opening for implantation. In fact, fabrication of probe array structures with advanced CMOS process in the same wafer can be a large cost because the probe area may usually much larger then the area of the backend.

Table 4.1 Comparison of 3D microprobe arrays with some major design parameters

Reference	[9-10]	[77-80]	[81]	[59, 73-75]	[77]	[76]
Substrate	Si	Epoxy, Polyimide	Polyimide/Nickel	Si	Si	Si
Dimension	3D	3D	3D	3D	3D	3D
3D method	Bulk silicon etching, out of plane	Molded tooling/ hand made	Bulk silicon etching, out of plane	Slots, platform, vertical spacer	Stacking with PCB	Platform with bays
Electrode material	Al	Tungsten/SiC	Al/Ti	Ir	Au	Au
Electronics compatibility	Yes (by Stacking & Wire-bonding)	No	No	Yes(Embedded in back-end/platform)	--	--
# of electrode per shaft/# of shaft/# of total sites	1/100/100 or 1/16/16	1/33/33 or 1/16/16	3/6/18	4/16/64 or 4/128/512 or 8/32/256	8/3/24	5/16/80
Shaft length (mm)	1.5	3-5	1.2	1.2, 2.5, 3.3	5	2
Shaft width (um)	90	50, 90, 120	160	40, 50, 144	90	--
Shaft thickness (um)	90	50, 90, 120	26	12-100	50	100
Shaft spacing (um)	400	250, 400, 450	450	200, 256	90	--
Electrode size (um^2)	--	--	400	81, 100, 1000	100	--
Electrode spacing (um)	--	--	200	24, 400	30	--
Back-end size (mm^2)	6.35×6.35	--	--	5.7×4	--	$\sim 5 \times 5$
Minimal opening required for implantation (mm^2)	$> 6.35 \times 6.35$- 1.56×1.56	$> 3.3 \times 1.05$, 1.56×1.56	$> 1.9 \times 2$	$> 2.5 \times 4.8$, 5.7×4	--	$> 5 \times 5$
Structure strength	High	Medium to high	Low	Low	Medium	Medium
Remarks	Dicing saw defined probe array	3D structure by epoxy supporting	Magnetic batch assembly	Ultra-sonic for wiring and Low profile structure	Anisotropic conductive film is used	Thermosonic bonding with ribbon cable

To improve the problems described above, this work reports a new stacking method for fabricating 3-D neural probe arrays. In this study, the 3-D orthogonal interconnection was replaced with 2-D wire bonding by the present stacking method, and the perpendicular bonding and snap fasteners which were used in previous work were no longer needed. Compared to previous work, this new stacking method can also provide reliable structure strength. ASIC chips can be substituted for spacers to increase the system integration and volume usage efficiency as well. Additionally, an anti-overflow design based on the capillary principle was exploited to avoid gel overflow onto proximate bonding pad during 3-D array assembly.

4.2 Stacked Multichip Structure Design

A new stacking method to produce three-dimensional neural probe arrays is presented in this work. This method creates 3-D probe arrays by assembling 2-D arrays and spacers layer by layer, as shown in Fig. 4.1. For a 4×4 3-D array, four 2-D arrays (gray color) with four probes in each array and three spacers (yellow color) were required. Compared to exising three-dimensional neural probe designs, the present stacking method improved the inconvenient assembly steps which include orthogonal assembly and perpendicular connection techniques. In the stacking method, the shapes of each 2-D arrays were carefully designed so they can be wire-bonded individually with different height levels. Spacers with an anti-overflow mechanism were also proposed in this paper. The present anti-overflow mechanism can also be realized on 2-D arrays if active circuit chips are used as spacers. Also, the thickness of the spacer determined the spacing between two 2-D arrays. Each planar 2-D array, electrode sites, inter-connection routing and bonding pads were located in the same plane. The bonding pads were arranged on the different sides of four 2-D probe arrays for wire bonding. Therefore, each 2-D array can be wire-bonded individually and the 3-D perpendicular bonding pads used in previous work are no longer needed.
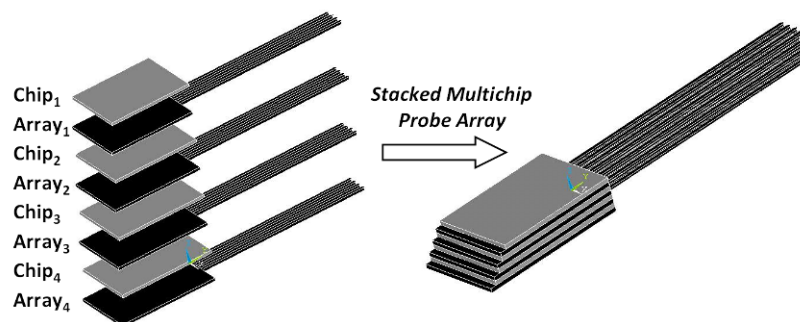
Fig. 4.1 The schematic of stacking a 4×4 3-D microprobe array

As shown in Fig. 4.2 (A), presented design needs smaller skull opening for insertion comparing with previous works. In previous works, the area of supporting platform defines the minimal surgery opening on the skull for implantation. In this design, the area needed

for insertion is almost the same as the recording target area. Presented method also has advantages of easy assembly process and high structure strength because the vertical connecters, tenons and joints that used in previous works are no longer needed. Moreover, the spacers give the possibility for multichip circuit integration by replacing them by circuitry chips.

By replacing spacers with active signal processing circuitry chips, the function of the 3-D neural probe array can be enhanced. For example, a conceptual representation of the stacked-multichip neural sensing interface is shown in Fig. 4.2 (B). For 64 recording sites sensing purpose, 4 planar arrays ($ARRAY_n$) which consist of 4 probe shafts with 4 recording sites on each probe shaft are stacked layer by layer. For each planar array $ARRAY_n$, there is a 16-channel neural amplifier (AFE_n) mounted onto itself by flip-chip bonding for amplification. Therefore, signal conditioning provided by the AFE_n can achieve reasonably high signal-to-noise ration before the neural signal being transferred into ADCs via the bonding wire. Also, the 16-channel neural amplifier has a time-division series data output to reduce the number of I/O, that is, the amount of wire-bonding.
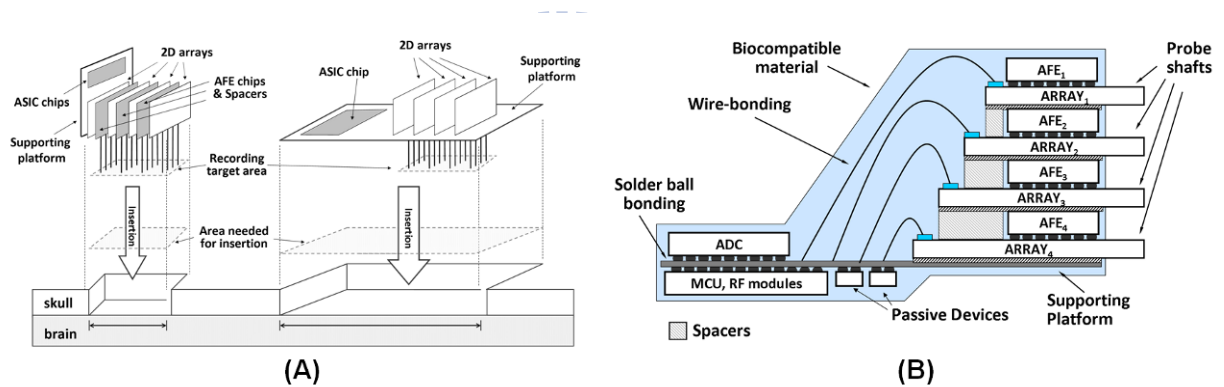
Fig. 4.2 (A) Comparison between presented stacking method and previous works using planar arrays vertically connected onto the supporting platform for constructing a 3D neural recording. (B) Conceptual representation of the multichip neural interface

The lengths of the backend of each planar array are different therefore allow each layer of planar array can be wire-bonded individually with different level of height. Since that the size of each AFE_n is always the same, there are three spacers therefore needed when stacking 4 planar arrays and 4 neural amplifier chips into a 3D neural recording device as shown in Fig. 4.2 (B). The ADCs is mounted on the supporting platform for signal digitalization and controlled by the micro-control unit (MCU). The MCU also controls the synchronization between AFEs and ADCs, and the data transmission via wireless RF modules. Related wireless data/power transmission modules and passive devices can also be mounted onto the supporting platform. Finally, biocompatible material is employed to encapsulate the implantable device for biocompatibility and electrical isolation.

Briefly speaking, in IC manufacture, larger area means higher cost. When the active

circuitry is fabricated with probe shafts in the back-end of the 2-D array, larger wafer areas are required. In the stacking design, spacers with circuitry and 2-D arrays were fabricated individually. Therefore, the stacking method can reduce the cost for circuitry integration and increase the design flexibility when modification of probes/circuitries is required for different applications. Besides, comparing with previous work, the volume usage efficiency was increased because there were no waste rooms between arrays and spacers. In short, the advantages of using active circuit chips as spacers include reducing the cost of circuitry integration, increasing the flexibility of the design and increasing the volume usage efficiency.

4.3 Fabrication, Assembly and Characterization

The key component in present stacked 3D structure is the planar neural probe arrays, which were made with multiple bio-sensing sites for neural recording [82]. The fabrication steps of the planar array are displayed in Fig. 4.3 (A) and briefly described as follows: 250nm-thick nitride deposition on 200μm-thick silicon wafer for electrical isolation. Then, 300nm/30nm-thick Pt/Ti layer was deposited and patterned by lift-off for wire interconnects on the probe shaft, following with 500nm-thick nitride deposition for encapsulation. Electrode sites and wire-bonding pads were defined by RIE. Then, 2μm-thick SiO2 was deposited by PECVD to protect the probe structure. Finally, shape of probe array was defined and released by DRIE. Fig. 4.3 (B)-(C) display the fabrication results of the planar arrays.

Another similar fabrication process which using polyimide (PI) and Cr/Au as isolation and conduction layer is also developed. The thickness of PI and Cr/Au are 3um and 1um, following with 3um-thick, electroformed Au as electrode site and bonding pad material. The Au layer is somewhat over-electroformed to ensure that the electrode was in contact with the neural tissue while implantation. Also, the final shape of the planar array was defined and released by DRIE.

When the stacking method is used to construct the 3-D neural probe arrays, the overflow adhesion gel or glue between the stacking layers may cover the proximate bonding pads and make them ineffective. Using less gel may reduce the overflow problem, but reduce the adherent strength. To solve the overflow problem of the gel, an anti-flow mechanism design was applied in the stacking method. The anti-overflow mechanism was accomplished by creating a through-silicon-via around the edges of the spacers. It uses capillary action force to prevent the gel from overflowing to the bonding pads. The mechanism functions in the following condition: when the stacking process starts, the combined parts compress the adhesion gel and force it to flow around. The flowing glue will fill the via by capillary action as it passes the via. Therefore, there is no redundant glue covering the proximate bonding pads.
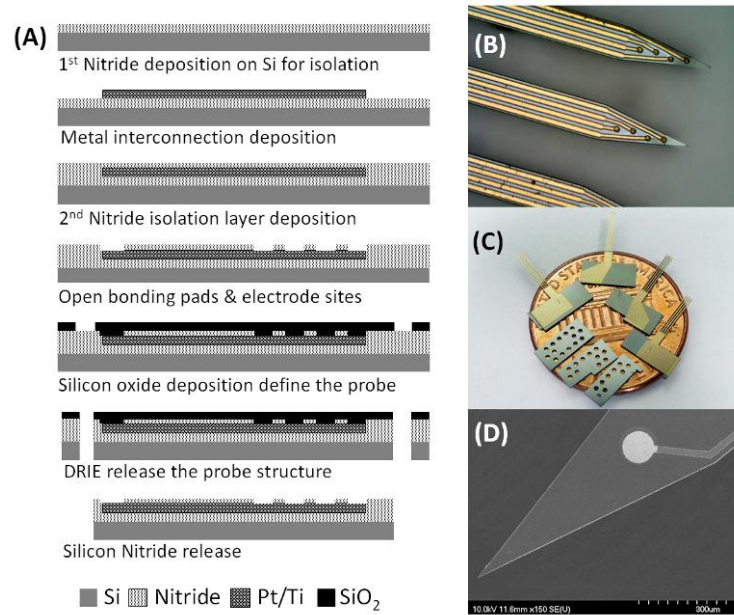
Fig. 4.3 (A)Fabrication steps of the planar array (B) FabricatedProbe tip. The tapered tip angle is about 23° (C) Fabricated parts on a one cent coin (D) Tip and electrode

The radius of the via was one of the major design parameter in preventing overflow. The formula is given by the well-known capillary action principle [83] with definition of the liquid-air surface tension, contact angle, density of the liquid, acceleration due to gravity, the height of the liquid column and the radius of the via. In this case, the maximal height of the liquid column is the thickness of the spacer (250 μm), and the liquid-air surface tension is 0.033 N/m [84], contact angle is 70° [85], density is 2,000 kg/m^3 and gravity acceleration is 9.8 m/s^2. The capillary action principle gives the radius of the via a theoretical result of 4,600 μm, which was even larger than the size of the spacer. In fact, there is some limitations should be put into consideration. For instance, the limited volume of glue, the viscosity of glue, the friction force between glue-substrate interface and the capillary force in the narrow gap between two parts will make the liquid column never reach the expected height. The final via radius was experimentally set as 250 μm to enhance the filing of the via with glue.

After probe arrays are fabricated, a pre-designed PCB is utilized as the multichip neural interface structure substrate. To demonstrate the proposed stacked-multichip neural probe array, a conceptual realization is achieved by using the dummy chips bonded with the planar arrays by thermosetting gel (EA2151, LIONTONG Inc., TAIWAN) to realize the interface structure assembly. Convenient flip-chip technology was employed to accomplish alignment, pressurization and heating process, while the thermosetting gel provided adhesive layer between arrays and dummy chips. The thermosetting glue was solidified at 185℃ in 180 seconds with an adhesive strength of 150-180 kg/cm3. The temperature is low enough to prevent the melt of Al wires in the CMOS chips during practical bonding in the future work.

The maximal placement accuracy of the flip-chip was 0.5 μm in a single bonding step. Thus, the total miss-alignment error can be neglected. Moreover, the average assembly time for a 4 × 4 3-D microprobe array by manual alignment was approximately 35 minutes (including heat curing time). In the present study, we applied about 0.26 μL of gel between spacers and arrays. The appropriate amount of the adhesion get combined the stacking well without spilling to the proximate pads.

Fig. 4.4 (A)–(G) illustrate how the anti-overflow mechanism functions in the practical assembly process. The details are displayed as follows: (A) the fabricated 2-D array (Array$_n$) was fixed on the flip-chip holder (not shown). (B) A drop of thermosetting polymer was deposited onto the 2-D probe array and the spacer (Spacer$_n$) was picked by the flip-chip bonder head and aligned. (C) Start bonding – the aligned spacer was moved downward and controlled by the flip-chip bonder head. After the spacer came into contact with the glue drop, the drop spread in random directions because it was squeezed by the spacer. (D) The spacer was moved continuously downward, and the glue filled the via by capillary force when it flowed past the via. (E) The spacer came into contact with the 2-D array. The gel bump occurred on the top of the via because the pressure from bonding. (F) The flip-chip bonding head was removed. (G) The assembly process was completed following thermal solidification of the thermosetting glue. The gel bump over the via rapidly receded after heat curing.
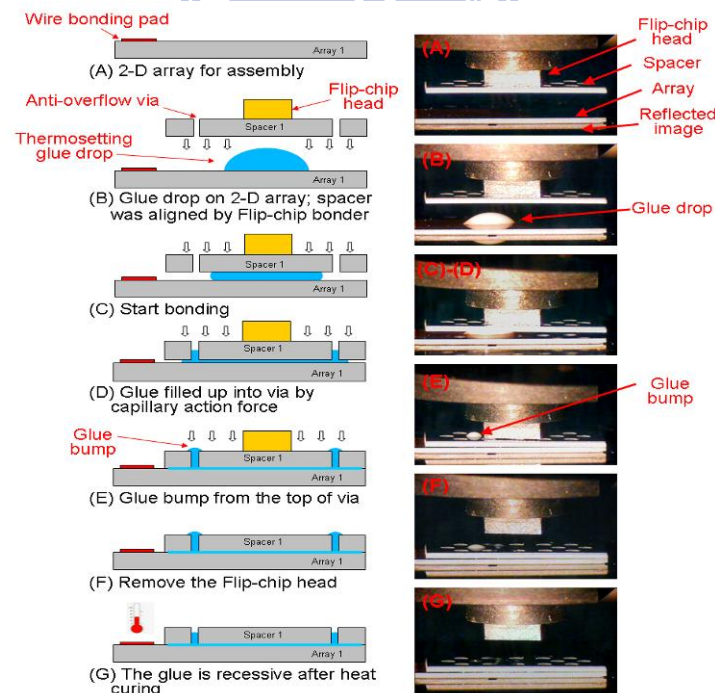
Fig. 4.4 Proposed assembly anti-flow process and related practical photographs

After wire-bonding, the wires were covered by epoxy, then, the whole device is covered by PDMS for the isolation from the implanted tissue except the probe shaft. Fig. 4.5 (A) shows the stacked 4-layer arrays with dummy chips (spacers). Note that each layer of planar array

was wire-bonded individually with different level of height. Fig. 4.5 (B) shows the packaged result of the assembled 3D neural interface structure on a one cent coin. The white connectors located on the backend of the packaged array were used for further recording experiments.
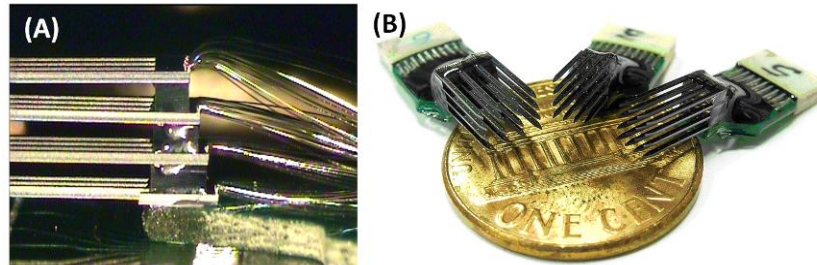
Fig. 4.5 (A) Stacked 4-layer probe array with dummy chips with wire-bonded individually in different level of height (B)Packaged 3D neural interface structure on one cent coin

Electrode impedance spectroscopy (EIS) was used to evaluate the impedance performance of the electrode-electrolyte interface [86]. When the electrode sites come into contact with tissue, electrode-tissue interface impedance was established. High interface impedance will cause signal attenuation and induce considerable thermal noise while recording. Fig. 4.6 is the test result of impedance characterization of all the 64 electrodes in physiological saline solution, which is used to simulate the recording condition. Test result shows that the impedance is around 100kΩ at 1 kHz, which is around the neuron activity frequency range.
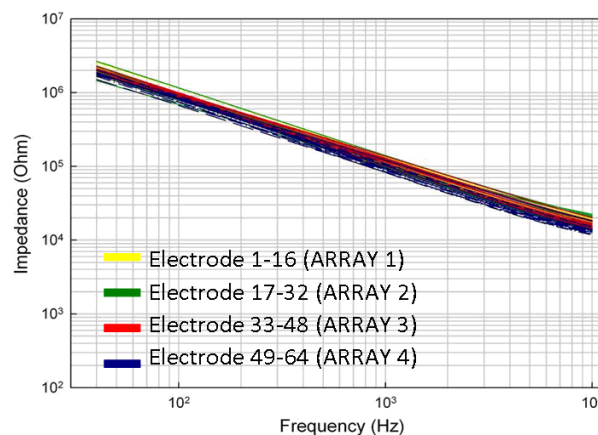
Fig. 4.6 Impedance characterization of fabricated 3D probe array

4.4 Neural Recording in Rat Brain

To demonstrate the practical function, the fabricated 3-D neural probe array was implanted into an anesthetized rat. Fig. 4.7 (A) shows the photograph of a stacked 3-D microprobe array that was inserted into the brain of an anesthetized rat by a manual 3-axis moving stage (not shown in the figure). The screw on the skull was adopted as a reference for measurement. The opening in the skull was about 2 mm by 3 mm. Fig. 4.7 (B) shows the

photomicrograph of the implantation section. The figure was modified by superimposing a lesion marker, an implantation track, and overlaying a scaled image of the microprobe array. One lesion marker arrowhead (red) was used to identify the location of the outermost recording site, in relation to the field CA1 of the hippocampus. Fig. 4.7 (C) presents neural signals from the 16-channel microprobe array, acquired with a Multi-Channel Acquisition Processor (MAP, Plexon Inc., USA). During recordings, electrical signals were passed from the headstage to an amplifier through a band-passed filtered (spike preamp filter: 450–5 kHz, gain: 15,000–20,000) and sampled at 40 kHz per channel. Fig. 4.8 presents a 50-ms segment of spontaneous neural activity derived from Fig. 4.7 (C) for clear action potential observation.
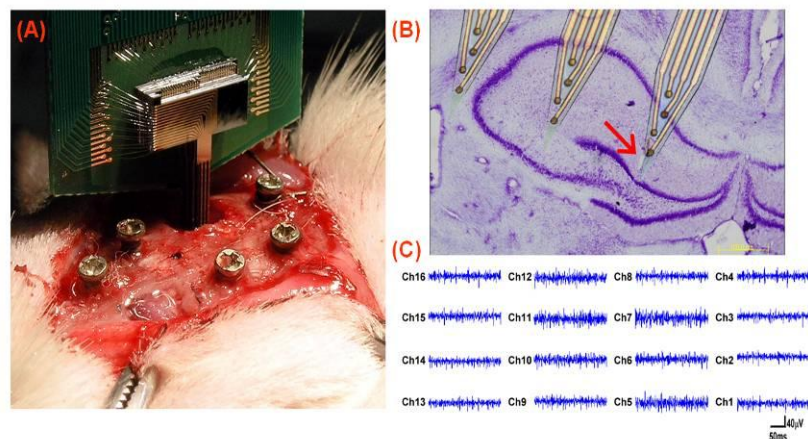
Fig. 4.7 (A) Photograph of inserted stacked 3D microprobe in brain (B) The in situ location of probes (C) The simultaneous 16-channel neural activities recording
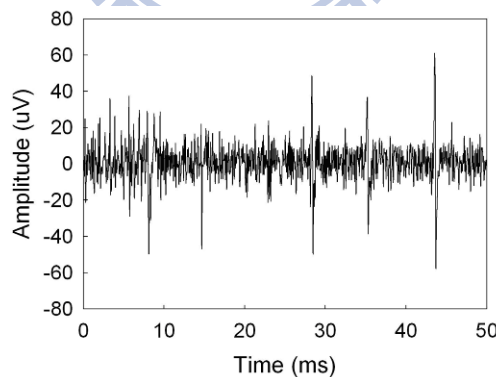
Fig. 4.8 Recorded spontaneous neural activity in motor cortex of rat

4.5 3D Signal Acquisition in Human Brain Resection Tissue

Next, real 3D neural signal propagation observation in human cerebral resection cortex layers is achieved by practical implantation after resection surgery on the cooperation with the Buddhist Tzu-Chi Hospital in Hua-Lien City, Taiwan in this study. All the study procedures follow the IRB rule of Buddhist Tzu-Chi Hospital. The patient is suffering from epilepsy seizure needed for surgery resection treatment. After the resection surgery, the

tissue was put into a prepared ACSF solution in a water bath with 37 Celsius degree with oxygen pump to keep it alive for recording. The fabricated 3D probe array was inserted into the brain tissue by a manual 3-axis moving stage. From the recording, we can build a 3D distributed spatial signal plot. Fig. 4.9 displays the recorded raw data from the resection tissue. Fig. 4.10 (A) illustrates the 3D distributed sensing electrodes diagram in implant tissue volume. Fig. 4.10 (B) shows the normalized near-field potential intensity variation observation in 4 layers in continuous time frames. However, spontaneous recording in the resection tissue lacked for even-related response to demonstrate the propagation in three dimensional volumes. Future work will also seek for stimulated recording in implant tissue for further investigation.
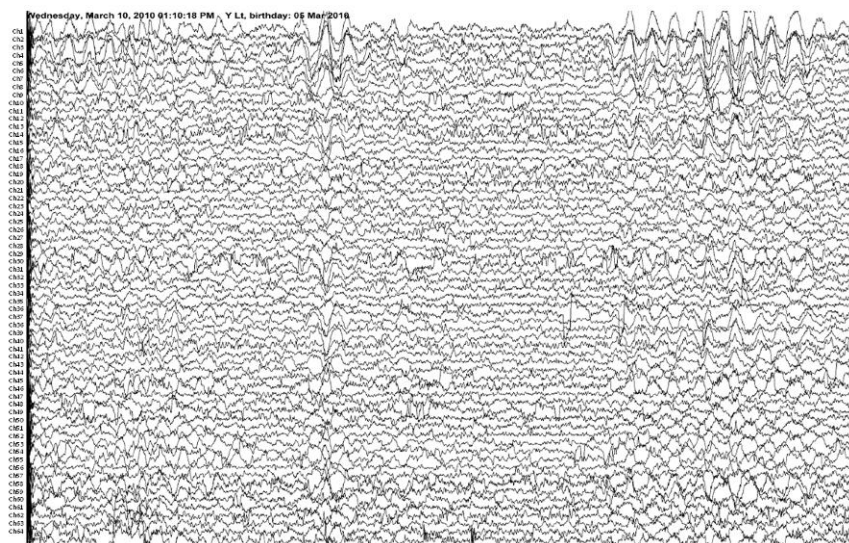
Fig. 4.9 Recorded raw data from resection brain tissue
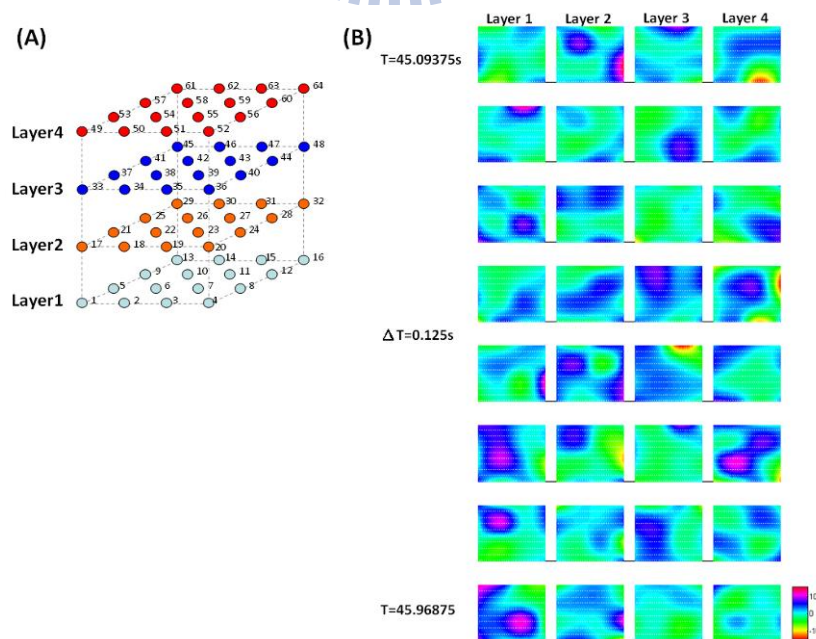
Fig. 4.10 (A) 3D distributed sensing electrodes diagram in implant tissue volume (B) Normalized LPF intensity propagation observation in 4 layers in continuous time frames

4.6 Summary

The minimal opening is the area that must be resected, including skull and dura, to fully place an implantable device onto the brain. A smaller skull opening can reduce the implantation damage such as the rise of intracranial pressure, and the probability of wound infection. In previous work, the opening area was never less than the supporting platform [74-75] to make sure all the probes were completely inserted into tissue. Therefore, the minimal surgical opening area was defined by the supporting platform in this case. Previous works requires larger the supporting platform area when ASIC chips were used for system integration [59]. In presented stacking method, the system integration will not increase the opening area because it can be accomplished by replacing spacers with ASIC chips. The opening area, depends only on the probe array dimension, is less than 1.75×1 mm^2 which can be readily shrunk by using thinner and narrow shafts.

Previous work may also induce additional tissue damage in the bottom of the platform as well. The interlocking structures, including tethers and joints, can cause the protrusion and damage to the tissue underneath [59]. For the stacked 3-D array, only probe array will be in contact with the target tissue.

The strength of the assembled structure is also an important issue in implantable device. Compared with the proposed 3D array, structures with tethers and joints used in previous work may not provide reliable strength to fix the probes on the platform during implantation [59] [74]. The thermosetting polymer in the stacked 3-D array provided an adhesive strength of 150–180 kg/cm3 after curing. Thus, sufficiently structural strength was guaranteed in the present design.

Compared with previous 3-D array studies, the advantages of using the stacking method for constructing 3-D arrays include easier assembly processes, stronger structure strength, smaller opening area and less damage to the tissue surrounding the implanting region. ASIC chips can be substituted for spacers to achieve system integration without increasing device size as well. The stacking method can therefore increase the design flexibility and enhance the volume usage efficiency.

In-vivo spontaneous neural activity recording from present stacked multichip neural sensing structure performed on anesthetized rat also illustrates the capability for practical implantable neural recording. Finally, 3D neural signal propagation observation for human cerebral cortex layers is achieved by practical implantation in excised brain tissue after resection surgery in this study. The neural signal data acquired by 3D multichip array achieves the recording and mapping of the neural signal network and interconnections among the target brain structure, which allows further studies for event-related observation. Future work will also seek for suitable solder-ball process and related biocompatible encapsulation material to realize the full concept of the stacked multichip structure.

Chapter 5

Integrated Electronics toward Microsystem

5.1 Biomedical Microsystem for Neuroprosthesis

Neuroscience engineering together with *in-vivo* real time biomedical information, such as neural activity, recorded by implant neural sensors and microsystems is ultimately crucial for bio-logical researches to identify and develop treatments for brain disorders i.e. Parkinson's disease, epilepsy, and seizures [87], as well as for developing rehabilitative prosthetic devices to help people with disabilities such as deafness [88], blindness [89], and incontinence regain at least some measure of normal function. Moreover, implantable devices have attracted the interest of the neuroscience community because of their importance in facilitating basic research on neural organization, learning, and plasticity in behaving animals. Such implantable microsystems promise to enable revolutionary advances in recording from dozens to hundreds of neurons at the cellular level [90-92]. A miniaturized long-term and reliable biomedicine implantation with versatile bio-sensors is needed for real-time prosthetics applications in free-behavior implanted subject. Current commercial products in the implants often with a heavy battery associate with the system power supply. Therefore, systems constructed by integrated circuits and bio-potential sensors with miniaturized power and volume, developed with coil inductor for RF-power receiving from an external host is highly desirable.

In this chapter, key components including inductive coupled coil for radio-frequency (RF) powering, low dropout (LDO) voltage regulator for RF-DC conversion and multi-channel analog-front-end (AFE) amplifier for biopotential conditioning are developed for the biomedical microsystem design. Section 5.2 describes the RF-powering coil and LDO regulator design, following with a 16-channel AFE chip development reported in Section 5.3. Spiral coils as a wireless power module with LDO linear regulator circuit convert RF signal into DC voltage provide a batteryless implantation for truly free-behavior monitoring. The 16-channel AFE provides pre-amplification and signal conditioning. Also, a chip-on-broad (COB) integrated microsystem consisting of fabricated AFE chip, commercial micro control unit (MCU) and wireless transceiver module are developed for the conceptual representation of the proposed microsystem.

5.2 Wireless Powering Coil and Circuitry

Fig.5.1 illustrates the electrical system architecture of the proposed RF-powering system. External component includes PA and RF power transmission coil, on-broad components involves receive coil, rectifier, smoothing capacitance and bias diode, and the on-chip component includes LDO regulator with band gap bias circuit and thermal protection circuitry. External RF power produced by a Class-E amplifier is coupled into the microsystem via a tuned LC network followed by a full-wave rectifier and regulators to produce stable 1.8V and 0.7V for system and reference supplies. 13.56MHz RF-powering is chosen due to lowest tissue absorbability to avoid damage on tissue [93].

Results in this section were co-worked with Sheng-Hsin Hung in Microsystem Control Laboratory, National Chiao-Tung University.
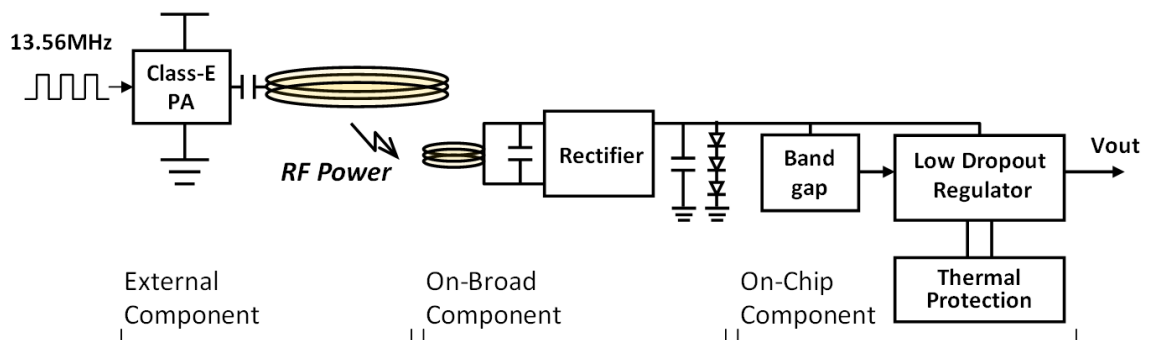
Fig. 5.1 Electrical system block diagram of the wireless powering system

5.2.1 Spiral Coil and Full-wave Rectifier

The radio frequency power is transmitted through coupled coils, which follows the electromagnetic induction of Faraday's Law. Fig. 5.2 shows the simplified schematic diagram of an inductive power transmission link [92]. L_1 is the primary coil that is attached to the skin from outside of the body, driven by an ac source V_s, which is often an efficient class-E power amplifier [94]. L_2, is the secondary coil that is implanted under the skin flap along with the rest of the implant electronics. A pair of permanent magnets, one in the center of each coil, can align and hold them together to maximize their mutual inductance M. Coil windings have parasitic resistance and capacitance associated with them, which are represented by lumped elements R_{s1} and R_{s2}. Capacitors C_{s1} and C_2 are added to form a pair of resonant LC-tank with L_1 and L_2, respectively.

Magnetic flux lines are formed around the primary coil as a result of the flow of current though it. They close their paths through the air and spread all around the coil. The voltage induced in the secondary coil, which is important for both power and data delivery to the

42
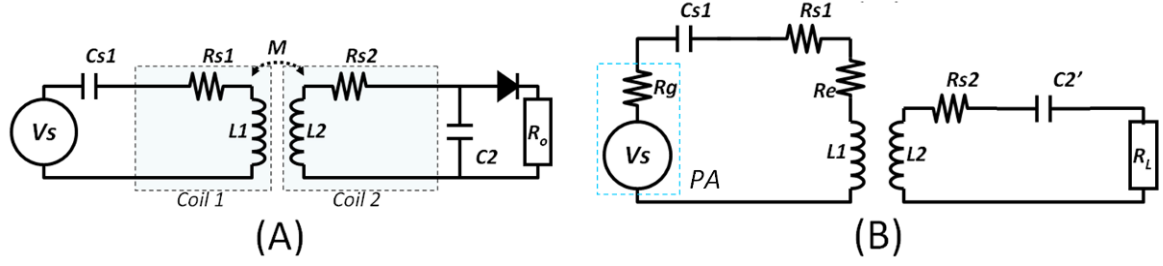
Fig. 5.2 (A) Basic schematic diagram of the inductive link (B) Equivalent circuit

implant, is due to the magnetic flux passing though the secondary coil [95]. The equivalent AC load resistance R_{ac} which will dissipate an amount of AC power equivalent to the DC power in R_o is

$$R_{AC} = R_o \Big/ 2$$

(5 - 1)

The equivalent R_L resistance can be transform into equivalent resistance

$$R_L = \left(\omega L_2\right)^2 \Big/ R_{AC}$$

(5 - 2)

Also, the equivalent resistance R_e, reflected back into the primary coil is

$$R_e = \frac{(\omega M)^2}{R_{s2} + R_L} = \frac{R_{AC} K^2 Q_1 Q_2}{R_{AC} + Q_2^2 R_{S2}} \times R_{S1}$$

(5 - 3)

where K is the coupling coefficient, which can be find by the

$$A_k = 2 - \frac{1}{1 - \left(\omega^2 C_{Total} L_2\right)}$$

(5 - 4)

Where A_k is the correction factor, and $C_{TOT} = C_{para} + C_{cable} + C_{prob}$, C_{para} is the parasitic capacitance, C_{cable} is the capacitance from connection cable, and C_{prob} is the capacitance from testing probe [96]. The coupling coefficient is

$$K = A_k \frac{V_R}{V_S} \sqrt{\frac{L_1}{L_2}}$$

(5 - 5)

where V_R is the voltage drop on the resistance load R_o. M is the mutual inductance of the coils and

$$Q_1 = \omega L_1 \Big/ R_{S1} \quad , \quad Q_2 = \omega L_2 \Big/ R_{S2}$$

(5 - 6)

are the unloaded quality factor of the two coils. The optimal efficiency is given by [97]

$$\eta_{OPT} = \frac{K^2 Q_1 Q_2}{[1 + (1 + K^2 Q_1 Q_2)^{1/2}]^2}$$

(5 - 7)

while

$$R_{S2\_Optimal} = R_{AC} \frac{\sqrt{1 + K^2 Q_1 Q_2}}{Q_2^2}$$

(5 - 8)

The coupling coefficient is determined by the coil dimension (diameter and distance), and the quality factor is defined by the coil structure and material [98]. In this work, low

43

skin-effect, low resistance single layer spiral coil structure is utilized. Then, consider of a standard 50 ohm output power amplifier, the R_{s1} can be determinated as

$$50 = R_{s1} + R_e \qquad (5 \text{-} 9)$$

Also, the effective transmission distance can be estimated by using equations [99]:

$$r_R / r_T = \sqrt{\frac{(d_T - d_R)^2 + 4D^2}{(d_T + d_R)^2 + 4D^2}} \qquad (5 \text{-} 10)$$

$$d_T = (d_R{}^2 + 4D^2)^{1/2} \qquad (5 \text{-} 11)$$

Finally, the design procedure of the inductive coupling coils is briefly described as following. First, define the coil size boundary condition for the application. Then, the maximized coupling coefficient can be determined through [97]. Quality factor is maximized by selecting appropriate conductor material. Calculate R_{AC}, $R_{S2\_Optimal}$ and R_{S1} from desired rectifier performance and powering specification. Therefore, L_1 and L_2 can be designed and obtained and realized by experimental measurements. Then, the resonance capacitance C_{S1} and C_2 can be found according to desired transmission frequency. Fig. 5.3 (A) (B) shows the optical photographs of the fabricated receive and external coils. The receiving and external powering coil, made by 24/16 AWG cupper wire, exhibit 1.5cm and 4cm in diameter, respectively. Fig. 5.3 (C) shows the measured S22 parameter and Smith chart of the developed 13.56 MHz inductive coupled spiral coils.
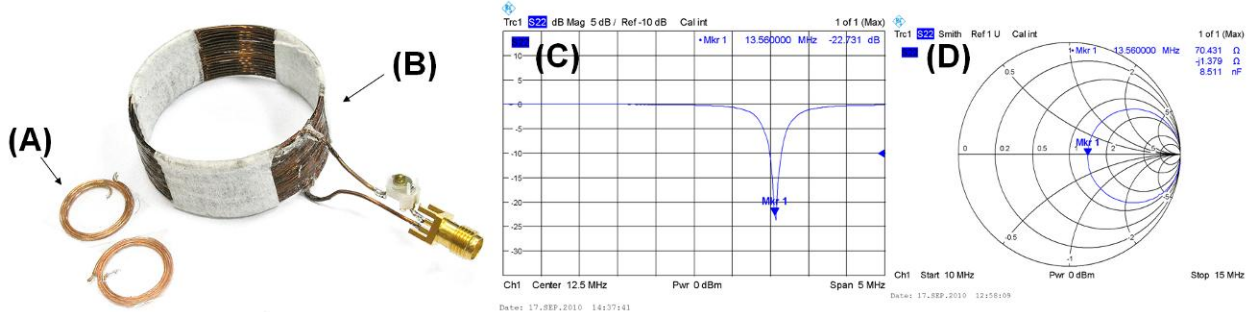
Fig. 5.3 (A) Receiving coil (B) External coil (C) Measured S22 parameter (D) Smith chart of the developed SCWPM

Rectification is processed utilizing a full-wave rectifier to convert the RF AC signal, received from the spiral coil through inductive coupling, to DC voltage level for further regulation. Here, rectifier consisting of four diodes is used, as shown in Fig. 5.4.
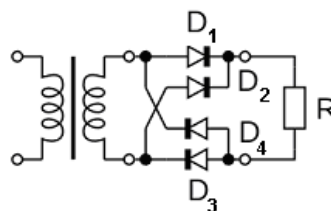
Fig. 5.4 Full-wave bridge rectifier using 4 diodes [100]

The antenna efficiency is characterized with PDMS coating as bio-protection in implanted tissue. Measurement result under conditions in air/tissue (pork) and with/without PDMS encapsulation is illustrated in Fig. 5.5, which results no obvious influence from packaging.
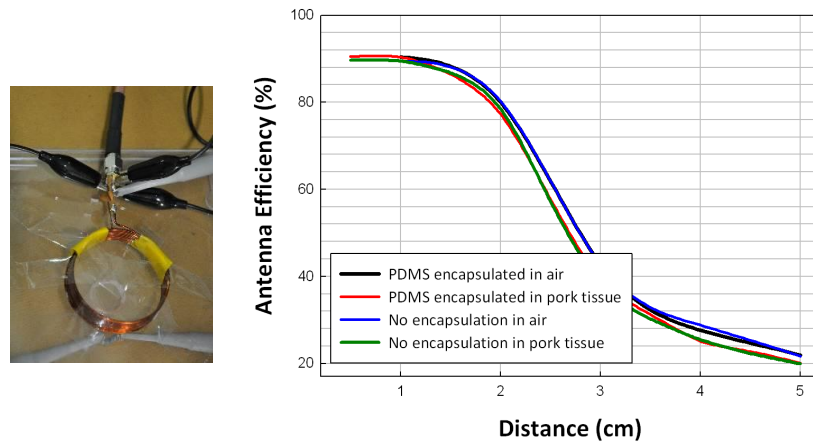
Fig. 5.5 Antenna efficiency characterization with PDMS packaging as bio-protection in implant under conditions in air/tissue (pork) and with/without PDMS encapsulation

5.2.2 RF-DC Voltage Regulator

Fig. 5.6 illustrates the block diagram of the proposed low-dropout linear regulator. The architecture is modified from a typical low-dropout regulator topology [101] with power MOSFET and thermal protection unit to enhance the driving current and avoid temperature damage on tissue. The error amplifier amplifies the voltage difference between the reference voltage and divided load voltage and switches the power MOSFET (PMOS). Output voltage is described as

$$V_{OUT} = V_{REF}\left(\frac{R_1 + R_2}{R_2}\right)$$

(5 - 1 2)
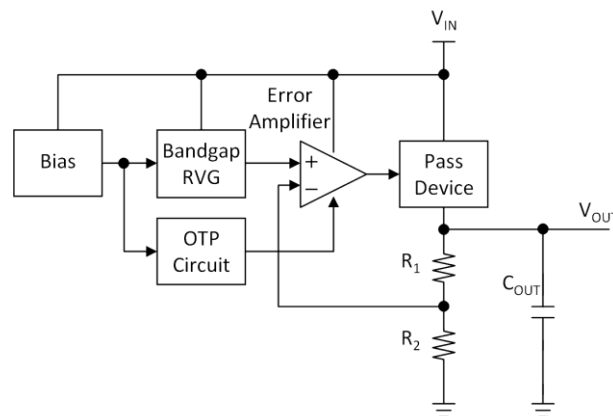
Fig. 5.6 Block diagram of the proposed low-dropout linear regulator

Another design issue in the linear regulator is the stability problem. According to the bode plot analysis, the output capacitance and its equivalent series resistance (ESR) decides the

zero point to increase the phase margin. However, the ESR must be carefully designed in appropriate range to ensure the system stability.

Fig. 5.7 shows the circuit schematic of the error amplifier. MI27 is the power MOSFET illustrated in Fig. 5.7. Also, stability is one of the design key points. In this design, ceramic capacitance with low ESR is used as output capacitance, which can cause low phase margin and lead into un-stable condition. Therefore, extra RC-compensation is introduced to enhance the system stability. In Fig. 5.7, current limitation control by two Poly resistances which is inverse proportional to current. PIP capacitance I48 and resistor RI31 are used for Miller compensation. PIP capacitance MI44 and MI39 are used as internal smoothing capacitances for spike rejection. MOS MI3 acts as output switch, which controlled by thermal protection circuit.
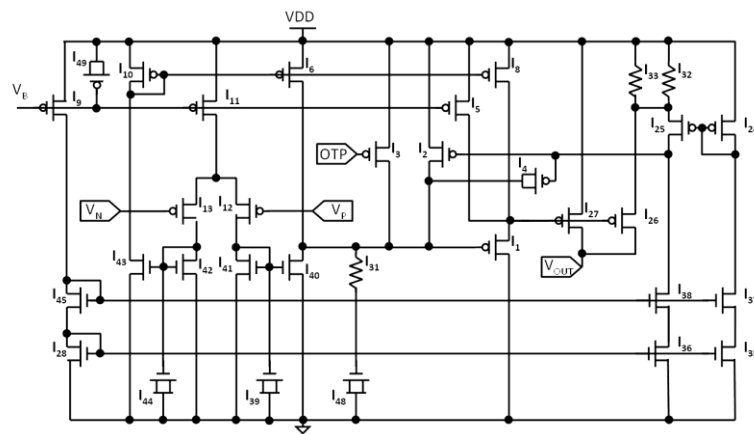
Fig. 5.7 Error amplifier circuit

Fig. 5.8 (A) shows the detailed schematic of a temperature-independent bandgap reference voltage generator (RVG) [102]. In Fig. 5.8 (A), the PNP BJT QI16 and QI17 act as negative- and positive-TC voltage devices produce a temperature independent voltage difference to the operational amplifier. A resistor RI18 is used to adjust the output V_{REF}. PIP capacitance MI31 and resistor RI2 are used for Miller compensation. MI5 and MI6 act as a startup for quicker response. MI4 is an extra gain stage for higher PSRR. MI20 is used for extra ESD protection, while the PIP capacitance MI3 used as a filter and bias. Fig. 5.8 (B) illustrates the thermal protection circuit schematic. The over-temperature protection (OTP) design is used to avoid thermal damage on tissue due to the high temperature ($> 40\,°C$) caused by the operating circuit. In Fig. 5.8 (B), RI3 is a ROND resistor in tsmc 0.35um process, which has high temperature coefficient ($PTC_1=1.51e-3$). When T raise, voltage drop on RI3 increase, then turn-on MI14, increase current flow passing MI14, turn-on MI15, pull down OTP. Hysteresis functions when temperature drop down lower than 40°C, MI14 will not off immediately due to the current provided by BJT QI2. Until the temperature is lower enough, say <37°C, voltage drop on RI3 decrease, current decrease, MI14 turn-off, MI15 off, OTP pull high.
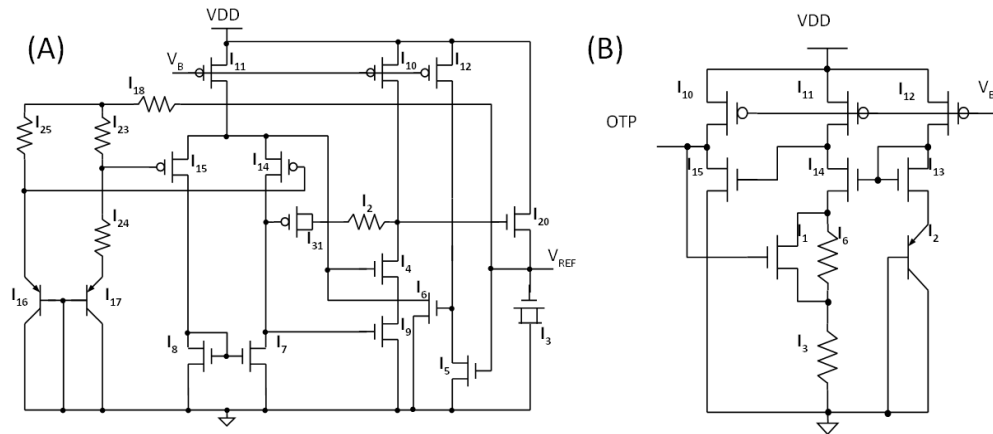
Fig. 5.8 (A) Bandgap voltage reference generator and (B) Over-thermal protection circuit

The proposed LDO regulator chip is fabricated via TSMC 0.35um 2P4M process. The die size is 1.42 x 0.95 mm^2. Fig. 5.9 (A) shows the optical microphotograph. Fig. 5.9 (B) is the test result of the Power supply rejection ratio. The measured PSRR is around 70.883 dB and 0.165 dB at 10k Hz and 13.56M Hz, respectively. Comparing to the simulation result of PSRR (~81.44 dB), the main difference is that simulation consists of only pure capacitance, but in practice, parasitic inductance does exist in the output ceramic capacitance, which decreases the high frequency performance in PSRR.
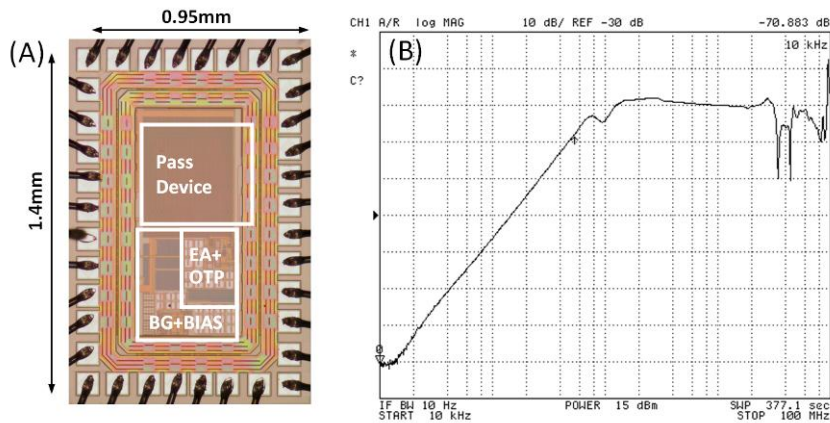
Fig. 5.9 (A) Optical microphotograph of the fabricated chip (B) PSRR of the LDO

The stability test of the LDO regulator displays the ripple and noise on the output voltage level under different current loading. Fig. 5.10 (A) Output stability observation under I_{OUT}=200 mA. Result shows that the maximal noise level is lower than 3-4mV. Low ripple and noise performance is one of the great property of linear regulator. Fig. 5.10 (B) present the output ripple caused by a current loading from 0 mA to 200mA. Output transient behaves a 308-264 mV spike, say 17%-14% variance in output voltage, under the condition V_{IN} from 3V to 6V, respectively. The output transient performance can be easily improved by increase the Quiescent Current but also increase the power consumption. Fig. 5.13 (C)

illustrates the output ripple observation under a sudden maximal current loading. The maximal output current varies under different V_{IN} condition. Result shows that the peak of the spike is less than 300mV. Line Transient is the output current ripple caused by the input voltage variance. Fig. 5.13 (D) shows the spike observation under loading current 200 mA with V_{IN} variance from 2.6V to 6V. The overall Line Regulation performance is between 1.5-4.5mV, cause 0.0833~0.25% variance in output current.
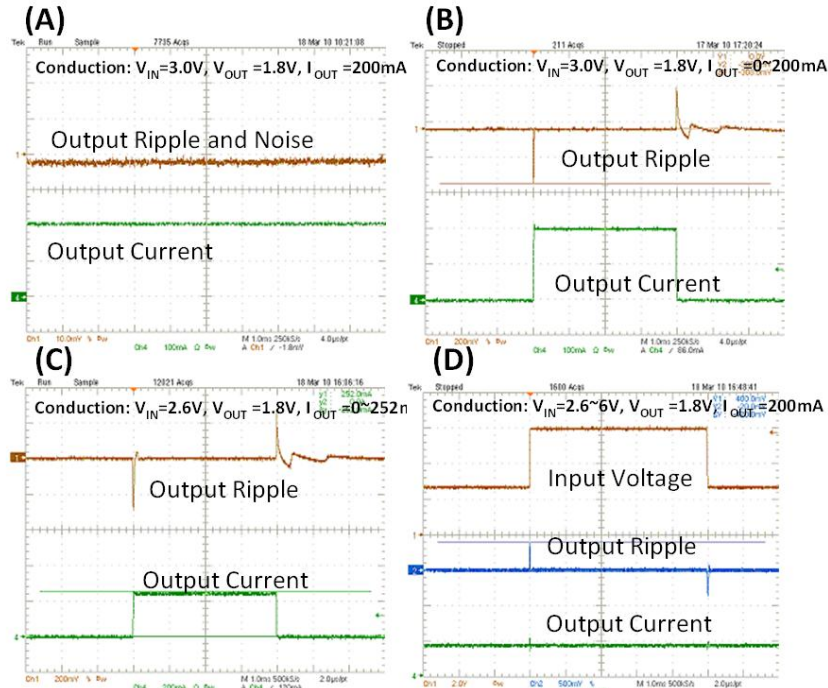
Fig. 5.10 (A) Stability test@I_{OUT}=200 mA (B) Load transient test I_{OUT}=0-200 mA@V_{IN} =3V (C) Ripple observation@load 0-252mA (D) Output spike@V_{IN} =2.6-6V

Table 1 shows the measured Load/Line Regulation result. Note that when the I_{OUT}=200mA under V_{IN} from 5V to 6V, the system is thermal shutdown due to the over thermal protection (OTP). Generally speaking, the Load Regulation is between 0.5-5mV, which is around 0.0278-0.278% variance in output voltage. Table 5 summarizes the measured performance of the presented LDO regulator comparing to other works.

Table 5.1 Load/Line Regulation Test Result

	V_{IN} (V)	2.6	3.3	4.2	5.0	6.0	Line Regulation
I_{OUT}=0mA		1.828	1.8285	1.829	1.8295	1.8285	1.5mV
I_{OUT}=50mA		1.828	1.829	1.83	1.8305	1.8305	2.5mV
I_{OUT}=100mA	V_{OUT} (V)	1.828	1.83	1.831	1.8325	1.8325	4.5mV
I_{OUT}=200mA		1.8285	1.8315	1.834	OTP	OTP	NA
	Load Regulation	0.5mV	3mV	5mV	NA	NA	

Presented chip shows low drop out voltage, wide input range with reasonable Quiescent Current. Additionally, thermal-protection (<40℃) design is also included in the present linear regulator to avoid damage in implanted target for implant device applications. Some equations used for specification comparison are listed below:

$$V_{Drop} = V_{IN} - V_{OUT} \ @ \ I_{OUT \ MAX}$$ (5 - 1 3)

$$I_{eff} = \frac{I_{OUT\_MAX}}{I_{IN\_MAX} + I_Q}$$ (5 - 1 4)

Table 5.2 Summary of LDO Regulator performance

	[103]	[104]	[105]	This work
Year	2006	2008	2010	2011
Technology (μm)	0.13	0.18	0.35	0.35
Input Voltage (V)	3~4.5	NA	2~4.5	2.6~6
Output Voltage (V)	2.8	1.2	1.8	1.8
Dropout Voltage (V)	0.199	0.2	0.2	0.125
Current Efficiency (%)	NA	99.9	NA	99
Output Current (mA)	150	200	200	0~200
Quiescent Current (μA)	114	20	30	45
Current Limit (mA)	NA	NA	NA	252
Line Regulation (mV)	1.5	NA	6	4.5
Load Regulation (mV)	17.4	NA	0.09	5
PSRR (dB)	67@20K	45@20K	NA	71@10K
Thermal Protection	No	No	No	Yes (<40℃)

5.2.3 System Characterization and Performance

After the fabrication of spiral coils and LDO regulator chip, PCB level integration is utilized for system performance characterization. To generate the RF powering, a power amplifier module using commercial chips is used to amplify the 13.56 MHz signal from a signal generator. Fig. 5.11 shows (A) Fabricated wireless powering system (B) Schematic of the class-E amplifier (C) Receive module. Fig. 5.11 (D) illustrates the temperature raise test of the SCWPM under 37℃ environmental temperature, which is used to simulate the practical implant environmental condition with maximal output current (200mA) for 1hr. Result shows that less than 2℃ raise is observed thus meet the implantation requirement [56] [106].

Finally, Fig. 5.12 shows observation on the output performance of receive coil, rectifier and LDO chip by applying 13.56M Hz signal to the. Fig. 5.12 (A) and (B) display the received power on receiving coil, the rectifier output and the LDO output when input signal on

E-class amplifier is 2.5V and 6.8V, while related output current is 0 mA and 200 mA, respectively. The maximal output ripple is around 50mV due to the low PSRR performance at 13.56M Hz. However, the ripple can be reduced down to less than 20mV is extra 0.1μF ceramic capacitance is added at the LDO output. Fig. 5.12 (C) shows the load regulation under current loading varies from 100 mA to 200 mA. The Transient voltage is about 400mV in peak. Table 5.3 shows the result of measured Load regulation of the full system.

To summarize, the spiral coils as a wireless power module is presented in power management for batteryless medical instrumentation applications. The coil and circuit design, fabrication and system implementation are exhaustively discussed in this section. Finally, practical measurement result provides the detailed performance characterization of the presented wireless power module.
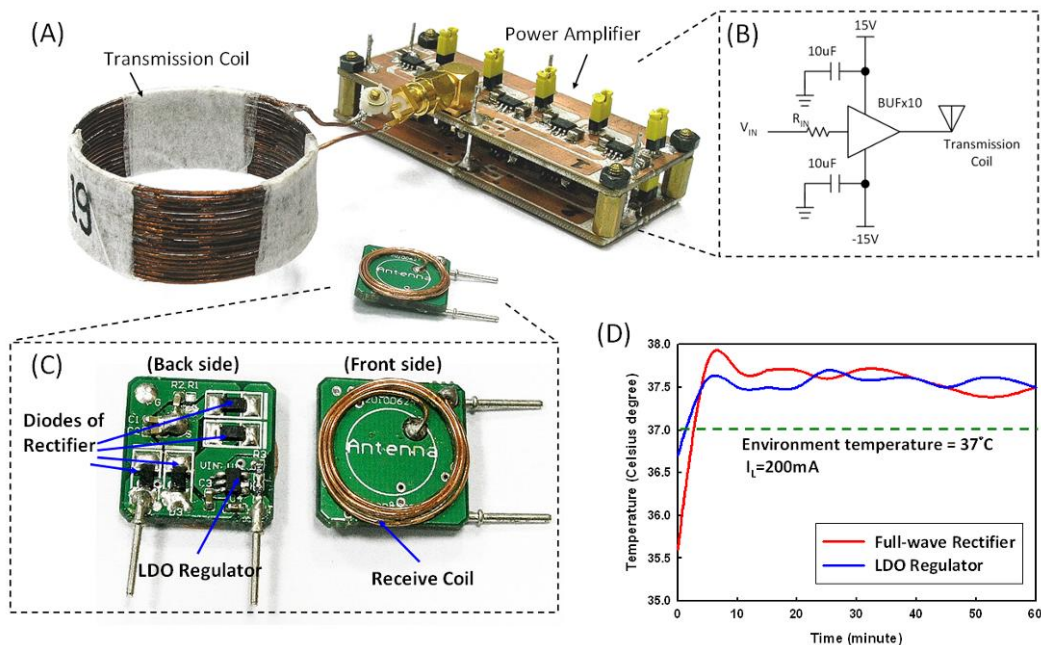
Fig. 5.11 (A) Fabricated system (B) Schematic of the class-E amplifier (C) Receive module (D) Temperature raise test under 37℃ with maximal output current for 1hr
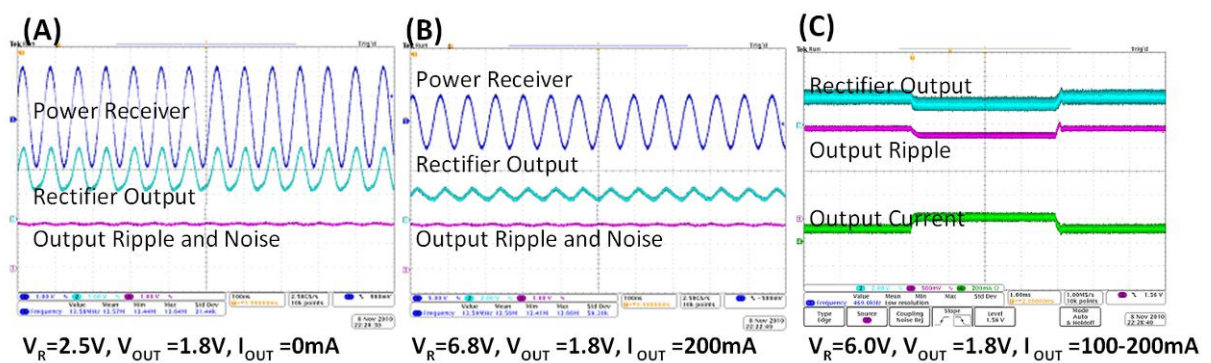
Fig. 5.12 (A) Output ripple observation under $V_{IN} = 2.5V$, $I_{OUT} = 0$ mA (B) $V_{IN} = 6.8V$, $I_{OUT} = 200$ mA (C) Load regulation under $I_{OUT} = 100\text{-}200$ mA

Table 5.3 Measured Load regulation of the system

Current	V_{OUT}
I_{OUT}=0mA	1.828V
I_{OUT}=50mA	1.827V
I_{OUT}=100mA	1.826V
I_{OUT}=150mA	1.823V
I_{OUT}=200mA	1.820V
Load Regulation	8mV

5.3 Multichannel Analog Front End

The studies of biomedical signals, or say biopotential, play an important role in the researches of biomedical science. Generally, biopotentials used in diagnoses are monitored with electrodes to acquire these electrical signals. Generally speaking, EEG and ECG are most widespread used in clinical diagnoses, and they span over a relatively low frequency range, say dc to about 100Hz [107]. The collected weak physiological signals have to be amplified, filtered and conditioned for the actual clinical applications because the raw signals are so small that they may be strongly interfered by the environmental noise. The demands of small portable, wearable and mobile sensing system are increased rapidly for the long term monitoring requirements; a low-power, low-noise amplifier system for the neural sensing applications is therefore needed.

Results in this section were co-worked with Tan-Jiun Ho and Yen-Chang Chen in Microsystem Control Laboratory, National Chiao-Tung University.

5.3.1 Differential-Difference Amplifier

The conventional instrumentation amplifier (IA) designs include traditional three operational amplifiers structure (3OIA) [108], current-balance structure (CBIA) [109-110] and differential difference amplifier (DDA) [111]. 3OIA structure requires completely resistor match to obtain very high common-mode rejection ratio (CMRR); however, mismatched resistor can cause serious CMRR debasement [112]. The advance of CBIA is its simple structure but also suffer from the requirement of current-mirror match, or the mismatch can also affect the CMRR efficiency [113].

In this work, a 16-channel analog front end (AFE) neural amplifier using DDA as first stage is presented. Comparing to previous works, resistor mismatch in the DDA design will solely influence the amplification gain. Block diagram of the complete 16-channel amplifier is shown in Fig. 5.13 (A). The differential difference amplifiers (DDA) are used as first stage of the AFE amplifier for high-CMRR and low-noise requirements. A 16:1 MUX controlled

by the clock signal allows all 16 DDAs share the same second and third amplifier/filter stages. The MUX frequency can be up to 200 kHz to scan the 16-channel inputs. The second stage and third stage use operational transconductance amplifier (OTA) to implement low-pass filter, high-pass filter and gain amplifier with selectable bandwidth and gain. The gain and low-pass filter frequency are controlled by digital signals LPF-Select and Gain-Select.

The DDA used in this work is modified from [112], and the circuit is depicted in Fig. 5.13 (B). To reduce the original flicker noise, the input stage (M_1-M_2 and M_3-M_4) are PMOS with wide width and operated in weak inversion region. The input stage transfers the input voltage into current. M_9 and M_{10} construct a common source amplifier. The differential currents flowing through M_7 and M_8 are transferred back to voltage signal by the load device M_{11} and M_{12}. The output gain stage of DDA is constructed by the two-stage amplifier (M_{13}-M_{19}), which acts as a differential-to-single- ended converter and buffer. C_1 and C_2 are Miller capacitances used to increase the phase margin. Finally, the DDA-based non-inverting amplifier is implemented from the topological placement of R_1 and R_2. The input/output relation is defined as

$$V_{out} = (R_2/R_1 + 1)V_{in}$$
(5-15)
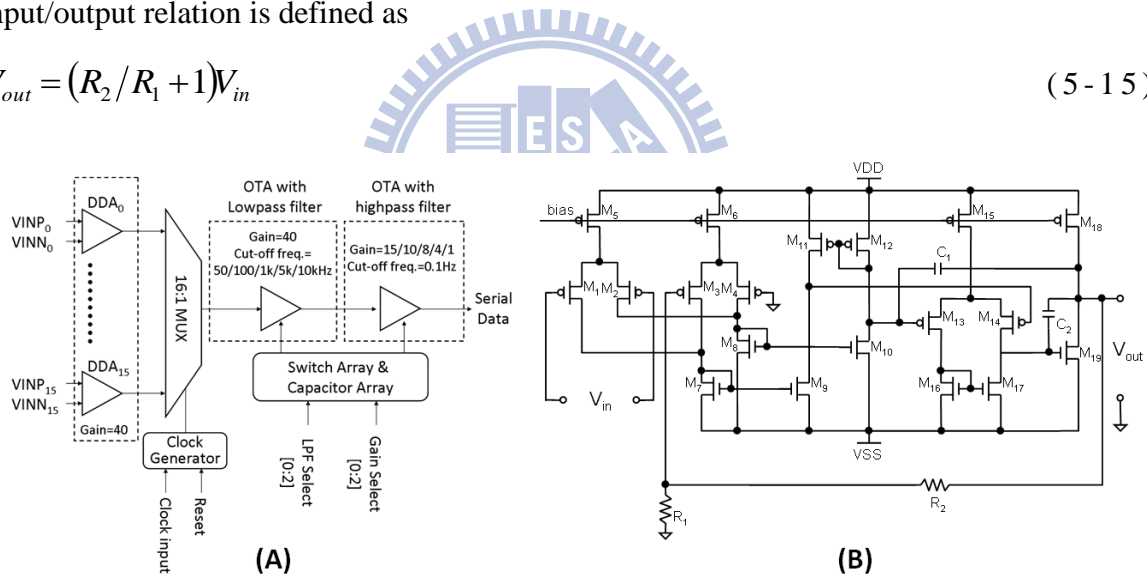
Fig. 5.13 (A) Electrical structure of the 16-channel amplifier (B) Schematic of the DDA

Fully differential OTA is used in the second and third stage of our 16-channel neural amplifier. The transconductance Gm of the amplifier is controlled by the bias current, while the input transistors are operated in the weak inversion, and the current mirror transistors are operated in the strong inversion. This design minimizes input-referred noise for a given bias current [114]. Fig. 5.14 shows the schematic of the second and third stages, which serve as a programmable gain and filter. In Fig. 5.14 (A), the filter is implemented by two series PMOS transistors across C_2 operated in sub-threshold region. The mid-band gain A_M is set by C_1/C_2=40. The cutoff frequency is approximately defined as Gm/($A_M C_L$), where Gm is the transconductance of OTA. The selectable on-chip capacitive loads provide 50 Hz

to 10 kHz low-pass cut-off frequency. Fig. 5.14 (B) shows the amplifier stage with tunable gain and fixed high cutoff frequency. The ratio of capacitors determines the gain factor of 15 to 1. The two series PMOS resister across a capacitance is employed to provide the high-pass cut-off frequency of 0.1Hz. The final output of the AFE chip is serial data, of which the packaging volume and wire bonding pads can be reduced due to less I/O numbers.
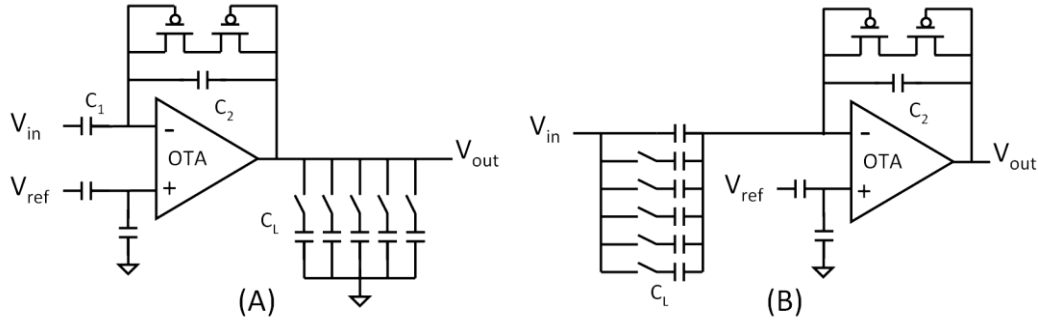
Fig. 5.14 Schematic of the 2nd and 3rd stages which serve as programmable gain and filter

5.3.3 Characterization and Performance

The 16-channel neural amplifier is fabricated using the TSMC 0.35um two-poly four-metal CMOS process and mounted on a dedicated printed-circuit board for testing. To measure the chip performance, a DAQ device (National Instruments, USA) is used to collect and transmit the 16-channel signal to a laptop. The DAQ device also provides a 200k Hz clock to operate the MUX. A microphotograph of the complete chip is shown in Fig. 5.15(A). The whole chip achieves a size of $4.18mm^2$ including pads. It drains a power of 108 μW when operating for full 16-channel neural recording. The chip operates from a single 1.8V supply without off-chip components. The measured input referred noise is 2μVrms in the band of dc to 200Hz.

Fig. 5.15 (B)-(C) shows the measured frequency response with tunable gain/band, and the noise spectrum. The measured input referred noise is 2μVrms in the band of dc to 200Hz. To verify the neural recording capability of the present AFE chip, simultaneous recording performance comparison with commercial ICs is tested by using a neural signal simulator (Cyberkinetics, US). A similar 3-stage amplifier structure which consisted of an instrumentation amplifier LT1789 (Linear Technology, US) and two operational amplifiers AD8607 (ADI, US) was used for comparison. Both present AFE chip and commercial ICs provides a band of 0.2-6k Hz with 66dB in gain. A 100-ms segment of comparison result is show in Fig. 5.15(D). In Fig. 5.15(D), the upper solid line and the lower dotted line display the results from present neural amplifier and commercial ICs, respectively. These two recordings result in a high correlation (>0.99) in average, which demonstrates the correct behavior of the present chip in neural recording.
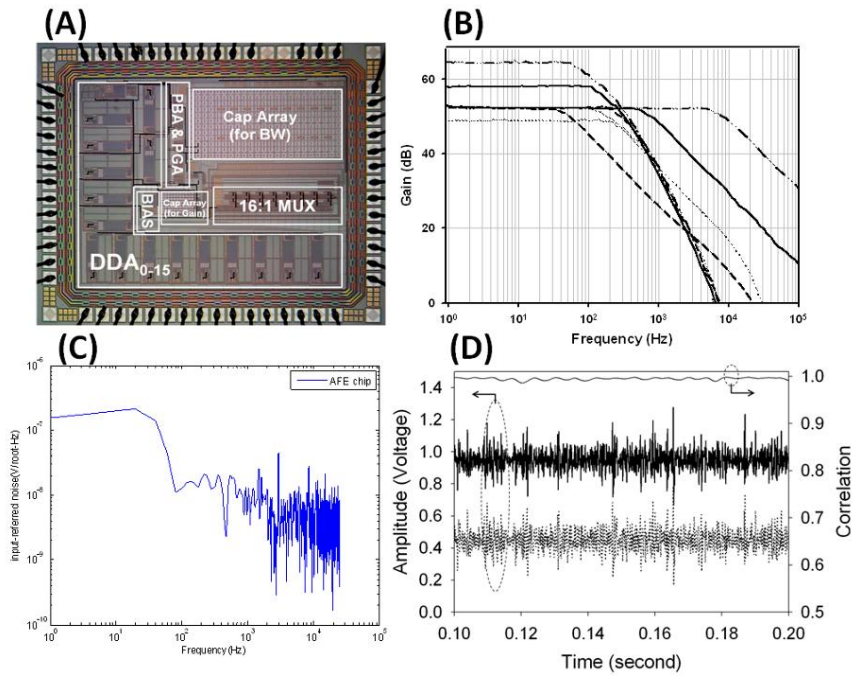
Fig. 5.15 (A) Microphotograph of the 16-ch neural amplifier chip (B) Measured tunable gain/band frequency response (C) Noise spectrum (D) Simultaneous comparison by neural simulator, upper solid line and the lower dotted line display the results from present amplifier and commercial chip. Result shows high correlation (>0.99) in average

Human EEG recording is obtained using Ag/AgCl electrodes on occipital region with amplifier ground connected to the A1, as shown in Fig. 5.16. Alpha waves (8-12 Hz) are observed when the subject's eyes were closed initially. Fig. 5.17 display the 16 channel recording consists of 9 leads of ECG from an ECG generator and 7 sinusoid waves from 10Hz to 40Hz, which are used for functional demonstration of the analog multiplexer. Table 5.4 summarizes the comparison of the measured parameters of this neural chip with those of reported multichannel works. Present neural amplifier offers technical merits of reduced supply voltage, sufficient low power per channel and reasonable low noise performance, yet offers comparable measured results such as input offset, CMRR and PSRR.
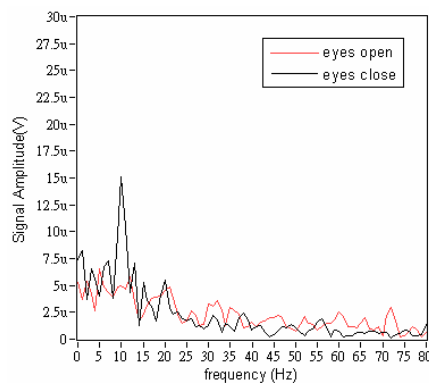
Fig. 5.16 Human EEG recording is obtained from on occipital region with amplifier ground connected to the A1, Alpha waves (8-12 Hz) are observed when eyes were closed
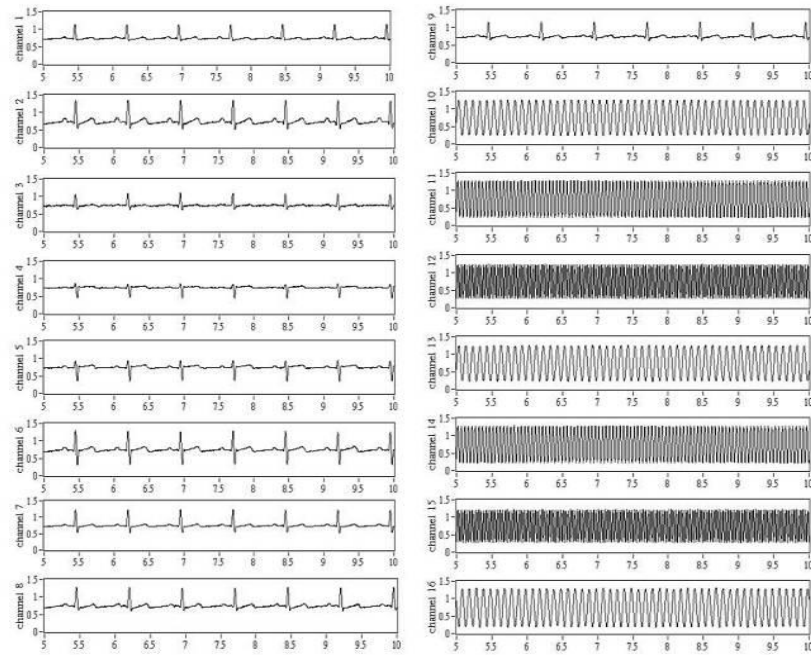
Fig. 5.17 16-channel recording consists of 9 leads of ECG from an ECG generator and 7
sinusoid waves from 10Hz to 40Hz

Table 5.4 Measured performance of the proposed neural amplifier

	This work	[115] JSSC2007	[116] JSSC2009	[117] BioCAS2009	[118] BioCAS2009	[119] BioCAS2010
CMOS Technology[μm]	0.35	1.5	0.35	0.5	0.18	0.35
Supply voltage[V]	1.8	±2.5	3	3.3	1.8	3
Number of channels	16	6	256	16	16	128
Mid-band gain[dB]	48-65	39.5	48-68	39.6	70	54-73
Highpass frequency[Hz]	0.1	0.025	0.01-70	0.2-94	100	0.5-50
Lowpass frequency[Hz]	50-6k	7.2k	500-5k	140-8.2	9.2k	500-10k
Current per channel[μA]	4.5	--	--	8	2.6	4.25
Input-referred[μVrms]	2	2.2	7	1.94	5.4	6.08
PSRR[dB]	>78	>85	--	>70	--	--
CMRR[dB]	>90	>83	--	>76	--	--
Amplifier Power[μW]	108(6.75/ch)	80(13.33/ch)	3840(15/ch)	422(26.4/ch)	8.6/ch	1632(12.75/ch)

5.3.4 Chip-on-Broad Integrated Microsystem

Wireless microsystem constructed with fabricated 16-channel neural amplifier, 8051-based
micro controller unit (C8051F582, Silicon Laboratories, Inc., USA) and Bluetooth
transceiver (BTM-182, Rayson Technology Inc., Taiwan) is implemented. Detailed system
structure is shown in Fig. 5.18. The 16-ch AFE amplifier provides signal conditioning of the
weak biopotentials, produces time-division serial data output. The series data are then
digitized and packaged with marker, wirelessly transmitted by the Bluetooth transceiver.
The C8051F582 is 8051 core based micro controller with embedded 200ksps 12-bit SAR

ADC, 50M Hz internal oscillator, operation voltage from 1.8 to 5.25V. The UART port is used to communicate with the Bluetooth module. The BTM-182 consists of CSR Bluecore-4 single chip, complete 2.4GHz radio transceiver and print circuit antenna, is designed for transparent wireless serial connection. Benefit to the easy usage of Bluetooth, single lap top is utilized as transceiver host.
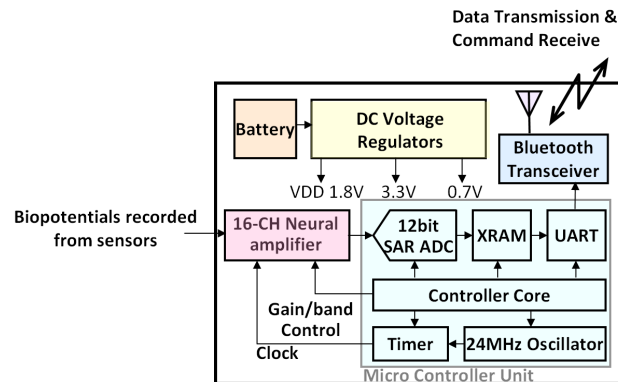
Fig. 5.18 System block diagram of the chip-on-Broad level integrated microsystem

Fig. 5.19 (A) shows the control flow of the MCU, and detailed timing chart of the data is in Fig. 5.19 (B). The microsystem provides two operation modes, say 16-channel mode and single channel mode. In the case of 16-channel mode, the clock generated by MCU is sent to the AFE amplifier to scan the 16 channels and outputs series data. A counter controlled Sample-control-Bit (SCB) is used to sample the analog data to ADC at the falling edge of the clock. Red dot in Fig. 5.19 (B) denotes the sample point for ADC. Digitalized 12-bit data is then divided into 2 bytes to UART. After 16 channels are sent, two FF which acts marker are sent into UART before next 16-channel data. The marker is used by the software to divide and reconstruct the serial data back to simultaneous 16 channels. Windows-based software is designed for receiving data from the presented microsystem and sends commands to tune on, reset or parameter setting to the microsystem. Additionally, the full system is proposed to be packed onto the back of a rat as a backpack with wires link to the implanted sensors in brain.
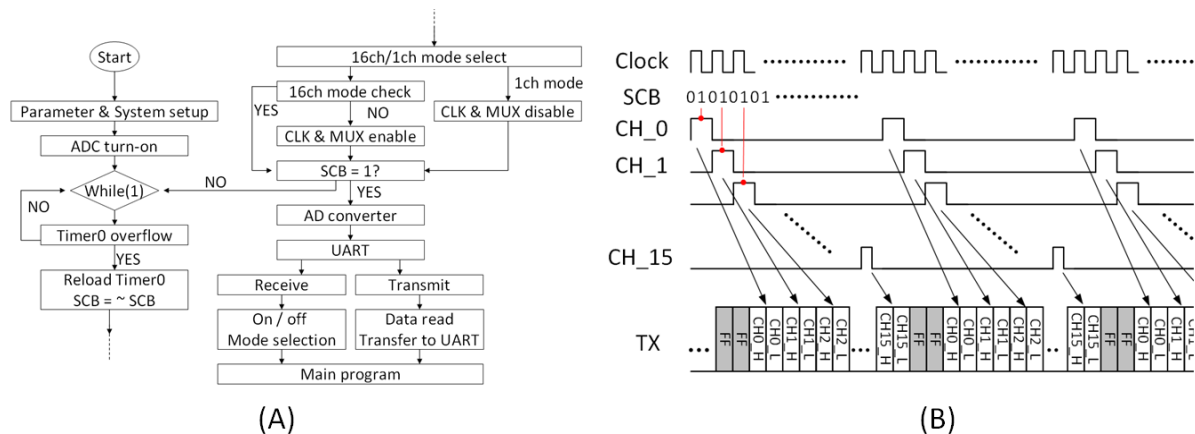
Fig. 5.19 (A) Control flow of the MCU (B) Data timing and packaging method

A 4-layer PCB design with Chip-on-Broad (COB) technique is used to divide the analog (neural amplifier) and digital circuit into two side of the PCB with two powering layer in middle layers. Fig. 5.20 shows the fabricated microsystem. The over all PCB is 39mm x 39mm in size, weight 20g with a 380mAh battery. A PCB antenna is also designed on the Bluetooth module. Commercial regulators are employed for providing 3.3V, 1.8V and 0.7V for ESD circuit, system supply and reference bias, respectively. Additionally, programming ports, power on LED, reset button and debugging circuitry are embedded on the broad for function verification although this can seriously increase system dimension.

The Flexible cable wire is designed by a 2-layer polymer-based ribbon, connected to the microsystem via a ZIP connector. As shown in Fig. 5.20, a presented 3D neural probe array is attached to the microsystem. In fact, the sensors can easily be replaced for versatile applications, such as EEG or ECoG by using presented MEMS dry electrode (MDE) or polymer based brain surface grid electrode array. Table 5.5 summarizes the microsystem specification.
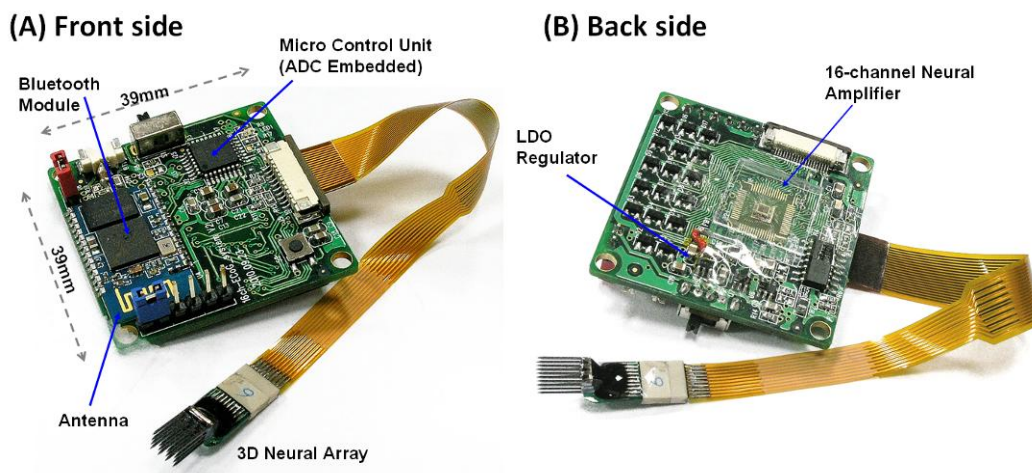
Fig. 5.20 Fabricated microsystem (A) Digital side (B) Analog side

Table 5.5 Specification list of the microsystem

Parameter	Value
Size	39 x 39 mm^2
Weight with/without battery	20g/9.96g
Resolution /Channel number	12bit/ 16 channels
AFE Gain	400-4000V/V
Sample Rate	1.25k Hz per channel
Transmission rate	Max 961200bps
Current Consumption/ Battery capacity	20 mA / 380mAh

5.4 Summary

In this chapter, key components including inductive coupled coil for wireless powering, low dropout voltage regulator and multi-channel analog-front-end amplifier for biopotential conditioning are developed for the biomedical microsystem design. Section 5.2 describes the RF-powering coil and regulator design, following with a 16-channel AFE chip development reported in Section 5.3. Spiral coils as a wireless power module with LDO linear regulator circuit convert RF signal into DC voltage provide a batteryless implantation for truly free-behavior monitoring. The 16-channel AFE provides pre-amplification and signal conditioning. Also, a chip-on-broad (COB) integrated microsystem consisting of fabricated AFE chip, commercial micro control unit (MCU) and wireless transceiver module are developed for the conceptual representation of the proposed microsystem.

Chapter 6

Conclusion

6.1 Summary of Thesis

In this dissertation, a neural sensors and microsystems toward neuroprosthesis applications is presented. Detailed designs and results for the sensors and systems are described in previous chapters. The MEMS surface-mounted dry electrode provides superior low interface impedance. Alternative MDE designs including DS-MDE and transparent MDE for better self-stability and PDT applications are also reported. Flexible gird electrode array using parylene-C as structure for ECoG recording is also proposed. *In-vivo* recording of auditory response experiment in rat demonstrates its practical effectiveness. New stacking method for assembling a 3D microprobe array is developed for implantable 3D neural recording. Proposed method provides simple process, solid structure with possibility for system integration, design flexibility and volume usage efficiency. The neural signal data acquired by 3D multichip array achieves the recording and mapping of the neural signal network and interconnections among the target brain structure, which allows further studies for event-related observation.

Wireless RF-powering electronics approach is described for implantable biomedical microsystem applications. Miniaturized spiral coils as a wireless power module and low-dropout regulator circuit convert RF signal into DC voltage for batteryless implantation with low quiescent-current and line/load regulation, high antenna/current efficiency with thermal protection to avoid damage to the implanted tissue. A 16-channel analog front end neural amplifier is also introduced, which offers technical merits of reduced supply voltage, sufficient low power per channel and reasonable low noise performance, yet offers comparable measured results such as input offset, CMRR and PSRR. Finally, an integrated microsystem using commercial micro control unit and wireless transceiver module are shown as a conceptual representation of proposed system.

To summarize, proposed sensors and electronics provide versatile neural recording and key component realization in microsystem design, as well as achieving the development of biomedical prosthesis applications by integrating with commercial modules. However, there are still plenty of rooms needed to be discovered beyond this work.

6.2 Future Work

In this dissertation, versatile neural sensors and electronics in biomedical system had been studied preliminarily. There are some prospects for the further researches including detailed neural-electrode interface studies, all-polymer based implantable sensor array for true 3D analysis, long wireless/batteryless transmission distance, system-on-chip design and reliable packaging integration with neural sensors.

Furthermore, specifically sensing electrodes for localized neuron recording require special microfabrication process with particular impedance performance. Localized neural recording can reduce the difficulty of neuron sorting or classification because of the specified signal source. Additionally, standard electrode model should be characterized by a small-signal source to compare and identify the electrode performance with prior arts. The auditory evoked potential (AEP) studied in the dissertation should also be comparing with standard samples in prior arts, as well as the neural potential recorded form different layer of the tissue by the presented neural probes. The practical survival time of the implant device is another important issue, which is considered as the next step beyond current achievements. Noise measurements and analysis is another weakness part in the work, including MDE development and the wireless neural microsystem. Comparison of the noise performance between MDE and wet electrode should be detailed investigated. The improvement of the power transmission efficiency (PTE) in photodynamic therapy by transparent MDE is clearly observed, however, current result lack of studies in the influence of the interface variance by the surface mounted MDE structure. Quantitative design procedures should be involved in the development the next generation MDE with logical and empirical verification. Finally, fully integrated system on chip design will be the ultimate goal toward neural prosthetic microsystem implementation.

Reference

[1] N. V. Thakor, "Biopotentials and Electrophysiology Measurement" in *The Measurement, Instrumentation, and Sensors Handbook*. Webster, John G., CRC Press, 1999.

[2] R. Plonsey, "*Bioelectric Phenomena*," New York: McGraw-Hill, 1969.

[3] R. Plonsey and R. C. Barr, "*Bioelectricity*," New York: Plenum, 1988.

[4] R. C. Barr, "Basic electrophysiology," in *The Biomedical Engineering Handbook*, Bronzino J., Ed., Boca Raton, FL: CRC Press, 1995.

[5] N. V. Thakor, "Neuroprosthesis: An Inspiration for Brain-Machin Interface," Lecture Note Presented at the *International Workshop on Bio-Inspired System and Prosthetic Devices*, Hsinchu, Taiwan, 2010

[6] Legatt, J. Arezzo and H.G. Vaughan, "Averaged multiple unit activity as an estimate of phasic changes in local neuronal activity: effects of volume-conducted potentials," *Journal of Neuroscience Methods*, vol. 2(2), pp.203-217, 1980.

[7] E. Niedermeyer and D. Silva F.L., "*Electroencephalography: Basic Principles, Clinical Applications, and Related Fields*," Lippincot Williams & Wilkins, 2004.

[8] B. Abou-Khalil and Musilus, K.E., "*Atlas of EEG & Seizure Semiology*," Elsevier, 2006.

[9] E.N. Brown, R.E. Kass and P.P. Mitra, "Multiple Neural Spike Train Data Analysis: State-of-The-Art and Future Challenges," *Nature Neuroscience*, vol.7, pp.456-461, 2004.

[10] P.K. Campbell, K.E. Jones, R.J. Huber, K.W. Horch and R.A. Normann, "A silicon-based, 3-dimensional neural interface—manufacturing process for an intracortical electrode array," *IEEE Transaction on Biomedical Engineering*, vol. 38, pp758-768, 1991.

[11] S. Kim, R. Bhandari, M. Klein, S. Negi, L. Rieth, P. Tathireddy, M. Toepper, H. Oppermann and F. Solzbacher, "Integrated wireless neural interface based on the Utah electrode array," *Biomedical Microdevices*, vol. 11, pp. 453-466, Apr 2009.

[12] B. Rubehn, C. Bosman, R. Oostenveld, P. Fries, T. Stieglitz, "A MEMS-based flexible multichannel ECoG-electrode array," *Journal of Neural Engineering*, vol. 6, 2009.

[13] P. Cong, N. Chaimanonart, W. H. Ko, and D. J. Young, "A wireless and batteryless 130mg 300μW 10b implantable blood-pressure sensing microsystem for real-time genetically engineered mice monitoring," *IEEE International Solid-State Circuits Conference*, 2009.

[14] A.M. Sodagar, G.E. Perlin, Y. Yao, K. Najafi and K.D. Wise, "An Implantable 64-Channel Wireless Microsystem for Single-Unit Neural Recording," *IEEE Journal of Solid-State Circuits*, Vol. 44, pp.2591-2604, 2009.

[15] M. Teplan, "Fundamentals of EEG measurement," *Measurement Science Review*, vol.2, 2002

[16] H. A. Miller, D.C. Harrison, "*Biomedical Electrode Technology*," Academic Press, NY, 1974.

[17] A. P. Spence, "*Basic Human Anatomy*," Benjamin Cummings, Redwood City, CA, 1990.

[18] S.I. Fox, "*Human Physiology*," 9th Ed., McGraw-Hill, 2004.

[19] P. Griss, E. Peter, T. Heli, M. Pekka, O. Stig and S. Göran, "Micromachined Electrodes for Biopotential Measurements," *Journal of Microelectromechanical Systems*, vol. 10, no. 1, pp. 10-16, 2001.

[20] C.W. Chang, L.W. Ko, F.C. Lin, T.P. Su, T.P. Jung, C.T. Lin and J.C. Chiou, "Drowsiness Monitoring with EEG-Based MEMS Biosensing Technologies," *Journal of Gerontopsychology and Geriatric Psychiatry*, Vol. 23, pp.107-113, Jun 1, 2010.

[21] P. Griss, E. Peter and S. Göran, "Micromachined barbed spikes for mechanical chip attachment," *Sensors and Actuators Journal-A: Physical*, vol. 95, pp.94-99, 2002.

[22] J. G. Webster, "*Medical Instrumentation Application and Design*," 3rd ed., New York: Wiley, 1998.

[23] R. Matthews, N.J. McDonald, H. Anumula, J. Woodward, P.J. Turner, M.A. Steindorf, K. Chang, and J.M. Pendleton, "Novel hybrid bioelectrodes for ambulatory zero-prep EEG measurements using multi-channel wireless EEG system," Lecture Notes in *Artificial Intelligence*, vol. 4565, pp.137–146, 2007

[24] A. Amditis, A. Polychronopoulos, "System architecture of a driver's monitoring and hypovigilance warning system," *IEEE Intelligent Vehicle Symposium*, vol.2, pp.527–532, 2002

[25] C. T. Lin, L.W. Ko, I.F. Chung, T.Y. Huang, Y.C. Chen, T.P. Jung and S.F. Liang "Adaptive EEG-based Alertness Estimation System by Using ICA-based Fuzzy Neural Networks," *IEEE Transactions on Circuits and Systems I: Regular Papers*, vol.53, pp.2469–2476, 2006

[26] W. Klimesch, "EEG alpha and theta oscillations reflect cognitive and memory performance: a review

and analysis," *Brain Research Reviews*, vol.29, pp.169–195, 1999

[27] M. Steriade, "Central core modulation of spontaneous oscillations and sensory transmission in thalamocortical systems," *Current Opinion in Neurobiology*, vol.3, pp.619–625,1993

[28] T. P. Jung, S. Makeig, M. Stensmo and T.J. Sejnowski, "Estimating alertness from the EEG power spectrum," *IEEE Transactions on Biomedical Engineering*, vol.44, pp.60–69, 1997

[29] R. Grace, V.E. Byrne, D.M. Bierman, J.M. Legrand, D. Gricourt, B.K. Davis, J.J Staszewski, and B. Carnahan, "A drowsy driver detection system for heavy vehicles," *Proceedings of the 1998 17th AIAA/IEEE/SAE Conference on Digital Avionics Systems*, 2, I36/1–I36/8. 1998

[30] S. Chatterjee, and A.S. Hadi, "Influential observations, high leverage points, and outliers in linear regression," *Statistical Science*, vol.1, pp.379–416, 1986

[31] C. T. Lin, I.F. Chung, L.W. Ko, Y.C. Chen, S.F. Liang and J.R. Duann, "EEG-based Assessment of Driver Cognitive Responses in a Dynamic Virtual-Reality Driving Environment," *IEEE Transactions on Biomedical Engineering*, vol. 54, pp.1349–1352, 2007

[32] X. Sun and W.N. Leung, "Photodynamic therapy with pyropheophorbide-a methyl ester in human lung carcinoma cancer cell: efficacy, localization and apoptosis," *Photochem Photobiol*, vol. 75, no. 6, pp. 644-651, 2002.

[33] Goldberg DJ, "Photodynamic therapy in skin rejuvenation," *Clinics in Dermatology*, vol. 26, pp.608-613, November, 2008.

[34] M. R. Hamblin, D.A. O'Donnell, N. Murthy, C.H. Contagand and T. Hasan, "Rapid Control of wound infections by targeted photodynamic therapy monitored by in vivo bioluminescence imaging," *Photochem Photobiol*, vol. 75, no. 1, pp. 51-57, February, 2002.

[35] J.P. Tardivo, A.D. Giglio, C.S. Oliveira, D.S. Gabrielli, H.C. Junqueira, D.B. Tada, D.Severino, R.F. Turchiello, and M.S. Baptista, "Methylene blue in photodynamic therapy: From basic mechanisms to clinical applications," *Photodiagnosis and Photodynamic Therapy*, vol. 2, pp. 175-191, 2002.

[36] D.J. Granville and D.W. Hunt, "Porphyrin-mediated photosensitization0-taking the apoptosis fast lane," *Current Opinion in Drug Discovery and Development*, vol. 3, pp. 232-243, 2000.

[37] B.Y. Kogan, , "Nonlinear photodynamic therapy. Photochemical dose levelling within a tumor by saturating a photosensitizer's triplet states," *Photochemical and Photobiological Sciences*, vol. 3, pp. 360-365, February, 2004.

[38] H. Gardeniers, R. Lüttge, E. Berenschot, M.J. Boer, S.Y. Yeshurun, M. Hefetz, R. Oever van 't and A. Bergden, "Silicon micromachined hollow microneedles for transdermal liquid transport," *Journal of Microelectromechanical System*, vol. 12, pp. 855-862, 2003.

[39] C.L. Chang, C.W. Chang, C.M. Hsu, C.H. Luo and J.C. Chiou, "Power-efficient wireless sensor for physiological signal acquisition," *Journal of Micro/Nanolithography, MEMS and MOEMS*, vol. 8, 02110, 2009.

[40] M. Shimada, Y. Yamada, M. Itoh and T. Yatagai, "Melanin and blood concentration in a human skin model studied by multiple regression analysis: assessment by Monte Carlo simulation," *Physics in Medicine and Biology*, vol. 46, pp. 2397-2406, 2001.

[41] J.B. Dawson, D.J. Barker, D.J. Ellis, J.A. Cotterill, E. Grassam, G.W. Fisher and J.W. Feather, "A theoretical and experimental study of light absorption and scattering by in vivo skin," *Physics in Medicine and Biology*, vol. 25, pp. 695-709, 1980

[42] J. Kitzmiller, D. Beversdorf and D. Hansford," Fabrication and testing of microelectrodes for small-field cortical surface recordings," *Biomedical Microdevices*, vol.8, pp.81–85, 2006

[43] K. Hashiguchi, T. Morioka, F. Yoshida, Y. Miyagi, S. Nagata, A. Sakata and T. Sasaki, "Correlation between scalp-recorded electroencephalographic and electrocorticographic activities during ictal period," *Seizure*, vol. 16, pp.238–247, 2007

[44] E. Asano, C. Juhász, A. Shah A, O. Muzik, D.C. Chugani, J. Shah, S. Sood and H.T. Chugani, "Origin and Propagation of Epileptic Spasms Delineated on Electrocorticography," *Epilepsia*, vol. 46, pp.1086-1097, 2005

[45] B. A. Hollenberg, C.D. Richardsa, R. Richardsa, D.F. Bahra and D.M. Rectorb, "A MEMS fabricated flexible electrode array for recording surface field potentials," *Journal of Neuroscience Methods*, vol. 153, pp. 147-153, 2006.

[46] M.L. Katiuska, M.M. Buitrago, B. Hertler, M. Schubring, F. Haiss, W. Nisch, J.B. Schulz and A.R. Luft, "Cortical stimulation mapping using epidurally implanted thin-film microelectrode arrays," *Journal of Neuroscience Methods*, vol. 161, pp. 118-125, 2007.

[47] S. Myllymaa, K. Myllymaa, H. Korhonen, J. Töyräs, J.E. Jääskeläinen, K. Djupsund, H. Tanila and R. Lappalainen, "Fabrication and testing of polyimide-based microelectrode arrays for cortical mapping of evoked potentials," *Biosensors and Bioelectronics*, vol. 24, pp. 3067-3072, 2009.

[48] B. Rubehn, C. Bosman, R. Oostenveld, P. Fries and T. Stieglitz, "A MEMS-based flexible multichannel ECoG-electrode array," *Journal of Neural Engineering*, vol. 6, no. 3, 2009.

[49] Y. Y. Chen, H.Y. Lai, S.H. Lin, C.W. Cho, W.H. Chao, C.H. Liao, S. Tsang, Y.F. Cheng and S.Y. Ling, "Design and fabrication of a polyimide-based microelectrode array: application in neural recording and repeatable electrolytic lesion in rat brain," *Journal of Neuroscience Methods*, vol. 182, pp. 6-16, 2009

[50] L. Grand, L. Wittner, S. Herwik, E. Göthelid, P. Ruther, S. Oscarsson, H. Neves, B. Dombovári, R. Csercsa, G. Karmos and I. Ulbert, "Short and long term biocompatibility of neural silicon probes," *Journal of Neuroscience Methods*, vol. 189, pp. 216-229, 2010

[51] T. Stieglitz, W. Haberer, C. Lau and M. Goertz, "Development of an inductively coupled epiretinal vision prosthesis," in *Proceedings of EMBS 2004*, pp. 4178-4181.

[52] A. Hoogerwerf and K. Wise, "A three-dimensional microelectrode array for chronic neural recording," *IEEE Transaction on Biomedical Engineering*, vol. 41, pp. 1136–1146, 1994.

[53] J.J. Licari and L.A. Hughes, "*Handbook of polymer coatings for electronics: chemistry, technology, and applications*", 2nd ed. Park Ridge, N.J., U.S.A.: Noyes Publications, 1990.

[54] D. C. Rodger, J.D. Weiland, M.S. Humayun and Y.C. Tai, "Scalable flexible chip-level parylene package for high lead count retinal prostheses," in *Proceedings of Transducers*, pp. 1973-1976, 2005

[55] D.C. Rodger, L. Wen, H. Ameri, A. Ray, J.D. Weiland, M.S. Humayun and Y.C. Tai, "Flexible Parylene-based Microelectrode Technology for Intraocular Retinal Prostheses," In *Proceedings of IEEE NEMS Conference*, pp.743-746, 2006

[56] K. D. Wise, A.M. Sodagar, Y. Yao, M.N. Gulari, G.E. Perlin and K. Najafi, "Microelectrodes, Microelectronics, and Implantable Neural Microsystems," *Proceedings of IEEE,* vol. 96, pp.1184-1202, 2008

[57] G. Paxinos and C. Watson, *The Rat Brain in Stereotaxic Coordinates*: ACADEMIC PRESS, 2008

[58] M. Chcurel, "Windows on the brain," *Nature*, vol. 412, pp.266-268, 2001

[59] Y. Yao, M. N. Gulari, J. A. Wiler, and K. D. Wise, "A microassembled low-profile three-dimensional microelectrode array for neural prosthesis applications," *Journal of Microelectromechanical Systems*, vol.16, pp. 977-988, 2007

[60] J.D. Green, , "A simple microelectrode for recording from the central nervous system" *Nature*, 182, pp. 962, 1958

[61] K.D. Wise, J.B. Angell and A. Starr, "An integrated-circuit approach to extracellular microelectrodes". *IEEE Transaction on Biomedical Engineering*, BME-17, 238-247, 1970

[62] K. Najafi, K.D. Wise and T. Mochizuki, "A high-yield IC-compatible multichannel recording array." *IEEE Transactions on Electron Devices*, 32, 1206-1211. 1985

[63] K.E. Jones, P.K. Campbell and R.A. Normann, "A glass silicon composite intracortical electrode array." *Annals of Biomedical Engineering*, 20, 423-437. 1992

[64] A. Mercanzini, K. Cheung, D.L. Buhl, M. Boers, A. Maillard, P. Colin, J.C. Bensadoun, A. Bertsch, and P. Renaud, "Demonstration of cortical recording using novel flexible polymer neural probes." *Sensors and Actuators A: Physical*, 143, 90-96. 2008

[65] G.A. May, S.A. Shamma,; R.L. White, "Tantalum on sapphire micro-electrode array". *IEEE Transactions on Electron Devices*, 26, pp.1932-1939. 1979

[66] K.D. Wise," Silicon microsystems for neuroscience and neural prostheses." *IEEE Engineering in Medicine and Biology Magazine*, 24, 22-29. 2005

[67] K.L. Drake, K.D. Wise, J. Farraye, D.J. Anderson and S.L. Bement, "Performance of planar multisite microprobes in recording extracellular single-unit intracortical activity". *IEEE Transaction on Biomedical Engineering*, 35, 719-732, 1988

[68] K. Najafi and J.F. Hetke, "Strength characterization of silicon microprobes in neurophysiological tissues". *IEEE Transaction on Biomedical Engineering*, 37, 474-481. 1990

[69] K. Najafi, Ji, J. and K.D. Wise, "Scaling limitations of silicon multichannel recording probes." *IEEE Transaction on Biomedical Engineering*, 37, 1-11. 1990

[70] K.J. Paralikar and R.S. Clement, "Collagenase-aided intracortical microelectrode array insertion: Effects on insertion force and recording performance". *IEEE Transaction on Biomedical Engineering*, 55, 2258-2267. 2008

[71] C.S. Bjornsson, S.J. Oh, Y.A. Al-Kofahi, Y.J. Lim, K.L. Smith, J.N. Turner, S.De, B. Roysam, W. Shain and S.J. Kim, "Effects of insertion conditions on tissue strain and vascular damage during neuroprosthetic device insertion" *Journal of Neural Engineering*, 3, 196-207. 2006

[72] V.S. Polikov, P.A. Tresco and W.M. Reichert, "Response of brain tissue to chronically implanted neural electrodes". *Journal of Neuroscience Methods*, 148, 1-18. 2005

[73] A.C. Hoogerwerf and K.D. Wise," A 3-dimensional microelectrode array for chronic neural recording".

IEEE Transaction on Biomedical Engineering, 41, 1136-1146. 1994

[74] Q. Bai, K.D. Wise and D.J. Anderson, "A high-yield microassembly structure for three-dimensional microelectrode arrays". *IEEE Transaction on Biomedical Engineering*, 47, 281-289. 2000

[75] Q. Bai and K.D. Wise, "Single-unit neural recording with active microelectrode arrays". *IEEE Transaction on Biomedical Engineering*, 48, 911-920. 2001

[76] S. Herwik, S. Kisban, A. Aarts, K. Seidl, G. Girardeau, K. Benchenane, M.B. Zugaro, S.I. Wiener, O. Paul, H.P. Neves and P. Ruther, "Fabrication technology for silicon-based microprobe arrays used in acute and sub-chronic neural recording". *Journal of Micromechanics and Microengineering*, 19, No. 074008. 2009

[77] J.G. Du, M.L. Roukes and S.C. Masmanidis, "Dual-side and three-dimensional microelectrode arrays fabricated from ultra-thin silicon substrates". *Journal of Micromechanics and Microengineering*, vol.19, No. 075008, 2009,

[78] J. C. Williams, R. L. Rennaker and D. R. Kipke, "Long-term neural recording characteristics of wire microelectrode arrays implanted in cerebral cortex," *Brain Research Protocols*, vol. 4, pp.303–313, 1999.

[79] P.J. Rousche, D.S. Pellinen, D.P. Pivin, J.C. Williams, R.J. Vetter and D.R. Kipke, "Flexible polyimide-based intracortical electrode arrays with bioactive capability". *IEEE Transaction on Biomedical Engineering*, 48, 361-371. 2001

[80] H. Takahashi, J. Suzurikawa, M. Nakao, F. Mase and K. Kaga, "Easy-to-prepare assembly array of tungsten microelectrodes". *IEEE Transaction on Biomedical Engineering*, 52, 952-956. 2005

[81] S. Takeuchi, T. Suzuki, K. Mabuchi and H. Fujita, "3D flexible multichannel neural probe array."*Journal of Micromechanics and Microengineering,* 14, 104-107. 2004

[82] C. W. Chang and J. C. Chiou, "Development of a Three Dimensional Neural Sensing Device by a Stacking Method," *Sensors*, vol. 10, pp. 4238-4252, May 2010.

[83] A.W. Adamson, "*Physical Chemistry of Surfaces,*"5th ed.; John Wiley: New York, USA, 1990.

[84] C.H. Cheng and H.H. Lin, "Measurement of surface tension of epoxy resins used in dispensing process for manufacturing thin film transistor-liquid crystal displays". *IEEE Transactions on Advanced Packaging*, 31, 100-106. 2008

[85] W. Huang, Y. Yao, Y. Huang and Y.Z. Yu, "Surface modification of epoxy resin by polyether-polydimethylsiloxanes-polyether triblock copolymers". *Polymer* 2001, 42, 1763-1766.

[86] W. Franks, I. Schenker, P. Schmutz and A. Hierlemann, "Impedance characterization and modeling of electrodes for biomedical applications," *IEEE Transactions on Biomedical Engineering*, vol. 52, pp. 1295-1302, 2005.

[87] K. D. Wise, A. M. Sodagar, Y. Yao, M. N. Gulari, G. E. Perlin, and K. Najafi, "Microelectrodes, microelectronics, and implantable microsystems," *Proceedings of IEEE,* vol. 96, pp.1184–1202, 2008.

[88] F.G. Zeng, S. Rebscher,W. Harrison, X. Sun, and H. Feng, "Cochlear implants: System design, integration, and evaluation," *IEEE Reviews in Biomedical Engineering*, vol. 1, pp. 115–142, 2008.

[89] J. D. Weiland and M. S. Humayun, "Visual prosthesis," *Proceedings of IEEE*, vol. 96, no. 7, pp. 1076–1084, Jul. 2008.

[90] A. B. Schwartz, "Cortical neural prostheses,"*Annual Review of Neuroscience,* vol. 27, pp. 487–507, 2004.

[91] D. M. Taylor, I. H. Tillery, and A. B. Schwartz, "Information conveyed through brain-control: Cursor versus robot," *IEEE Transactions on Neural Systems and Rehabilitation Engineering*, vol. 11, no. 2, pp. 195–199, Jun. 2003.

[92] A.M. Sodagar, K.D. Wise and K. Najafi, "A Wireless Implantable Microsystem for Multichannel Neural Recording," *IEEE Transaction on Microwave Theory and Techniques*, VOL. 57, NO. 10, 2009

[93] P. Vaillancourt, A. Djemouai, J. F. Harvey and M. Sawan, "EM radiation behavior upon biological tissues in a radio-frequency power transfer link for a cortical visual implant," *International Conference of the IEEE Engineering in Medicine and Biology Society*, vol. 19, pp. 2499-2502, 1997.

[94] Uei-Ming Jow and Ghovanloo, M., "Modeling and Optimization of Printed Spiral Coils in Air, Saline, and Muscle Tissue Environments," *IEEE Transactions on Biomedical Engineering*, vol.3, no.5, pp.339–347, 2009

[95] N. O. Sokal and A. D. Sokal, "Class-E-A new class of high-efficiency tuned single-ended switching power amplifiers," *IEEE Journal of Solid-State Circuits*, vol. SSC–10, no. 3, pp. 168–176, Jun. 1975

[96] Klaus Finkenzeller "*RFID handbook: Fundamentals and application in contactless smart cards and identification*" Ed. 2, Wiley, John & Sons, 2003

[97] R.R. Harrison, "Designing Efficient Inductive Power Links for Implantable Devices," *IEEE Circuits and Systems Conference*, 2007.

[98] A. Kurs, A. Karalis, R. Moffatt, J.D. Joannopoulos, P. Fisher and M. Soljačić, "Wireless power transfer via strongly coupled magnetic resonances," *Science*, vol. 317, pp. 83-86, Jul 2007.

[99] W.H. Ko, S.P. Liang, and C.D.F. Fung, "Design of radio-frequency powered coils for implant instruments", *Medical & Biological Engineering & Computing*, vol. 15, pp. 634-640, 1977.

[100] N. Mohan, T.M. Undeland and W.P. Robbins, "*Power Electronics: Converters, Applications, and Design*," 3rd edition, John Wiley and Sons, New York, 2003.

[101] Rincon-Mora, G.A.; Allen, P.E., "A Low-Voltage, Low Quiescent Current, Low Drop-Out Regulator," *IEEE Transactions on Solid-State Circuits,*, vol.33, pp. 36-44, 1998

[102] B. Razavi, "*Design of Analog CMOS Integrated Circuit*," McGraw-Hill, 2001

[103] K. Wong and D. Evans, "A 150mA low noise, high PSRR low-dropout linear regulator in 0.13 mu m technology for RF SoC applications," *Proceedings of the IEEE European Solid-State Circuits Conference*, pp. 532-535, 2006.

[104] L. G. Shen, Z. S. Yan, X. Zhang et al., "A Fast-Response Low-Dropout Regulator Based on Power-Efficient Low-Voltage Buffer," *2008 51st IEEE Midwest Symposium on Circuits and Systems Conference Proceedings*, pp. 546-549, 2008.

[105] C. Y. Hsieh, C. Y. Yang, and K. H. Chen, "A Low-Dropout Regulator With Smooth Peak Current Control Topology for Overcurrent Protection," *IEEE Transactions on Power Electronics*, vol. 25, no. 6, pp. 1386-1394, Jun, 2010.

[106] T.M. Seese, H. Harasaki, G.M. Saidel, and C.R. Davies, "Characterization of tissue morphology, angiogenesis, and temperature in the adaptive response of muscle tissue to chronic heating," *Laboratory Investigation*, vol. 78, no. 12, pp. 1553-1562, 1998.

[107] R.R. Harrison, "A Versatile Integrated Circuit for the Acquisition of Biopotentials," *IEEE Custom Integrated Circuits Conference*, pp115-122, 2007.

[108] S. Franco, "*Design With Operational Amplifiers and Analog Integrated Circuits*,"2nd edition, New York: MacGraw-Hill, 1997

[109] C.W. Mundt, K. N.Montgomery, U. E. Udoh, V. N. Barker,G. C. Thonier, A. M. Tellier, R. D. Ricks, R. B. Darling, Y. D. Cagle, N. A. Cabrol, S. J. Ruoss, J. L. Swain, J.W. Hines, and G. T. A. Kovacs, "A multiparameter wearable physiological monitoring system for space and terrestrial applications," *IEEE Transactions on Information Technology in Biomedicine*, vol. 9, no. 3, pp. 382- 391, Sep. 2005.

[110] E. Waterhouse, "New horizons in ambulatory EEG monitoring," *IEEE Engineering in Medicine and Biology Magazine*, vol. 22, no. 3, pp. 74–80, May/Jun. 2003.

[111] R. Martins and F.A. Vaz, "A CMOS IC for portable EEG acquisition systems," *IEEE Transactions on Instrumentation and Measurement*, vol. 47, no. 5, pp. 1191–1196, Oct. 1998.

[112] K. A. Ng and P. K. Chan, "A CMOS analog front-end IC for portable EEG/ECG monitoring applications," *IEEE Transactions on Circuits and Systems I: Regular Papers*, vol. 52, no. 11, Nov. 2005.

[113] R. F. Yazicioglu, P. Merken, and R. Puers, "A 60uW 60 nV/$\sqrt{}$Hz readout front-end for portable biopotential acquisition systems," *IEEE Journal of Solid-State Circuits*, vol. 42, 5: 1100-1110, May 2007

[114] R. R. Harrison and C. Charles, "A low-power low-noise CMOS amplifier for neural recording applications," *IEEE Journal of Solid-State Circuits*, vol. 38, pp. 958-965, Jun 2003.

[115] R.R. Harrison , P.T. Watkins , R.J. Kier , R.O. Lovejoy , D.J. Black , B. Greger and F. Solzbacher, "A low-power integrated circuit for a wireless 100-electrode neural recording system," *IEEE Journal of Solid-State Circuits*, vol. 42, pp. 123-133, Jan 2007.

[116] Aziz, J.N.Y. Abdelhalim, K. Shulyzki, R. Genov, R. Bardakjian, B.L. Derchansky, M. Serletis and D. Carlen, "256-Channel Neural Recording and Delta Compression Microsystem With 3D Electrodes", *IEEE Journal of Solid-State Circuits*, Vol. 44, No. 3, pp. 995-1005. 2009.

[117] M. Mollazadeh, K. Murari, G. Cauwenberghs, and N. Thakor, "Micropower CMOS Integrated Low-Noise Amplification, Filtering, and Digitization of Multimodal Neuropotentials," *IEEE Transactions on Biomedical Circuits and Systems*, Vol. 3, Issue 1, pp. 1-10, 2009.

[118] B. Gosselin, et al., "A Mixed-Signal Multichip Neural Recording Interface With Bandwidth Reduction," *IEEE Transactions on Biomedical Circuits and Systems*, vol. 3, pp. 129-141, Jun 2009.

[119] F. Shahrokhi, K. Abdelhalim and R. Genov, "The 128-Channel Fully Differential Digital Integrated Neural Recording and Stimulation Interface," *IEEE Transactions on Biomedical Circuits and Systems*, vol. 4, pp. 149-161, 2010.

Curriculum Vitae/個人簡歷

武陵高級中學	1996.9-1999.6
國立交通大學電機與控制工程學系	1999.9-2003.7
國立交通大學電機與控制工程研究所碩士班	2003.9-2005.7
國立交通大學電機與控制工程研究所博士班	2005.9-2011.4

Publication List/著作列表

Journal paper/期刊論文

[1] **Chih-Wei Chang** and Jin-Chern Chiou, "Development of a Three Dimensional Neural Sensing Device by a Stacking Method," *Sensors*, Vol.10, no.5, pp.4238-4252, 2010.

[2] **Chih-Wei Chang**, Li-Wei Ko, Fu-Chang Lin, Tung-Ping Su, Tzyy-Ping Jung, Chin-Teng Lin, and Jin-Chern Chiou, "Drowsiness Monitoring with EEG-Based MEMS Biosensing Technologies, " *Journal of Gerontopsychology and Geriatric Psychiatry*, Volume 23 (2), pp.107-113, Jun 1, 2010.

[3] Chia-Lin Chang, **Chih-Wei Chang**, Hong-Yi Huang, Chen-Ming Hsu, Chia-Hsuan Huang, Jin-Chern Chiou and Ching-Hsing Luo, "Power-Efficient Bio-potential Acquisition Device with DS-MDE Sensors for Long-Term Healthcare Monitoring Application," *Sensors*, Vol.10, no.5, pp.4777-4793 , 2010.

[4] Chen-Chun Hung, **Chih-Wei Chang** and Jin-Chern Chiou, "Transparent Microprobe Array Fabricated by MEMS Hot Embossing Technology for Photodynamic Therapy Application," *IEICE Electronic Express*, Vol.7, no. 9, pp569-576, 2010.

[5] Chia-Lin Chang, **Chih-Wei Chang**, Chen-Ming Hsu, Ching-Hsing Luo, Jin-Chern Chiou, "Power-efficient wireless sensor for physiologicalsignal acquisition," *Journal of Micro/Nanolithography, MEMS, and MOEMS*, Vol.8, no.2 , pp. 021120, 2009.

Conference paper/研討會論文

[1] **Chih-Wei Chang**, Kuan-Chou Hou, Li-Jung Shieh, Sheng-Hsin Hung and Jin-Chern Chiou, "Wireless Powering Electronics and Spiral Coils for Implant Microsystem toward Nanomedicine Diagnosis and Therapy in Free-Behavior Animal," *IEEE International Nano-Electronics Conference*, Taoyuan, Taiwan, June 21-24, 2011.

[2] **C.W. Chang**, Y.J. Chen, S.H. Hung and J.C. Chiou, "A Wireless and Batteryless Microsystem with Implantable Grid Electrode/3-Dimenesional Probe Array for ECoG and Extracellular Neural Recording on Rat," *The 16th International Conference on Solid-State Sensors, Actuators and Microsystems* (*Transducers 2011*), June 5-9, 2011, Beijing, China.

[3] J.-R. DUANN, **C.-W. CHANG**, C.-L. CHANG, Y.-J. LIN, S.-C. LIANG, H.-Y. HUANG, C.-H. LUO, J.-C. CHIOU, "Animal EEG/ECoG acquisition system without wire bound," *Neuroscience 2010 Conference*, San Diego, USA, Sessions 818.5, Nov. 13-17, 2010

[4] Jin-Chern Chiou and **Chih-Wei Chang**, "Development of Three Dimensional Neural Sensing Device by Stacking Method," *IEEE Sensors 2010 Conference*, Waikoloa, Big Island, Hawaii, Nov. 1-4, 2010.

[5] **Chih-Wei Chang** and Jin-Chern Chiou, "Stacked Multichip Three-Dimensional Probe array toward Implantable Neural Prostheses," *The 39th Neural Interface Conference,* Long Beach, CA, USA, Jun. 21-23, 2010.

[6] J.C. Chiou, T.J. Ho and **C.W. Chang**, "A 16-channel Instrumentation Amplifier for Versatile Physiological Recording Applications," *The 20th VLSI Design/CAD Symposium*, Hualien, Taiwan, 2009

[7] 邱俊誠、洪振鈞、謝禮忠、蔡櫂隆、侯冠州、**張志瑋**, "利用 CMOS MEMS 及後製程製作之靜電式低電壓驅動光相位調制器陣列", *The 13th Nano and Microsystem Technology Conference*, Hsinchu, Taiwan, Jul. 9-10, 2009

[8] J.C. Chiou, **C.W. Chang** and T.J. Ho, "Chopper-Stabilized Differential-Difference Instrumentation Amplifier for Body Surface Physiological Signal Recording," *Electronic Technology Symposium*, Kaohsiung, Taiwan, June 19, 2009

[9]   **C.W. Chang** and J.C. Chiou, "Surface-Mounted Dry Electrode and Analog-Front-End Systems for Physiological Signal Measurements," *IEEE/NIH 2009 LIfe Science Systems and Applications Workshop*, pp.108-111, Bethesda, Maryland, USA, April 9-10, 2009

[10] J.C. Chiou , **C.W. Chang** and C.C. Chou, "A CMOS Chopper-Stabilized Instrumentation Amplifier for MEMS Physiological Sensor Applications," *The 19th VLSI Design/CAD Symposium*, Kenting, Taiwan, pp.560-563, Aug., 2008

[11] J.C. Chiou , **C.W. Chang**, Y.J. Lin, C.T. Lin, L.W. Ko and I.L. Tsai, "The Development of Portable BCI System with MEMS EEG sensors for Drivers' Drowsiness Estimation," *Asia-Pacific Conference on Transducers and Micro-Nano Technology*, Tainan, Taiwan, June 22-25, 2008.

[12] Chang, C.M. Hsu, S-C Lai, **C.W. Chang** ,C.H. Luo and J.C. Chiou, "A Power-Efficient Wireless Biotelemetry For MEMS Sensing Physiological Signal Analysis," *Asia-Pacific Conference on Transducers and Micro-Nano Technology*, Tainan, Taiwan, June 22-25, 2008.

[13] J.C. Chiou , **C.W. Chang**, Y.J. Lin, C.T. Lin, L.W. Ko and J.F. Chung, "Portable EEG-Based Biomedical System with Drowsiness Detection in Smart Room Control," *18th ASME Annual Conference on Information Storage & Processing Systems*, Santa Clara, California, USA, June 16-17, 2008.

[14] J.C. Chiou, C.F. Kuo, Y.J. Lin, **C.W. Chang**, and K.C. Hou, "Development of Novel Cascade Structure for Improving Stroke of Electrostatic Comb-Drive Actuator," *21st IEEE International Conference on Micro Electro Mechanical Systems*, Tucson, Arizona, USA, Jan. 13-17, 2008.

[15] 邱俊誠、林永峻、**張志瑋**、蔡尚瑋、謝禮忠、吳順德，"生醫應用微型感測器與模組之研究與發展," *電子月刊*, 2008 年 1 月號 150 期, pp. 121-135.

[16] Chin-Teng Lin, Jin-Chern Chiou, Li-Wei Ko, Y. J. Lin, **C. W. Chang**, Sheng-Fu Liang, Ching-Hsing Luo, Tung-Ping Su, "Development of Mobile Wireless Brain Computer Interface for Drowsiness Detection, " *Proceedings of 2007 CACS International Automatic Control Conference*, Taichung, Taiwan, Nov. 9-11, 2007.

[17] J. C. Chiou, **C. W. Chang**, C. L. Chen, "MEMS based Dry Electrodes for Biopotential Measurement", *Symposium on Genetic System for Neuroscience Research*, NYMU, Taiwan, Jan., 2005.

[18] **C. W. Chang**, J. C. Chiou, Y.C. Lin, "A Multiple Electrostatic Electrodes Torsion Micromirror Device with Linear Stepping Angle Effect," *OPT2004*, NCU, Taiwan, Dec., 2004.

Patent/專利

[1]   Jin-Chern Chiou, Chen-Chun Hung and **Chih-Wei Chang**, "*METHOD FOR FABRICATING MICRONEEDLE ARRAY AND METHOD FOR FABRICATING EMBOSSING MOLD OF MICRONEEDLE ARRAY*," US Patent 7429333B2.

[2]   Jin-Chern Chiou and **Chih-Wei Chang**, "*INTEGRATION STRUCTURE OF SEMICONDUCTOR CIRCUIT AND MICROPROBE SENSING ELEMENTS AND METHOD FOR FABRICATING THE SAME*," US Patent 7875479B2.

[3]   邱俊誠、**張志瑋**、洪振鈞，「*微探針陣列結構*」，中華民國專利發明第 I328441 號

Project/研究計畫

[1]   UCSD/DARPA Project "Development of Dry MEMS Bio-Sensors," 2005/06/01 ~ 2006/05/31

[2]   國科會「應用於日常生活環境之可攜式人性化腦波監控與腦機介面系統」2005/11/01 ~ 2008/10/31

[3]   國科會「心理人文與智慧工程共構之可塑型優質高齡化生活空間科技」2006/08/01 ~ 2009/09/30

[4]   榮臺聯大計畫「智慧型可攜式多重睡眠生理紀錄與分析系統及其在睡眠呼吸中止症診斷與駕車瞌睡防止之應用－可拋棄式高精度微機電生醫訊號感測器之研發」2007/01/01 ~ 2009/12/31

[5]   國科會晶片系統國家型科技計畫(NSoC)「智慧型仿生系統之晶片系統平台技術開發－三維電極感測陣列之研發」2008/08/01 ~ 2011/07/31

[6]   國科會晶片系統國家型科技計畫(NSoC)「動物實驗用癲癇治療電子系統之實現」2010/11/01~2011/07/31

[7]   國科會晶片系統國家型科技計畫(NSoC)「具生物反饋機制之智慧型長時睡眠監測系統－應用於智慧型長時睡眠監測系統之感測器與類比前端積體電路設計」2009/08/01~2011/07/3

[8] 國科會晶片系統國家型科技計畫(NSoC)「癲癇治療電子系統之研發及其動物實驗之驗證－整合式三維生物神經訊號感測介面」2011/5/1 ~ 2014/7/31

Teaching Assistant/課程助教

[1] 交大電控所, 邏輯設計與實驗(96 學年上學期)
[2] 交大電控所, 訊號與系統(96 上學期、下學期)
[3] 交大電控所, 微機電系統技術導論(97、98、99 學年上學期)

Award/獎項

[1] 生醫積體電路設計創意競賽第一名「Bioelectronics for Better Life」生醫電子積體電路設計研習營, 2010
[2] 國家新創獎學生組第一名 「具準確設置特性之乾式電極陣列與可自動偵測波峰區間之十二導程心電圖儀研發」國家新創獎, 2007
[3] "The Design and Fabrication of Silicon Micro Probe Array," Best Poster Award, Symposium on Genetic Systems for Neuroscience Research, University of Taiwan, 2005

Other Experience/其他

[1] 台灣-史丹佛醫療產品設計種子人才培訓 2009.8 ~ 2010.1